Theoretical Investigations of Cluster Compounds on the 1 nm Scale: Geometric, Electronic, and Optical Properties

Takeshi Iwasa

DOCTOR OF
PHILOSOPHY

Department of Structural Molecular Science
School of Physical Sciences
The Graduate University for Advanced Studies

2008

To my parents

Contents

Abstract

The aim of this thesis is to theoretically study geometric, electronic, and optical properties of one-nanometer sized cluster compounds. The thesis is composed of two parts. In the first part, the geometric and electronic properties of gold-thiolate cluster compounds, which have recently been studied experimentally, are revealed. I will discuss how the local geometric structures are related to the electronic properties of the compounds. In the second part, optical response theory that is applicable to the nanocluster compounds is developed. Special emphasis is placed on nonuniform electronic excitations induced by near-fields.

Let me briefly review history of metal nanoclusters. Research in nanocluster compounds has its root on the study of bare metal clusters in gaseous phase, where size-dependent physicochemical properties are the main concern. However, most of these bare clusters are energetically and chemically unstable. In the past few decades, metal clusters protected by organic molecules have been synthesized in solution, and some of these cluster compounds were found to be stable even in the air. Although these nanocluster compounds were expected to be promising candidates for functional nanomaterials in a wide range of nanotechnologies, it is not trivial to characterize their detailed structures. Reducing the size of clusters to the 1 nm scale, their geometries and other properties become much more sensitive to the change in size and chemical compositions. In such circumstances, sub-nanometer sized gold-cluster compounds have intensively been synthesized with the definitive determination on the chemical compositions. Despite the brilliant results, even their geometrical structures have not sufficiently been characterized. Furthermore, the studies on their optical properties are still in the juvenile stage. For these reasons, I theoretically study the geometric, electronic, and optical properties of some representative cluster compounds at the 1 nm scale.

The geometric and electronic structures of a gold-methanethiolate $[Au_{25}(SCH_3)_{18}]^+$ are investigated by carrying out the density functional theory (DFT) calculations. The obtained optimized structure consists of a planar Au_7 core cluster and Au-S complexes, where the Au_7 plane is enclosed by a $Au_{12}(SCH_3)_{12}$ ring and sandwiched by two $Au_3(SCH_3)_3$ ring clusters. This geometry differs in shape and bonding from a generally accepted geometrical motif of gold-thiolate clusters that a spherical gold cluster is

superficially ligated by thiolate molecules. This newly optimized gold-methanthiolate cluster shows a large HOMO-LUMO gap, and calculated X-ray diffraction and absorption spectra successfully reproduce the experimental results. On another gold cluster compound $[Au_{25}(PH_3)_{10}(SCH_3)_5Cl_2]^{2+}$, which consists of two icosahedral Au_{13} clusters bridged by methanethiolates sharing a vertex gold atom and terminated by chlorine atoms, the DFT calculation provides very close structure to the experimentally obtained gold cluster $[Au_{25}(PPh_3)_{10}(SC_2H_5)_5Cl_2]^{2+}$. I further demonstrate that a vertex-sharing triicosahedral gold cluster $[Au_{37}(PH_3)_{10}(SCH_3)_{10}Cl_2]^{+}$ is also achieved by bridging the core Au_{13} units with the methanethiolates. A comparison between the absorption spectra of the bi- and triicosahedral clusters shows that the new electronic levels due to each oligomeric structure appear sequentially, whereas other electronic properties remain almost unchanged compared to the individual icosahedral Au_{13} cluster. These theoretical studies have elucidated the fundamental properties of the promising building blocks such as geometric structures and stability of real cluster compounds in terms of the detailed electronic structures. As a next step, I have to gain a further insight into the dynamical optical properties of cluster compounds. In particular for discussing photoinduced dynamics in nanoclusters or nanocluster assemblies, inter-cluster near-field interactions should be understood properly. The conventional light-matter interaction based on available lasers is quite different from the near-field interaction. The electric fields of available lasers usually have the wavelength much longer than the size of the local structure of the cluster compounds. In other words, the 1-nm-sized cluster compounds feel the almost uniform electromagnetic field and thus the local structures of the compounds cannot be resolved. In contrast, a near-field interaction occurs at the same scale of the cluster compounds and is thus expected to be used to observe the local structure of the 1 nm sized materials. The difficulty in their theoretical description arises from the fact that the near-field has a non-uniform local structure. For these reasons, I will develop an optical response theory that is applicable to 1-nm-sized clusters interacting with the near-field.

The optical response theory is developed in a general form on the basis of the multipolar Hamiltonian derived from the minimal coupling Hamiltonian by a canonical transformation. The light-matter interaction in the multipolar Hamiltonian is described in terms of the space integral of inner product of polarization and electric field, whereas the minimal coupling Hamiltonian uses momentum and vector potential, which are rather inconvenient for practical computations. Noteworthy is the fact that the polarization in the integral can be treated entirely without any approximations. This means an infinite order of multipole moments is taken into account. Thus the present approach is a generalization of the optical response formulation beyond the dipole approximation. I have incorporated the optical response theory with the nonuniform light-matter interaction into an electron-dynamics simulation approach based on the time-dependent density functional theory (TDDFT) in real space. To elucidate the electron dynamics of 1 nm-sized molecules induced by the nonuniform light-matter interaction, the integrated TDDFT approach has been applied to and

computationally solved for a test molecular system, NC_6N, in the dipole radiation field. Several unprecedented electronic excitation modes were induced owing to the nonuniform light-matter interaction using the near-field in contrast to the uniform light-matter interaction that corresponds to the conventional dipole approximation. For example, high harmonics were generated more easily. It has also been found that the near-field with different phase and spatial structure promotes or suppresses high harmonics.

In conclusion, I have revealed the geometric and electronic properties of gold-thiolate nanocluster compounds and developed optical response theory in an effort to understand nonuniform light-matter interaction between near-filed and 1nm-sized cluster compounds.

Acknowledgements

I would like to acknowledge and extend my heartfelt gratitude to the following people who have made the completion of this dissertation possible:

First of all, I am extremely thankful to Prof. Katsuyuki Nobusada. His valuable and consistent encouragement and support have propelled me to start and eventually complete this dissertation.

My sincerest gratitude also goes to Prof. Tatsuya Tsukuda and Prof. Yuichi Negishi, who have furnished me with their important data and participated in fruitful discussions.

Also, I would like to thank Prof. Tomokazu Yasuike for the assistance he extended and the inspiration he provided. Dr. Masashi Noda has made considerable improvements in our TDDFT program, which helped me so much. My thank-you list also includes all laboratory members who have helped me throughout this dissertation. Among them, Dr. Kazuya Shiratori, who garnered his Ph.D. last year, supported me with daily discussions for this study.

To the members of other groups; Prof. Yasufumi Yamashita, Dr. Nobuya Maeshima, Dr. Satoshi Miyashita, Dr. Yasuhiro Tanaka, Mr. Wataru Mizukami: thank you for helping me out with quantum and/or computational physics.

This list is, of course, topped by the most important people in my life—my family and friends.

Chapter 1

Introduction

1.1 Thesis overview

This thesis is composed of two parts. In the first part (chapter 2), theoretical studies of the static physicochemical properties of gold cluster compounds, such as geometric and electronic structures and photoabsorption spectra are presented. The choice of the gold cluster compounds was due to a series of recent seminal experiments that succeeded for the first time in synthesizing and isolating gold thiolate clusters at the 1 nm scale with high precision [1–6]. The detailed static properties of some gold cluster compounds are fully discussed by resorting to the density functional calculations.

In the second part, I theoretically study dynamical optical properties of nanoclusters at the 1 nm scale. Nanoclusters have received much attention due to the potential applications to molecular-sized quantum devices associated with their unusual physicochemical properties of electronic structures, optical response, magnetism, catalysis and so forth [7–11]. Among those fascinating properties, this thesis is mostly motivated by recent appealing experiments that had demonstrated surface plasmon propagation through an array of nanoparticles [12–22]. The surface plasmon is strongly related to near-fields, which are observed only around nanostructures [23–44]. Optical near-field interactions between nanostructures have been studied in various ways [45–61]. Nevertheless, a theory of interaction between the near-field and the 1-nm-sized materials, particularly in the time domain, has not yet been well established. It is, thus, highly desired to develop such an optical response theory. In chapters 3-5, the optical response theory for 1-nm-sized nanoclusters is developed with special emphasis on understanding a nonuniform light-matter interaction induced by a near-field.

1.2 Nanocluster science

This section explains the interesting and important properties of gold cluster compounds, starting with a brief historical overview.

1.2.1 Bare metal clusters

Research in nanocluster compounds has its root on the studies of bare metal clusters in gaseous phase, where size-dependent physicochemical properties are the main concern [62,63]. While most of bare metal clusters are energetically and chemically unstable, some clusters with specific size have been found to be unusually stable. These specific clusters are called magic clusters. Some representative magic gold clusters of Au_{13}, Au_{55}, $\cdots$ have been intensively studied [64–69]. Despite their unusual size-distribution, it is difficult to prepare size-selective or monodispersed magic clusters. The magic clusters, even if they are prepared size-selectively, are in general unstable in the air with room temperature. Furthermore, the bare metal clusters usually have simple structures close to a spherical symmetry. For these reasons, the bare metal clusters have so far been mainly investigated in the context of basic cluster science and have not been discussed with the aim of developing cluster-assembled materials. Such conventional cluster science turned around after the method to prepare and isolate metal clusters size-selectively by protecting organic molecules had been established. In the next section, I will explain the importance of metal-molecule, in particular gold-thiolate, cluster compounds.

1.2.2 Gold cluster compounds

Small gold clusters protected by thiolate molecules have received much attention due to their unique physicochemical properties such as optical response, catalysis, and magnetism [70–74]. The thiolated gold clusters are also of increasing importance in the rapidly growing area of nanotechnology because they are expected to be one of the prototypes of molecular-sized materials which might function as optical devices, electrical junctions, and chemical sensors [75–81].

For example, some groups observed giant magnetic moments in thiolated gold surfaces [82] or thin films [83, 84]. The key ingredient to understand the giant magnetic moments is localized electrons transferred from the gold substrate to the thiolate molecule. Vager and Naaman proposed a theoretical model that the transferred electrons form electron pairs in the triplet state (i.e., boson electron pairs) and these boson pairs induce the giant magnetic moments [85]. On the other hand, Hernando *et al.* explained the unexpected magnetism as due to the blocking of a local magnetic moment by the giant magnetic anisotropy [83, 84]. They suggested that the transferred localized electrons induce such giant anisotropy through spin-orbit interaction.

Such unexpected magnetism was observed similarly in thiolated gold nanoparticles [72, 86–88]. Crespo *et al.* reported that the thiol capped gold nanoparticles, whose averaged core size is ca. 1.4 nm, showed ferromagnetic hysteresis with magnetic moment per Au atom $\mu = 0.036\ \mu_B$ [72]. However, the value of the magnetic moment is several orders of magnitude smaller than those of the thiol capped gold thin films [83,84]. Furthermore, they found that the gold nanoparticles stabilized by weak-interacted ligands of tetraoctyl ammonium bromide became diamagnetic. In contrast,

Yamamoto *et al*. reported that the X-ray magnetic circular dichroism (XMCD) study revealed the intrinsic magnetism consisting of a superparamagnetic part obeying the Curie law and of a temperature-independent Pauli-paramagnetic part in gold nanoparticles embedded in weak interacted ligands, poly(N-vinyl-2-pyrrolidone) [88,89]. They attributed such magnetism to the mixture of ferromagnetism of the surface gold atoms and the Pauli-paramagnetism of the core atoms. As completely opposite to the result obtained by Crespo *et al*., they observed that the strong interacting ligand such as thiolates quenched the surface ferromagnetism. The magnetism observed in various types of gold-thiolate systems, particularly in nanoparticles, is still controversial. These controversial issues concerning the magnetic properties in gold-thiolate systems are partly raised owing to the fact that the detailed electronic structures of these gold-thiolate systems were not fully specified. In other words, spin-polarized electronic structures of these systems have not been clarified.

Since these properties depend on their cluster sizes and structures, progress in the synthesis of gold-thiolates with well-defined chemical compositions is crucial in not only fundamental but also applied sciences. A number of methods to prepare and isolate monodispersed gold-thiolates have so far been developed [71,90–95] and in a recent paper Negishi et al. achieved the size-separated synthesis of glutathione (GSH)-protected gold clusters, Au-SG [1]. In the paper, they decided the definitive chemical composition of a series of the clusters, $Au_{10}(SG)_{10}$, $Au_{15}(SG)_{15}$, $Au_{18}(SG)_{14}$, $Au_{22}(SG)_{16}$, $Au_{22}(SG)_{17}$, $Au_{25}(SG)_{18}$, $Au_{29}(SG)_{20}$, $Au_{33}(SG)_{22}$, and $Au_{39}(SG)_{24}$, with high-resolution mass spectrometry, although their geometrical structures remain unresolved. Therefore, it is highly desirable to specify the geometric structures of these cluster compounds. In 2.1, the theoretical investigation on the geometry of one of these Au-SG clusters will be discussed.

1.2.3 Ordered nanoparticle assembly

As mentioned above, nanometer-sized metal clusters have been under extensive investigation owing to their novel physicochemical properties, which are known to be significantly different from those of the corresponding bulk metals. Metal nanoclusters are also expected to be key ingredients in new materials that function as molecular-sized quantum devices [75, 81, 96]. There is a rapidly growing understanding of fundamental properties of each individual metal nanocluster. However, relatively little is known about whether these clusters retain their individual properties after assembly as well as produce new collective features due to aggregation. The most direct approach to this issue is thought to specify a unit cluster that serves as a building block of cluster-assembled compounds, and then determine how the assembled compounds are constructed from the units. Nevertheless, it is not trivial to construct such cluster-assembled compounds in a bottom-up approach because each metal cluster easily coalesces into an aggregate through altering their individual geometrical and electronic structures. In general, the original physicochemical properties become rather obscure after aggregate formation and then the properties of bulk metals are

dominant.

To realize the cluster-assembled compounds with electronic properties of each metal constituent, the "*clusters of clusters*" concept proposed by Teo and coworkers [97–99] is suggestive. In a series of extensive investigations, they demonstrated that oligomeric metal-cluster compounds were systematically synthesized in a stepwise manner by aggregating icosahedral metal clusters. In such *clusters of clusters*, the individual icosahedral clusters serve as the basic building blocks and then form a polyicosahedral cluster through sharing vertex atoms. Khanna and Castleman and their coworkers have intensively demonstrated that aluminum-based icosahedral clusters (referred to as "*superatoms*" in their studies) form cluster-assembled compounds [100, 101]. The key in both concepts of *clusters of clusters* and *superatoms* is that the assembled compounds are constructed from building units retaining the electronic properties of the constituent units. Similarly to the polymerized clusters based on *cluster of cluster*, very recently a gold cluster-assembled compound was synthesized [6]. This cluster compound is regarded as a Au_{13} dimeric one in which two Au_{13} clusters share one vertex gold atoms. For larger assemblies, it is crucial to understand how the constituent unit clusters are assembled. In 2.2, I will explain the mechanism of oligomerization of the gold cluster compounds.

1.3 Optical response of nanoclusters

1.3.1 Toward dynamical properties

The first step to achieve cluster-based devices at the nanometer scale is to understand the static physicochemical properties of the constituent building blocks, in both isolated and assembled states. Once obtained these properties, the next step is to study their dynamical properties associated with electric current, energy transfer, and chemical reactivity. In particular, for discussing photoinduced dynamics in nanoclusters or nanocluster assemblies, we should have proper understanding of an inter-cluster near-field interaction. Several recent appealing experiments concerning near-field excitation dynamics in nanoparticle systems will be reviewed.

I would like to mention about recent appealing experiments, which motivate the second part of this thesis, of a propagation of surface plasmon or electromagnetic energy in weakly-interacting ordered metal nanoparticle systems at the hundred nanometers [12–22]. These experiments are schematically explained in Fig.1.1. The orange and blue spheres represent nanoparticles and near-field interactions, respectively, and the black illustrates the tip of a scanning near-field optical microscopy (SNOM) [23–44, 102–110]. The leftmost particle is locally irradiated by the tip and then the electromagnetic energy transfers from the tip to the particle through the near-field interaction. The electromagnetic energy is subsequently propagated along the array also through the near-field interaction. Experiments of local excitation of single gold nanostructure using SNOM also inspired this thesis [34,37,38,40,103,111–113]. In these experiments, surface plasmon has been induced by the near-field illumination

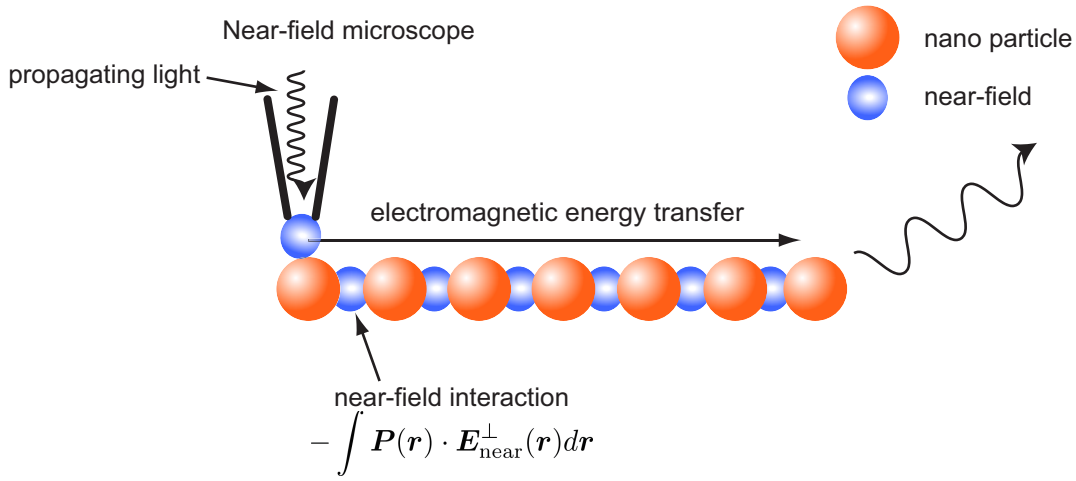

Figure 1.1: The image of photonic currents, where the orange sphere, the blue circle, and the black object, respectively represent metallic nanoparticles, near-field interactions, and a SNOM tip. An array of nanoparticles has been excited by a near-field around the probe tip (left) and then an electromagnetic field is propagated through the array from the left to the right.

which excites a local part of the wavefunction of the gold nanostructure. The near-field illumination of the single gold nanostructure can be considered as a local excitation of a coherent wavefunction. In contrast, the surface plasmon propagation through the nanoparticle array can be considered as a local excitation of an incoherent system. The near-field interaction between each nanoparticle introduces a coherency into the arrayed system.

Optical properties of metal nanoparticles, especially noble metal nanoparticles, have been extensively studied both experimentally and theoretically because of their ability to largely increase the measured signal of the Raman spectroscopy, which is known as Surface Enhanced Raman Spectroscopy (SERS) [114–120]. One of the origin of SERS is considered to be a largely enhanced electromagnetic field caused by a surface plasmon of a metal nanoparticle. Between closely spaced nanostructures, largely enhanced electromagnetic fields have also been reported and used as a nonlinear-optical source or chemical reaction field aiming at a new type of chemical reactions [102, 121–124].

1.3.2 Optical response in 1-nm-sized nanoclusters

The above-mentioned experiments clarify the two essences of the near-field; the large enhancement of an electromagnetic field intensity and the localized character. For the first one, the intensity of near-fields is enhanced by a surface plasmon induced by an incident light. The incoming propagating light oscillates electrons in a nanostructure and this oscillation (the surface plasmon) generates a new electromagnetic field around the surface of the nanostructure. The electrons then interact with the newly generated

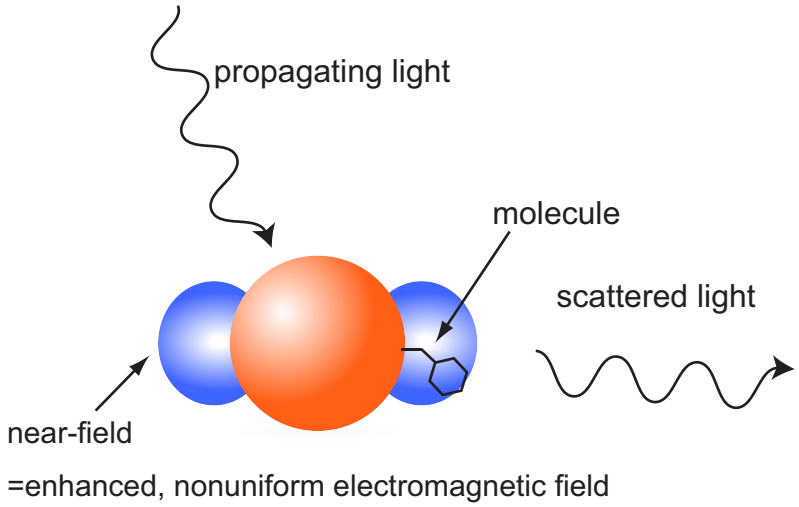

Figure 1.2: SERS is schematically illustrated. The orange particle and the blue circles represent a metallic nanoparticle and a near-field interaction, respectively. A molecule on the surface of the nanoparticle is exposed to the near-field and scatters the light.

field and regenerate an electromagnetic field. This feedback loop continues endlessly. Thus, theoretically, the field enhancement requires a self consistent solution for light-matter interactions. The field enhancement for metal particles at the 100 nm scale has been studied theoretically by solving the Maxwell's equations using the Green's function method [23–25], the Finite Difference Time-Domain (FDTD) method [125–132], the Multiple MultiPole method [32, 133], and/or Discrete Dipole Approximation (DDA) [51]. The method of Green's function is also used to analyze the surface plasmon in gold nanostructures induced by the near-field illumination [34, 37, 38, 40, 103, 111–113]. These field enhancement are, however, not necessarily important at the 1 nm scale, because the surface plasmon owes much to the particle size and does not occur at the 1 nm scale. Therefore, we can concentrate on the nonuniform light-matter interaction to study near-field interaction of nanoclusters at the 1 nm scale. For the second property, the localized character can be understood as that a near-field has a nanoscale spatial structure. As a result, a material in the near-field will interact with a nonuniform electromagnetic field.

The quantum mechanical treatment is required for the nanoclusters at the 1 nm scale. Whereas a near-field is still able to be treated as a classical electromagnetic field as long as the field intensity is rather strong. The strong means that one or two photon absorption or emission due to a light-matter interaction does not largely decrease or increase the intensity of the field. An optical response theory based on this assumption is called the semiclassical theory, that is, the quantum mechanics is used for matter and the classical electrodynamics for light. Under this semiclassical approach, the most rigorous treatment is to solve the coupled Schrödinger and the Maxwell's equations self consistently [45, 47, 54, 55, 134]. Although this theory can

be used for considering non-uniformity and field enhancement simultaneously, actual computations are computationally demanding. On the other hand, near-field interactions between two quantum mechanical particles have been studied [56–61], where interparticle interaction is reduced to be dipole-dipole or dipole-multipole interactions using simple metallic particles. However, the effect of the nonuniform electromagnetic field on electronic excitations was not clearly understood by these studies. Thus, I establish a suitable theory to reveal the nonuniform electronic excitation.

The theory developed in this thesis is based on a semiclassical treatment that 1-nm-sized materials are treated quantum mechanically while the electromagnetic fields are treated classically. Main focus of this study is the nonuniform electronic excitation of molecules at the 1 nm scale. Thus, the special emphasis is placed on an explicitly taking account of the spatial distribution of the electromagnetic field.

Chapter 2

Gold cluster compounds

- "Theoretical Investigation of Optimized Structures of Thiolated Gold Cluster $[Au_{25}(SCH_3)_{18}]^+$", T. Iwasa, and K. Nobusada, *J. Phys. Chem. C*, **111**, 45-49, (2007)

- "Thiolate-Induced Structural Reconstruction of Gold Clusters Probed by ^{197}Au Mossbauer Spectroscopy", K. Ikeda, Y. Kobayashi, Y. Negishi, M. Seto, T. Iwasa, K. Nobusada, T.Tsukuda, and N. Kojima *J. Am. Chem. Soc.*(communications), **129**, 7230, (2007)

- "Gold-thiolate core-in-cage cluster $Au_{25}(SCH_3)_{18}$ shows localized spins in charged states", T. Iwasa and K. Nobusada, *Chem. Phys. Lett.* **441**, 268-272, (2007)

- "Oligomeric Gold Clusters with Vertex-Sharing Bi- and Triicosahedral Structures", K. Nobusada, and T. Iwasa, *J. Phys. Chem. C* (Communication), **129**, 7230, (2007)

Geometric, electronic and optical properties of the unusually stable gold-thiolate cluster $Au_{25}(SCH_3)_{18}$ and the bi- and triicosahedral clusters are theoretically studied in this chapter. Ch. 2.1.2 decides the geometrical structure of $Au_{25}(SCH_3)_{18}$ in its cationic state (1+) with a closed electronic shell structure. In 2.1.3 and 2.1.3, I will investigate the spin polarization and absorption spectra of the gold-thiolate cluster $[Au_{25}(SCH_3)_{18}]^n$ with different charged states $n = 3-, 2-, 1-, 0, 1+$, and 3+. Ch. 2.2.2 describes the geometrical and electronic structures of bi- and triicosahedral clusters and the relationship between the geometries and absorption spectra will be discussed in 2.2.3. To this end, I have performed DFT calculations of the cluster explicitly taking account of the spin multiplicity.

2.1 Gold-thiolate cluster: $Au_{25}(SCH_3)_{18}$

Very recently, Negishi and Tsukuda experimentally confirmed that $Au_{25}(SG)_{18}$ was unusually thermodynamically [1] and chemically stable in comparison with the other Au-SG clusters [2]. The report of large-scale synthesis of $Au_{25}(SG)_{18}$ supports its extraordinarily high stability [3]. They also found that the pattern of the absorption spectrum of $Au_{25}(SG)_{18}$ was rather insensitive to change of the ligand (SG) for other thiolate molecules, in sharp contrast to the other Au-SG clusters that showed ligand-sensitive absorption spectra. These experimental observations imply the existence of a characteristic $Au_{25}S_{18}$ framework. Concerning the framework, on the basis of the X-ray diffraction (XRD) spectrum of $Au_{25}(SG)_{18}$, they have proposed that this cluster has a Au_{25} core cluster with a face-centered-cubic based structure. Unfortunately, the detailed geometrical structure was still unclear. Thus, to study the physicochemical properties of the $Au_{25}(SG)_{18}$ cluster, I begin with deciding the geometrical structure.

The XMCD study of a series of the Au-SG clusters was also reported by Negishi and Tsukuda [4]. This is the first study that the magnetic properties were investigated for the fully size-specified gold-thiolate clusters. Although they found that the Au-SG clusters were spin-polarized, the clusters were only paramagnetic with $\mu = 0.0093\mu_B$ per Au-S bond. On the other hand, in metal cluster compounds, it has been known that their stabilities are strongly affected by the number of electrons. A charging thus would have a nontrivial impact on its electronic properties such as absorption spectrum. However, on $Au_{25}(SG)_{18}$, change in the charge states unaffects its absorption spectrum [5]. In 2.1.3, I will discuss the charging effects on the absorption spectrum of the gold-thiolate cluster.

2.1.1 Computational details

I have carried out DFT calculations for the gold-methanethiolate cluster $[Au_{25}(SCH_3)_{18}]^+$, which is a theoretical model for the glutathione-protected gold cluster $Au_{25}(SG)_{18}$. I have adopted such a simplification of ligands frequently used in the previous calculations [135–140] because the full geometry optimization of $Au_{25}(SG)_{18}$ requires incredibly large computational costs. Furthermore, the above-mentioned experimental result, i.e. the absorption spectrum of $Au_{25}(SL)_{18}$ having a lack of dependence on the ligand L, partly supports this modeling. The present model cluster was calculated in its cationic state with a closed shell structure to avoid considering explicit spin effects. Charging effects on the geometric structure are mentioned in Section 3.

The geometry optimization was starting from two types of initial structures with different Au_{25} core structures. One of the Au_{25} cores is based on a face-centered-cubic (fcc) structure with six Au(111) facets consisting of eight gold atoms as shown in Figure 2.1(a). The other one is based on a vertex-sharing centered icosahedral Au_{13} dimer as shown in Figure 2.1(b). In this thesis, I refer to these clusters as FCC-Au_{25} and SES-Au_{25}, respectively. FCC-Au_{25} is chosen following the experimental result of the XRD spectrum, and SES-Au_{25} is taken into account by analogy with

a trimetalic cluster coordinated by triphenylphosphine (Ph_3P-) and chlorine (Cl) ligands, $[(Ph_3P)_{10}Au_{12}Ag_{12}PtCl_7]Cl$ [141]. The initial structures of $[Au_{25}(SCH_3)_{18}]^+$ are constructed by passivating each core cluster with 18 methanethiolate molecules within D_{3d} molecular symmetry for FCC-Au_{25} and within C_{2v} molecular symmetry for SES-Au_{25}.

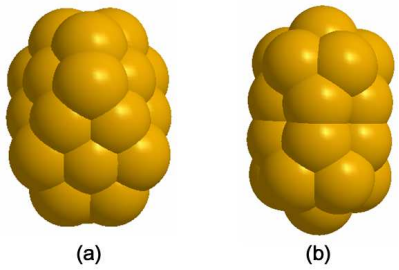

Figure 2.1: Optimized structures of bare Au_{25} clusters (a)FCC-Au_{25} and (b) SES-Au_{25}.

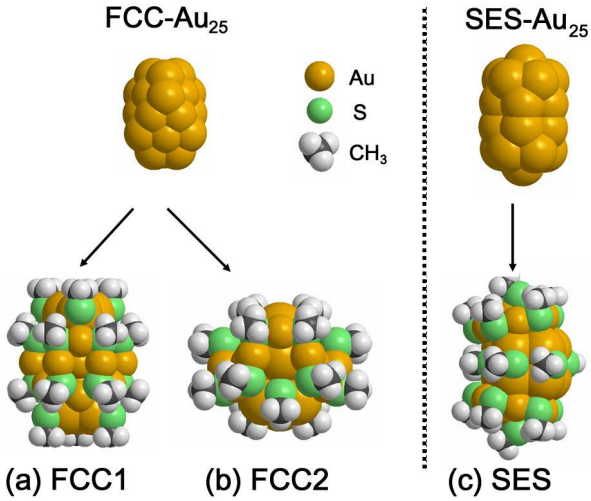

Figure 2.2: Optimized geometry of the gold-methanethiolates (a) FCC1, (b) FCC2, and (c) SES, respectively.

In this chapter, all the quantum chemical calculations were carried out employing the TURBOMOLE package of ab initio quantum chemistry programs [142]. The geometry optimizations based on a quasi-Newton-Raphson method were performed at the level of Kohn-Sham density functional theory (KS-DFT) employing the Becke three-parameter hybrid exchange functional with the Lee-Yang-Parr correlation functional (B3LYP) [143,144]. The triple-ζ valence-quality plus polarization (TZVP) basis

from the TURBOMOLE basis set library has been used in all calculations, along with a default 60-electron relativistic effective core potential (ECP) [145] for the Au atom. The absorption spectra were simulated by calculating the oscillator strength within time-dependent density functional theory (TDDFT). The present TDDFT is based on time-dependent Kohn-Sham response theory [146–149] Excited state properties were obtained from a pole analysis of frequency-dependent linear response functions.

The XRD spectra of the optimized structures were calculated by using the Debye formula [150]. The diffracted intensity $I(s)$ as a function of the diffraction vector length $s = \frac{2\sin\theta}{\lambda}$ is given by

$$I(s) = \sum_{i,j=1}^{N} \frac{\cos\theta}{(1+\alpha\cos^2 2\theta)} \exp\left(-\frac{Bs^2}{2}\right) f_i f_j \frac{\sin(2\pi s r_{ij})}{2\pi s r_{ij}},$$

where r_{ij} is the distance between the i-th and j-th atoms in the optimized gold-methanethiolates and (f_i, f_j) are the corresponding atomic scattering factors. θ is the diffraction angle, and λ is the wavelength of the incident X-ray beam. Angular dependent geometrical and polarization factors are expressed in the form of $\frac{\cos\theta}{(1+\alpha\cos^2 2\theta)}$, where α is almost equal to unity for the unpolarized incident beam. The damping factor $\exp\left(-\frac{Bs^2}{2}\right)$ means thermal effects. Since the charging effect of each atom was not taken into account, the scattering factor of an i-th atom is equal to its atomic number. The equipment dependent parameters were set to be $\alpha = 1.01$ and $\lambda = 0.1051967$ nm following the experiments by Negishi and Tsukuda [151]. On the other hand, the dumping parameter $B = 0.005$ nm^2 was chosen to reproduce the XRD spectrum of $Au_{25}(SG)_{18}$ according to what was discussed in ref [152].

2.1.2 Geometrical structures

I have obtained three types of optimized structures for $[Au_{25}(SCH_3)_{18}]^+$. Two of these structures are derived from FCC-Au_{25}, and the other one from SES-Au_{25}. The three optimized structures are shown in Figure 2 and their structural parameters are summarized in Table 1. The atoms of Au, S, C and H are shown in gold, green, gray, and white, respectively. In the following discussion, the two optimized structures derived from FCC-Au_{25} are referred to as (a) FCC1 and (b) FCC2, and the other one from SES-Au_{25} as (c) SES. FCC1 expands isotropically whereas FCC2 expands laterally in comparison with the initial structure of FCC-Au_{25}. The structure of SES is bent compared with that of SES-Au_{25}. As will be discussed later in detail, FCC2 is the most preferred structure of $[Au_{25}(SCH_3)_{18}]^+$. In the first place, I fully analyze the geometric and electronic structure of the FCC2 gold-thiolate cluster. Then, the obtained properties of FCC2 are compared with those of the other optimized gold-thiolate clusters, FCC1 and SES.

Table 2.1: The nearest neighboring interatomic distances of two bare Au_{25} clusters (FCC-Au_{25} and SES-Au_{25}), and of three optimized gold-methanethiolates (FCC1, FCC2, and SES).

distance(Å)	FCC-Au_{25}	SES-Au_{25}	FCC1	FCC2	SES
Au - Au	2.79 - 3.29	2.75 - 3.15	2.83 - 3.37	2.80 - 3.60	2.87 - 3.20
Au - S	—	—	2.39 - 2.72	2.39 - 2.43	2.38 - 2.41
S - C	—	—	$\sim$ 1.85	$\sim$ 1.85	$\sim$ 1.85
C - H	—	—	$\sim$ 1.09	$\sim$ 1.09	$\sim$ 1.09

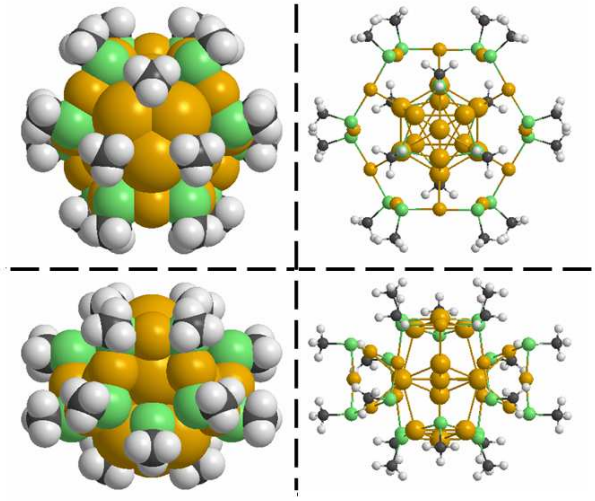

Figure 2.3: The top-view (above) and side-view (below) of the FCC2 in space-filling model (left) and ball&stick model (right).

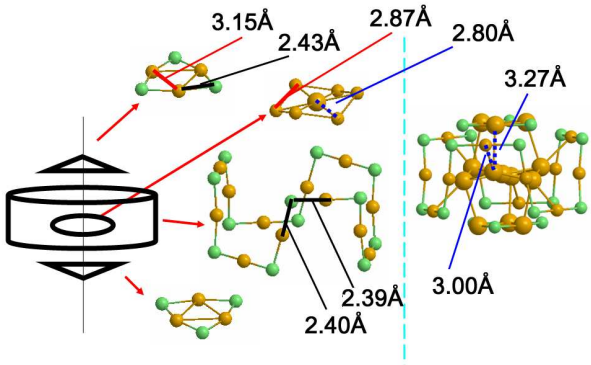

Figure 2.4: The four sub-systems of FCC2.

The best optimized geometrical structure of $[Au_{25}(SCH_3)_{18}]^+$

Figure 3 shows top and side views of FCC2 in different ways of drawing, "space-filling" and "ball and stick" models. FCC2 has an oblate structure and can be fractionalized into three subsystems; (i) a Au_7 core cluster, (ii) a $Au_{12}(SCH_3)_{12}$ ring, and (iii) two $Au_3(SCH_3)_3$ rings. This classification is schematically drawn in Figure 2.4. The almost planar Au_7 core cluster is surrounded by the $Au_{12}(SCH_3)_{12}$ ring. Then, the structure of FCC2 is completed by capping this core and ring subsystem from both sides of the top and the bottom with the two $Au_3(SCH_3)_3$ rings. The structural details of each fractionalized subsystem are as follows: (i) The Au_7 core cluster has a centered gold atom surrounded by a six-membered gold ring with a chair conformation. The Au-Au distance between the centered gold atom and each surrounding gold atom is 2.80 Å, and the distance between the nearest neighboring surrounding gold atoms is 2.87 Å. (ii) The $Au_{12}(SCH_3)_{12}$ ring consists of -Au-S- repeated bonds. The Au-S bond length is alternatively changed to either 2.39 Å or 2.40 Å. The nearest neighboring Au-Au distance is up to 3.60 Å. This Au-Au distance is significantly larger than that of usual bare gold clusters. (iii) The $Au_3(SCH_3)_3$ ring also consists of -Au-S- repeated bonds whose bond length is 2.43 Å, whereas the Au-Au distance is 3.15 Å. As is clear from these structural analyses, the present optimized gold-thiolate cluster consists of the core gold cluster and the $(Au\text{-}SCH_3)_n$ complex-like rings enclosing the core cluster. This feature is in sharp contrast to the widely known picture of gold-thiolate clusters that a core gold cluster is superficially protected by thiolate molecules. A similar finding was reported in a quite recent paper (ref [139]).

I continue the discussion of the stability of this optimized structure. From the vibrational analysis, it has been found that the structure has only one small imaginary frequency ($= 12.22\text{cm}^{-1}$). The existence of the imaginary frequency leads to the structural relaxation, which breaks the D_{3d} molecular symmetry. Thus, I have carried out geometry optimization again for FCC2 within C_s molecular symmetry to check a Jahn-Teller effect. As a result, the atomic rearrangements were very small, i.e., the largest one was only 0.004 Å. Therefore, I reasonably consider FCC2 to be acceptable for an energetically local minimum structure.

Before ending this subsection, the charging effect of $[Au_{25}(SCH_3)_{18}]^+$ on the geometric structure should be addressed. I have also carried out the geometry optimization of FCC2 in its neutral state. The calculated result showed that the structure of only the Au_7 core was slightly changed but the other $Au\text{-}SCH_3$ structures were almost unchanged. This is simply because not more than one or two charge differences are negligible at least for the geometric structure. Furthermore, I have confirmed that the charging effect does not have a qualitative influence on the XRD spectra. Although the explicit treatment of the spin multiplicity is mandatory for revealing magnetism or spin-dependent energy levels and there might be higher spin states that are lower in energy than the present closed shell structure, the charged (closed-shell) calculations provide reasonable results, as far as the geometric structure is concerned.

Comparison with the other optimized structures

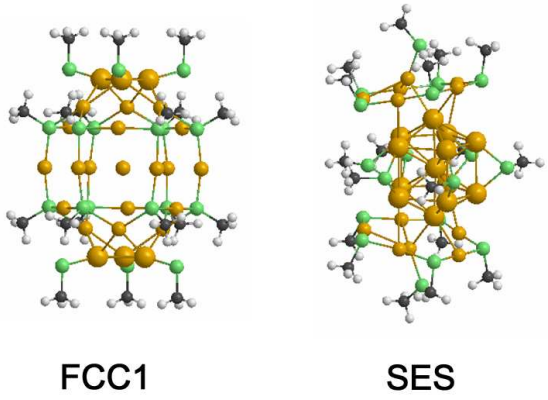

Figure 2.5: The structure of FCC1 and SES in "ball & stick" model.

In this subsection, I compare the geometric and electronic structures of FCC2 with those of the other optimized structures, FCC1 and SES. The structures of FCC1 and SES are shown in Figure 5, (see also Figure 2). As was mentioned in the beginning of this section, the deformation of the Au_{25} core structure caused by the coordination of the methanethiolates is commonly seen in FCC1 and SES. Such deformation is also found in the previous theoretical studies [137–140, 153] The gold and sulfur atoms in FCC1 and SES also form a -Au-S- repeated network.

FCC1 consists of fractionalized components of Au core and Au-S ring clusters as is similar to the structure of FCC2. However, there are two remarkable differences between the FCC1 and FCC2 structures. First, in FCC1 a methanethiolate coordinates to a gold atom rather than forming a $Au_3(SCH_3)_3$ ring. Second, the centered gold atom of the core cluster in FCC1 is localized markedly apart from the surrounding gold atoms by 4.60 Å. The result implies that the Au-Au interaction does not work any more, whereas the centered Au_7 core cluster in FCC2 plays an important role in stabilizing the structure of FCC2 as discussed later.

The structure of SES is more complicated than those of FCC1 and FCC2, and has a rather different geometric feature. Although it is difficult to fractionalize the whole structure, SES also consists of Au core and Au-S complex-like ring clusters. Therefore, the three optimized structures are similar to each other in a sense that they are constructed from a gold core cluster and Au-S complex-like ring clusters enclosing the core. However, FCC2 only provides the Au-S ring cluster with the ideal ratio of Au and SCH_3 being 1:1.

Figure 2.6 shows Kohn-Sham orbital energy levels of FCC1, FCC2, and SES as well as two core clusters of FCC-Au_{25} and SES-Au_{25}. The energies are indicated in units of eV relative to the energy of HOMO. I specify each component of the atomic

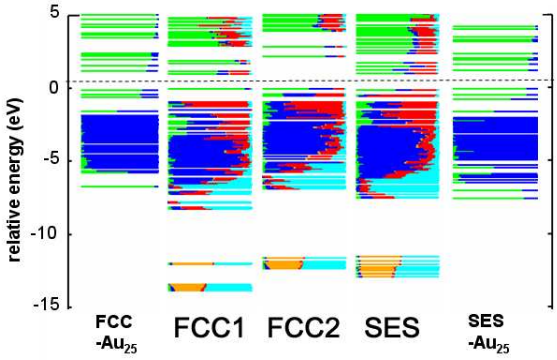

Figure 2.6: Kohn-Sham orbital energy levels of FCC-Au_{25}, FCC1, FCC2, SES, and SES-Au_{25}. The energies are indicated in the unit of eV relative to the HOMO energies. The orbitals colored in green, blue, yellow, red and light-blue represent Au($6sp$), Au($5d$), S($3s$), S($3p$), and CH_3 orbitals ,respectively. The broken line separate the occupied orbitals and the unoccupied orbitals. HOMO and LUMO are just under the line and just above the line, respectively.

orbitals contributing to the KS orbital energy levels by using different colors. The colors blue and green indicate Au $5d$ and $6sp$ orbitals, respectively, and the colors yellow, red and light blue S $3s$, $3p$, and methyl group orbitals, respectively.

The KS orbitals near HOMO and LUMO of the bare FCC-Au_{25} and SES-Au_{25} clusters are constructed mainly from the Au 6sp orbitals with small hybridizations of the Au 5d orbitals. The Au 5d band ranging from ca. -6 to ca. -2 eV is below the Au 6sp band. From the Mulliken population analysis, the central gold atoms of the bare clusters are negatively charged. The HOMO-LUMO gaps of both clusters are $\sim$1.2 eV.

Global features of the KS orbital energy levels of the three gold-methanethiolates can be classified into four groups from higher to lower in energy as follows: (i) the Au 6sp band, (ii) the Au (5d) - S (3p) bonding orbitals, (iii) the Au 5d band, and (iv) localized orbitals of the methanethiolate. The energy levels of HOMO, LUMO and the low-lying unoccupied orbitals belong to group (i). As is the case with the bare Au_{25} clusters mentioned above, the inside of the gold-methanethiolates is negatively charged. However, the negative charges in the gold-methanethiolates are smaller than those in the bare clusters. This is attributed to the charge transfer from the gold core to the thiolate molecule. This charge transfer was found to be the electronic transition from the Au(6s)-Au(6s) bonding orbital to the Au(5d6s)-S(3p) bonding orbital. The observed elongation of the Au-Au distance can be explained in terms of this charge transfer.

Table 2.2 shows the total energies and the HOMO-LUMO gaps of FCC1, FCC2 and SES. We can see that the total energy of FCC2 is lowest among these three energies.

Table 2.2: Total energies and HOMO-LUMO gaps of three optimized gold-methanethiolates, FCC1, FCC2 and SES.

	FCC1	FCC2	SES
E_{tot}(eV)	-306905.6	-306913.6	-306909.0
HOMO-LUMO gap(eV)	1.05	2.19	1.11

A surprisingly large HOMO-LUMO gap (2.19 eV) is found in FCC2. This energy gap is about twice as large as those of the other gold-methanethiolate clusters. From the orbital analysis, it has been found that HOMO, LUMO and LUMO+1 of FCC2 mainly consist of the atomic orbitals of the Au_7 core cluster. HOMO is composed of the 6s orbitals of the surrounding gold atoms and the 6p orbitals of the centered gold atom. These atomic orbitals interact with each other and split into bonding and antibonding orbitals. This strong interaction leads to the large HOMO-LUMO gap of FCC2.

Comparison with experimental data:
XRD and absorption spectra

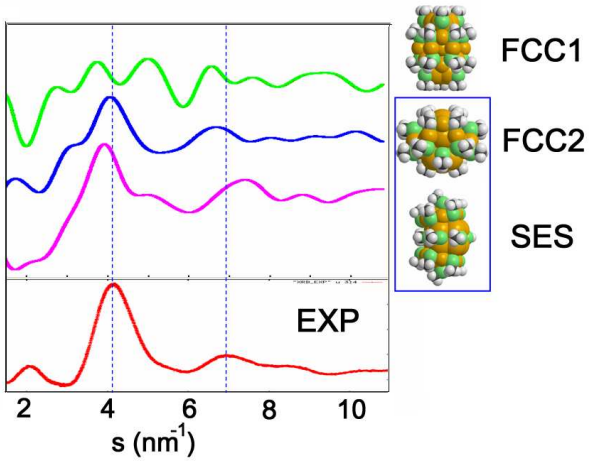

Figure 2.7: Experimental diffraction spectrum (below, labelled "EXP") and diffraction spectra calculated from optimized geometry of the gold-methanethiolates: FCC1, FCC2 and SES. The diffraction spectra in each case are displaced along the vertical axis for clarity of exposition.

Figure 2.7 shows the XRD spectra of the present three optimized structures in comparison with the experimental data [151]. The global features of the spectra of FCC2 and SES are qualitatively in good agreement with the experimental data. Furthermore, the spectrum of FCC2 provides two major peaks ($\sim$4 and $\sim$7 nm^{-1}) which reasonably coincide with the experimental ones (see, the vertical dotted lines). Here, I should

stress that $Au_{25}(SG)_{18}$ was highly purified, so that the experimental XRD spectrum reflects only this size of the cluster. Thus, it is not necessary to take account of the size distribution of the clusters depending on the experimental conditions. Although the qualitative agreement of the calculated FCC2 XRD spectrum with the experimental one should not be taken as a final proof of the existence of the FCC2 structure, this result will be utilized when totally judging the most probable $[Au_{25}(SCH_3)_{18}]^+$ structure.

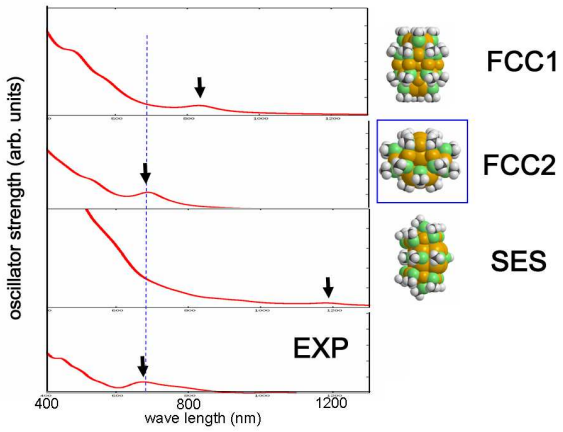

Figure 2.8: Absorption spectra of FCC1, FCC2, SES, and experiment(below, labelled "EXP"). The solid lines are obtained by convoluting each absorption peak with the Lorenz function for FCC1, FCC2 and SES. For convenience, the broken line is drawn to comparison for the absorption peaks.

Figure 2.8 shows the comparison of the calculated absorption spectra with the experimental data [151]. The solid lines are obtained by convoluting each absorption peak with the Lorentz function. The first major peaks of the spectra are indicated by arrows. As is clearly seen from the figure, the absorption spectrum of FCC2 sufficiently reproduces the experimental data. The first peak at 689 nm and the shoulder at 534 nm are assigned to the electronic transitions that occurred within the Au_7 core cluster. The first peak corresponds to the electronic excitation from HOMO to LUMO, and the shoulder from HOMO to LUMO+1.

Brief summary

FCC2 was decided to be the most plausible geometry for the $Au_{25}(SCH_3)_{18}$ by the careful investigations on the electronic structure, total energy, and comparisons between experiments. The following sections study further the electronic and optical properties of FCC2 by using unrestricted DFT calculations.

2.1.3 Electronic properties

Let me briefly review the unique geometrical structure of $[Au_{25}(SCH_3)_{18}]^+$ obtained in the previous section. The cluster consists of a Au_7 core and a $(AuSCH_3)_{12}[(AuSCH_3)_3]_2$ cage structure as shown in Fig. 2.9. The Au_{25} cluster is effectively reduced to the Au_7 core owing to a coordination of the eighteen thiolates. Then, the Au_7 core takes a nearly planar structure and the remaining outer gold atoms together with the thiolates form a robust complex-like cage composed of one $Au_{12}(SCH_3)_{12}$ ring with a zig-zag (-Au-S-) framework and two planar $Au_3(SCH_3)_3$ rings. As will be numerically confirmed later, this structure is almost unchanged in the different charged states and these unique structural features play a very important role in realizing the spin polarization localized at the Au_7 core.

Magnetism

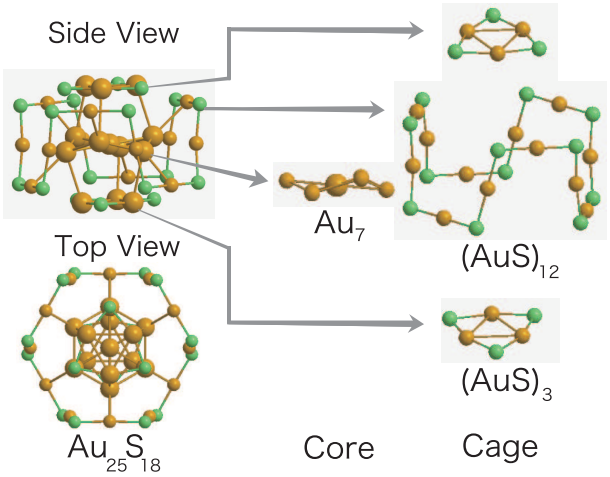

Figure 2.9: The optimized geometry of $[Au_{25}(SCH_3)_{18}]^+$ consisting of Au_7 core and $(AuSCH_3)_{12}[(AuSCH_3)_3]_2$ cage structure: Au (gold) and S (green). For simplicity, the methyl groups are not shown in this figure.

I started from the geometry optimization of the neutral cluster, $Au_{25}(SCH_3)_{18}$ by resorting to unrestricted DFT calculations. The ground state of the cluster was found to be the doublet state. Figure 2.10(a) shows the density of state (DOS) for the up [red lines] and down [blue lines] electron spins. The short vertical line denotes the Fermi energy level. As shown in the figure, the KS orbital analysis indicates that the curves of DOS are classified into three regimes contributed mainly from (i) the Au(5d) orbitals, (ii) the Au(5d)-S(3p) bonding orbitals, and (iii) the Au(6s, 6p) orbitals of the Au_7 core. The figure shows that the one unpaired electron (up spin in this figure) is localized at the Au_7 core, and the red and blue curves of DOS for Au(5d) and Au(5d)-S(3p) are almost symmetrical. The highest occupied molecular orbital (HOMO), containing one up-spin electron in the present unrestricted DFT calculations, of the neutral (n=0)

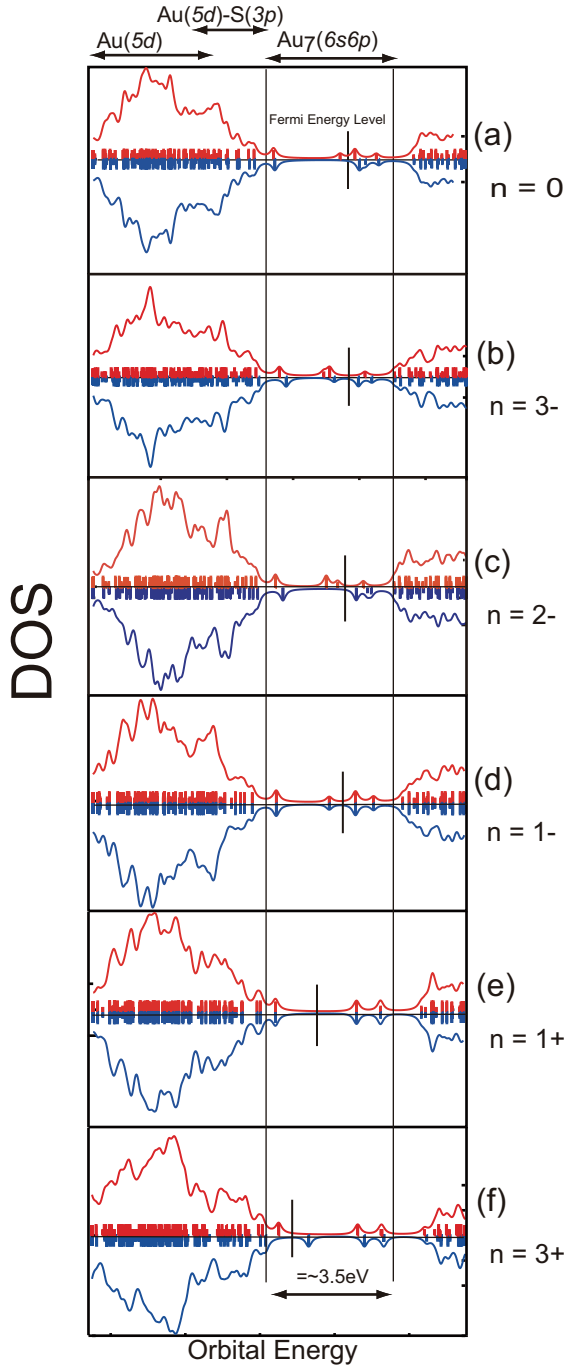

Figure 2.10: Density of States for the up (red) and down (blue) spins of the charged clusters $[Au_{25}(SCH_3)_{18}]^n$. For comparison purposes, the absolute values of the orbital energies are conveniently shifted in each figure. The short vertical lines denote the Fermi energy level. All the DOSs were obtained by convoluting each KS energy level (indicated by the red and blue vertical lines) with the Lorentz function.

cluster depicted in Figure 2.11 schematically demonstrates that the unpaired electron is indeed localized at the Au_7 core and almost no electron density exists around the Au-S cage. For these reasons, it is not expected that the magnetic moment is induced at the surface of the gold-thiolate cluster. This is a sharp contrast to the observations in gold-thiolated surfaces or thin films in which the giant magnetic moments were induced by the localized electrons transferred from the gold substrate to the sulfur atom, but is consistent with what was obtained by Yamamoto *et al*. If we consider the electrons confined in the Au_7 core as "trapped electrons" proposed by Hernando *et al*., their explanation also seems to be consistent with the present result. Negishi *et al*. reported that the magnetic moments in the Au-SG clusters were induced by the localized electrons in the Au-S bonds and estimated them to be 0.0093 μ_B. Such a small value is consistent with the above calculated result that the significant magnetic properties are not induced at the surface of the small gold-thiolate cluster.

I have carried out geometry optimizations of the cluster in n = $3-, 2-, 1-, 1+$ and $3+$ charged states. It has been confirmed that these optimized structures are very similar to that of the neutral cluster except that the structure of the Au_7 core slightly winds depending on the charged states. This is because the Au-S cage enclosing the Au_7 core forms a rather rigid framework as described in the previous section. The HOMO-LUMO (lowest unoccupied molecular orbital) gaps and the spin multiplicities of all the charged gold-thiolate clusters are summarized in Table 1. It should be noted that these HOMO-LUMO gaps do not necessarily correspond to an absorption edge because LUMO may have a different spin against to HOMO. It is worth noting that spin polarization is realized in the higher charged states. To analyze each spin-polarized state, I will compare DOSs of the charged clusters with each other in Figs. 2.10(b)-(f). As in DOS of the neutral cluster (Fig. 2.10(a)), the red and blue curves of the Au(5d) and Au(5d)-S(3p) regimes are almost symmetrical indicating that the up and down spins form a pair. In contrast, DOSs associated with the Au_7 core depend on the charged states and particularly DOSs for the up and down spins in the charged states of $3-, 2-$, and $3+$ are asymmetrical. These spectral patterns show that the spin polarization is realized in such charged states. Furthermore, the unpaired electrons contributing to these spin-polarized states are localized at the Au_7 core. Figure 2.11 shows the KS orbitals related to the spin-polarized states. This figure schematically demonstrates that the unpaired electrons are localized at the core but not distributed around the Au-S cage.

Table 2.3: The HOMO-LUMO gaps and the spin multiplicities of $Au_{25}(SCH_3)_{18}$ in different charged states. The spin multiplicities are given in terms of $(2S + 1)$ with S being the total spin quantum number.

charge	$3-$	$2-$	$1-$	0	$1+$	$3+$
HOMO-LUMO gap (eV)	0.6	0.5	0.7	0.4	2.2	0.8
$2S + 1$	3	4	1	2	1	3

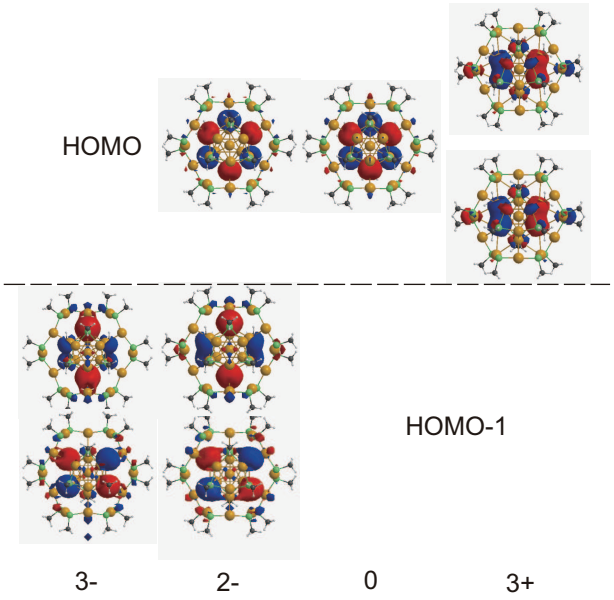

Figure 2.11: The top views of the KS orbitals associated with the unpaired electron. The orbitals are either HOMO or HOMO-1. The orbitals for n = 3- (HOMO-1), n = 2- (HOMO-1), and n = 3+ (HOMO) are doubly degenerate.

To illustrate the magnetic properties of the gold-thiolate cluster more clearly, I show in Figure 2.12 contour plots of the spin densities of the different charged states of 3−, 2−, 0, and 3+. The spin densities in the figure are given as difference between the up (red) and down (blue) electron spin densities. All the up spin densities (red) associated with the Au(6s) orbital are localized in the outer part of the Au_7 core. Very small (almost negligible) spin densities (ρ = -0.004e) mainly consisting of the down spin distribute around the Au_7 core. The contour plots for the charged states of 3-, 2-, and 3+ clearly show that the inhomogeneous spin distributions are localized in the Au_7 core. In particular, in the charged state of 2-, the up spin densities associated with the Au(6s) orbital distribute around the Au_7 core ring whereas the down spin densities are localized at the core. In contrast, in the contour plot of the neutral state, the spin density distribution becomes very subtle. All these spin density maps completely reflect the results described above, that is, the high-spin polarizability is realized in the charged state of 2- and the corresponding inhomogeneous spin densities distribute in the Au_7 core.

Following the explanations by Vager and Naaman, and Hernando *et al.*, the key ingredient to understand the magnetism is the giant magnetic moments. Such magnetic moments can be induced under the conditions that spin-polarized electrons are localized and magnetic anisotropy exists. These conditions are also satisfied in the present gold-thiolate cluster. The spin-polarized electrons are localized at the Au_7 core and the anisotropy is expected because the Au_7 core has an almost planar structure. Furthermore, since the Au_7 core is enclosed by the robust Au-S cage, the spin-polarized

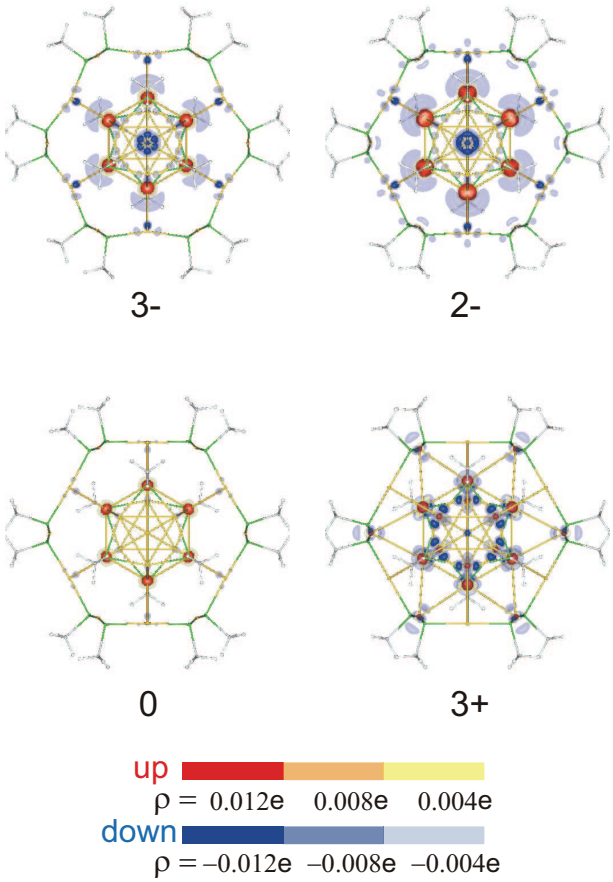

Figure 2.12: The top views of contour plots of the spin densities given as difference between the up and down electron spin densities. The charged states are 3-, 2-, 0, and 3+, respectively.

electrons will still be localized when the gold-thiolate cluster condenses to form larger compounds. The charged states of the gold-thiolate cluster are changed by introducing positive or negative counter ions. Therefore, the gold-thiolate compounds with unusual magnetism can be constructed by building up the gold-thiolate cluster $Au_{25}(SCH_3)_{18}$ through controlling the charged states.

Absorption spectra

Figure 2.13 shows absorption spectra of **1**, **2**, and **3** to the left and the corresponding experimental spectra to the right. The calculated absorption peaks were convoluted by the Lorentz function with a width of 40 nm. The first peak appears at $\sim$ 680 nm, irrespective of the charged state, whereas there is a glimpse of peaks around 800 nm both in the spectra of **2** and **3**. The spectral patterns are in good accord with the experimental one. Peak patterns of **1** and **3** are relatively similar, and of **3** shows peak splitting around 680 nm. To analyze these spectral patterns, KS-orbitals concerning

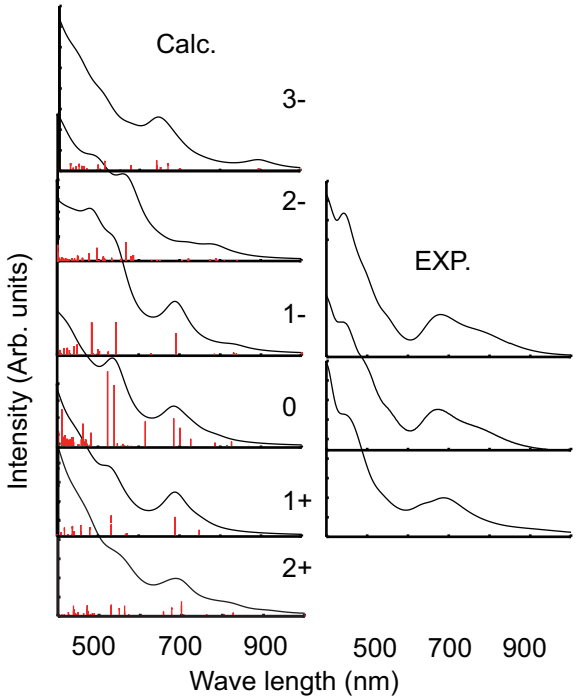

Figure 2.13: Absorption spectra of $Au_{25}(SCH_3)_{18}$ of calculated (left) and experimental (right) in the charged states are shown.

to the first peaks will be analyzed below.

Although, KS-orbital is just a mathematical tool and has little physical meanings, it is not so bad to use them for qualitative interpretation of molecular orbitals if we restrict ourselves to the discussion near the Fermi level [154]. To confirm this, I have performed HF/TZVP calculation on 1+ cationic state in closed shell model and compared the result with that of B3LYP/TZVP. Moreover, the MP2 calculation following to the HF/TZVP calculation shows the largest changes in occupation numbers of 5.79 %. This suggests that the HF occupations are acceptable in this gold-thiolate system and the comparison between HF and DFT calculations can make a sense. From the comparisons, I have obtained that the orbital orders around the Fermi levels are the same and the orbital shapes are indistinguishable. The HOMO-LUMO gaps and energy differences between HOMO(= HOMO-1) and HOMO-2 in HF calculation are larger than B3LYP one. Thus, the KS-orbital analyses on the absorption spectra provide good qualitative and intuitive pictures.

Figure 2.14 shows the KS orbital diagrams concerning to the first peaks. Some representative electronic transitions associated with the absorption peaks in Fig.2.13 are assigned. All the charged states have the same KS orbital characters with minor relaxations thorough varying the charges as reported experimentally [5, 91]. In **2** and **3**, the frontier electrons occupy LUMO of **1** which is doubly degenerated in nature. While such occupation breaks the closed shell structure of **1**, the electronic structure

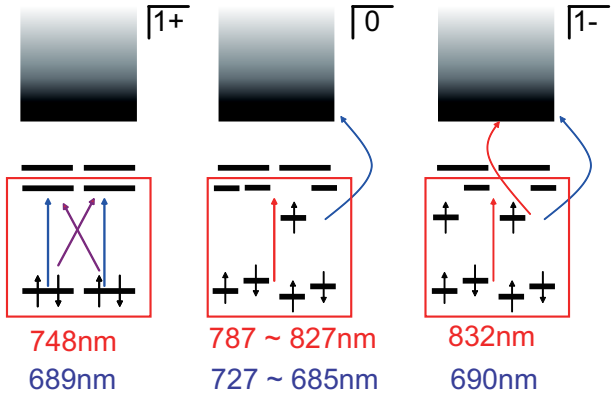

Figure 2.14: HOMO-LUMO

of **3** has quasi-closed shell character. The electronic transitions of the first peak of **1** is attributed to the HOMO-LUMO transitions, both HOMO and LUMO are composed mainly of Au_7. In the spectra of **2** and **3**, the first peaks are attributed to the transition from KS orbitals of Au_7 to Au(6s) of the Au-S cages, and the small peaks around 800 nm correspond to the first peak of **1**. The peak splitting observed around 680 nm in **2** can be explained by the disordered electronic structure compared to the other charged states, but having minor effects on the spectral curve. Thus, it can be concluded that the similarity in the peak positions between the spectra of **1**, and **2** and **3** are just a coincidence, which arise from the similarity of the relative spacing of the energy levels concerned. In contrast, the similarity between **2**- and **3**- spectra results from the same nature in the electronic configurations and transitions.

2.1.4 Short summary

I have presented the DFT study of the model cluster $[Au_{25}(SCH_3)_{18}]^+$ mimicking the extraordinarily stable glutathione(GSH)-protected gold cluster $Au_{25}(SG)_{18}$ experimentally observed very recently [1–3]. Three types of optimized structures were derived from the different core clusters of the fcc Au_{25} and of the vertex-sharing centered icosahedral Au_{13} dimer. The most preferred optimized structure, FCC2, which is based on the truncated fcc Au_{25} cluster, shows the unusually large HOMO-LUMO gap and sufficiently reproduces the experimental data of the XRD and absorption spectra. I have found that FCC2 can be partitioned into three types of subsystems, the Au_7 core cluster, the $Au_{12}(SCH_3)_{12}$ complex-like ring, and the two $Au_3(SCH_3)_3$ rings. This classification leads to a novel structural picture that the bare gold cluster is enclosed by the -Au-S- repeated network. Such a structural understanding reveals the physicochemical properties of small thiolated gold clusters in a new and different way.

The unrestricted DFT calculations have been performed to investigate the spin-polarized electronic structures of the core-in-cage geometry, $Au_7(AuSCH_3)_{12}[(AuSCH_3)_3]_2$,

with different charged states from 3− to 3+. While the spin multiplicity ($2S+1$) of the neutral cluster is 2, the higher-spin polarization is realized in the charged states. Furthermore, the unpaired electrons associated with these high spin-polarized states are always localized at the Au_7 core that is encapsulated by the robust Au-S cage. Therefore, we can control the degree of spin polarization by changing the charged states of the gold-thiolate cluster by introducing counter ions. The cluster will induce magnetic anisotropy due to the planar geometry of the Au_7 core even when integrated. Such controllable magnetic moments localized at the core cluster can be utilized to develop single molecule magnets and also magnetic storages by building up the gold-thiolate clusters. Optical absorption spectra of the charged states reproduce the experimental spectral curve in a good manner. Analysis of the absorption spectra with the electronic structure classifies the similarity of the peak position between cationic and the other states a coincidence. On the other hand, the anionic and neutral state have same electronic configurations leading the similar absorption spectral patterns having same peak positions and shoulders over the first peak. From the total energy differences, IP, EA, and VDE are estimated, from which I conclude that the anionic state can also be observed in a gas phase. Beyond the structural motif discovered at large gold-thiolate cluster, the cluster around 1 nm shows distinct geometrical feature and electronic properties and this suggests a need for more detailed analysis by experimental and theoretical works. These fabricated gold-thiolate clusters open up the new class of functional cluster material science.

2.2 Au_{13} oligomeric clusters

Tsukuda and coworkers made significant progress toward realizing the cluster-assembled compounds in a bottom-up approach [6]. They synthesized a gold cluster compound $[Au_{25}(PPh_3)_{10}(SC_2H_5)_5Cl_2]^{2+}$ (**1**) and characterized its geometric structure through single X-ray crystal analysis. The cluster has a unique structure in the sense that the Au_{25} core is constructed by bridging two icosahedral Au_{13} clusters with thiolates sharing a vertex gold atom and is terminated by two chlorine atoms. This biicosahedral structure is conceptually close to the clusters of clusters by Teo et al., and thus it is considered to be a dimer consisting of the two icosahedral Au_{13} units. The absorption spectrum showed that such dimerization gives rise to a new electronic level retaining the electronic properties of the individual Au_{13} constituents. Therefore, the icosahedral Au_{13} cluster incorporating with thiolates will be a typical prototype of building blocks of assembled gold clusters.

In this section, characterization of geometric and electronic structures of a dimer cluster $[Au_{25}(PH_3)_{10}(SCH_3)_5Cl_2]^{2+}$ (**2**) mimicking the cluster **1** will be discussed. Then, the mechanism of the dimerization will be studied theoretically. I will further discuss polymerization, as an example, the trimerized gold cluster $[Au_{37}(PH_3)_{10}(SCH_3)_{10}Cl_2]^{+}$.

2.2.1 Method of computation

Density functional theory (DFT) calculations have been carried out for the gold cluster **2**. In this model cluster, the triphenylphosphines of **1** were replaced with the phosphines, and the alkanethiolates were replaced with the methanethiolates. I have adopted such a simplification of the ligands frequently used in previous calculations [135,137,139,140,155,156]. Geometry optimization of the cluster **2** was performed starting from the initial guess structure taken from the single-crystal X-ray data of **1**. This initial structure is closed to C_{5h} molecular symmetry. I did not assume such a high molecular symmetry but performed the geometry optimization of the cluster within C_s molecular symmetry.

I should refer to the accuracy of the present DFT calculations with the B3LYP functional. The determination of the most preferable functional, particularly for heterogeneous clusters such as the present metal-molecule compounds, is beyond the scope of the present work. I have confirmed that at least for the present gold cluster compounds, the calculations with B3LYP compared with the PBE functional [157] reasonably reproduced the experimental results. Although the optimized structure based on the calculation with PBE is in slightly better accord with the experimental result, the calculation failed to reproduce the detailed absorption spectral patterns of the experiment. For references of comparison of functionals in gold-thiolate compound systems, see [139] and the following papers [153, 158]

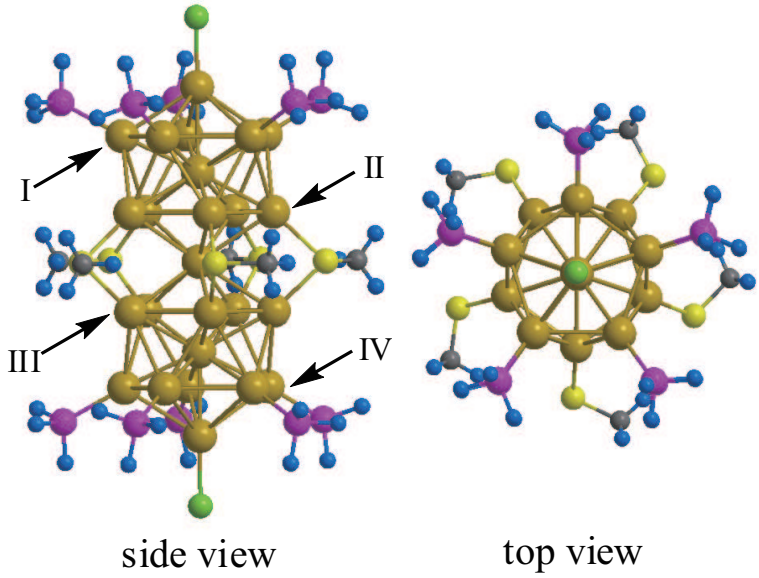

Figure 2.15: Side and top views of the optimized dimer structure of **2**. The colored balls represent constituent atoms: Au (gold), S (yellow), C (gray), H (blue), P (magenta), Cl (green).

2.2.2 Geometrical structures

Figure 1 shows side and top views of the optimized structure of **2**. In addition to this optimized structure, I have obtained other local minimum structures where the bond directions of the ligands (SCH_3 and PH_3) to the gold atoms are slightly different. This optimized structure has been computationally confirmed to be energetically most stable and has negligible imaginary frequencies with magnitudes less than 20 cm^{-1}, which are primarily associated with the vibrational motion of the C-H or P-H bonds. Although the geometry optimization has been carried out within C_s molecular symmetry, the optimized structure was close to C_{5h} molecular symmetry. This result implies that the optimized structure can still have high molecular symmetry and a lower energy minimum cannot be achieved even when the geometry optimization is carried out without the use of symmetry. For convenience, the four layers (I-IV denoted in Figure 1) of the gold pentagonal rings were labeled. The two icosahedral Au_{13} clusters are clearly bridged (between II and III layers) by the methanethiolates sharing a vertex gold atom and are terminated by the chlorine atoms. This structure is in good agreement with the experimental X-ray data of **1**. The methyl groups are bound to the sulfur atoms in an orientation similar to blades of a rotary fan. The top view in Figure 1 shows that the methyl groups (yellow-gray-blue balls) are aligned counterclockwise. Although this feature was not discussed in the experimental study [6], the illustration of the X-ray data of **1** also shows that the alkyl groups are aligned clockwise or counterclockwise.

Table 2.4: Structural and electronic properties of the calculated dimer and trimer clusters in comparison with the experimental data of **1**.

	dimer	trimer	expt. [6]
Au-Au (Å)	2.86 - 3.04	2.84]3.06	2.70 - 3.00
layer II - III (Å)	3.35	3.35	2.94 - 3.11
Au-S (Å)	2.47	2.47	2.36 - 2.43
Au-P (Å)	2.4	2.4	2.28 - 2.35
Au-Cl (Å)	2.37	2.37	2.38 - 2.42
Au-S-Au (deg)	85.4	85.1	75.7 - 80.9
Au-S-C (deg)	105.5	105.2	99.4 - 107.1
HOMO-LUMO gap (eV)	2.13	1.362	

Table 1 summarizes representative structural and electronic properties of **2** in comparison with the experimental ones. The theoretical structural properties are in good agreement with the experimental values, with the exception of a small difference in the Au-Au distance between the layers II and III. The bulky ligands of the triphenylphosphine in the cluster **1**significantly twist the Au_{13} icosahedral structure [6] compared with the methanethiolate ligands in the model cluster **2**. The distortion partly makes the Au-Au distance shorter in the cluster **1**.

The stability of the +2 cationic state of **2** is substantially based on closed-shell requirements. The calculated HOMO−LUMO gap of the cluster is large (2.13 eV) as shown in Table 1, whereas the electronic energy levels adjacent to HOMO are degenerate or close to each other because of high molecular symmetry of **2**. This is also true for the energy levels adjacent to LUMO. Just enough electrons in the +2 cationic state form a closed-shell structure, and therefore the +2 cation is more stable than other charged states. The stability can be also understood by using Mingos's electron counting rule [159]. This rule explains stability of clusters in terms of closed-shell requirements based on a jellium model. More specifically, the total number of valence electrons in a cluster consisting of vertex-sharing icosahedrons is given by $8n_p$, where n_p is the number of icosahedrons [159, 160]. The 16 valence electrons in the present cluster **2** fulfill the counting rule, and thus the cluster can be regarded as a dimer of a closed-shell, 8-electron system.

2.2.3 Optical properties

Figure 2.16a shows the absorption spectrum of the cluster **2** in comparison with (b) the experimental spectrum of **1**. The calculated spectrum was obtained by convoluting each absorption peak (vertical lines) with the Lorentz function. The calculation reasonably reproduces the peak positions and the shoulder structures observed in the experiment. The first peak on the theoretical absorption spectrum appears at 702 nm, well apart from other absorption peaks in the higher energy region (< 600 nm). This peak was found to be assigned to an electronic transition between the HOMO−LUMO

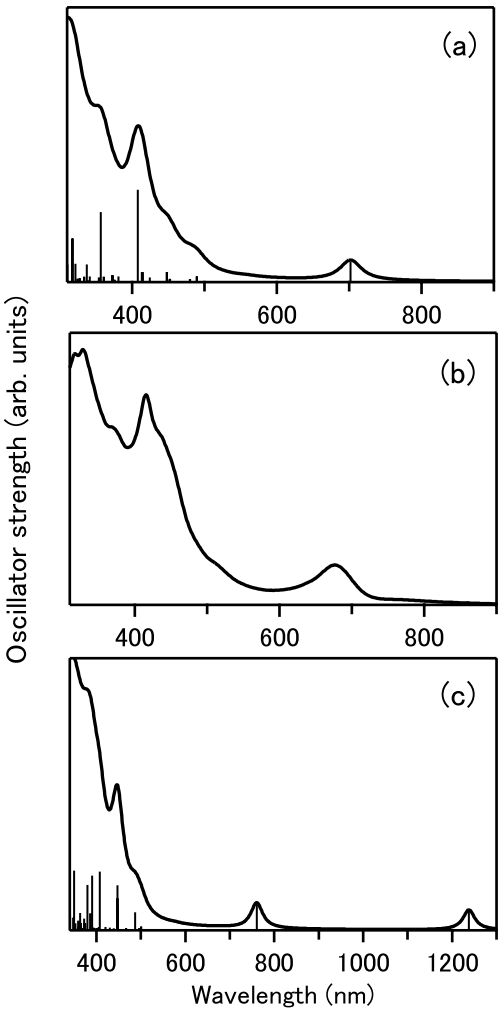

Figure 2.16: Absorption spectrum of (a) the dimer cluster **2** in comparison with (b) the experimental measurement of **1**. (c) Absorption spectrum of the trimer cluster **3**.

energy levels due to the vertex-sharing biicosahedral structure. The icosahedral Au_{13} cluster is spherically symmetric in origin, and thus its atomic orbitals along the x, y, and z axes are triply degenerate. In the biicosahedral structure, however, the symmetry breaks and then the atomic orbitals along the long molecular axis, such as the z axis, are lower in energy whereas those along x and y axes are higher in energy. Because the spherically symmetric s-orbitals are not affected by the symmetry breaking, their orbital energies do not change. Figure 2.17a shows the HOMO and LUMO of cluster **2**. The HOMO is constructed mainly from atomic orbitals along the z axis, and the LUMO consists of primarily s orbitals localized around the vertex gold atom at the center. Both electronic states of the HOMO and LUMO are attributed to the interaction between the two vertex-sharing Au_{13} icosahedrons induced by the symmetry breaking. Therefore, the absorption peak at 702 nm is assigned to a new electronic transition due to the dimeric structure. The absorption peaks in the higher energy

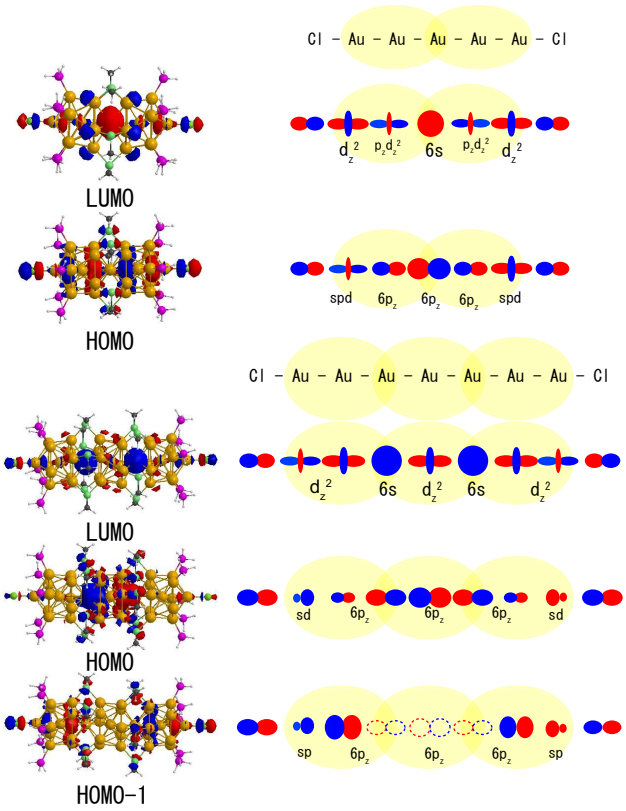

Figure 2.17: Schematic diagrams of the KS orbitals and main atomic orbital components contributing to each KS orbital: (a) the dimer cluster **2** and (b) the trimer cluster **3**. The atomic orbital components of HOMO-1 in the trimer partly cancel each other owing to their opposite phase (dotted orbitals).

region ($<$ 600 nm) were, however, assigned to the electronic transitions within the individual Au_{13} cluster unit.

The present cluster **2** has a peculiar structure that the Au_{25} core seems to be a dimer of the vertex-sharing Au_{13} icosahedron bridged by the methanethiolates. A natural question then arises whether oligomeric structures of more than the dimer can be achieved. To answer this question, I have further carried out geometry optimization of a trimeric structure within C_i molecular symmetry in the same way as in the biicosahedral cluster. The triicosahedral gold cluster of $[\,Au_{37}(PH_3)_{10}(SCH_3)_{10}Cl_2]^+$ (**3**) was obtained successfully with only one negligible imaginary frequency, with a magnitude of $\sim$10 cm^{-1}. The optimized structure was close to S_{10} molecular symmetry. At the present level of calculation, the +1 cationic structure was well-converged. The stability of the +1 cationic state is explained in terms of closed-shell requirements as in the case of the biicosahedral cluster mentioned above. In addition, the total number of valence electrons (=24) in the +1 cationic state also satisfies Mingos's electron counting rule ($24 = 8 \times 3$ (the number of icosahedrons)). In other words, the +1 triicosahedral cluster can be regarded as a trimer of a closed-shell, 8-electron system.

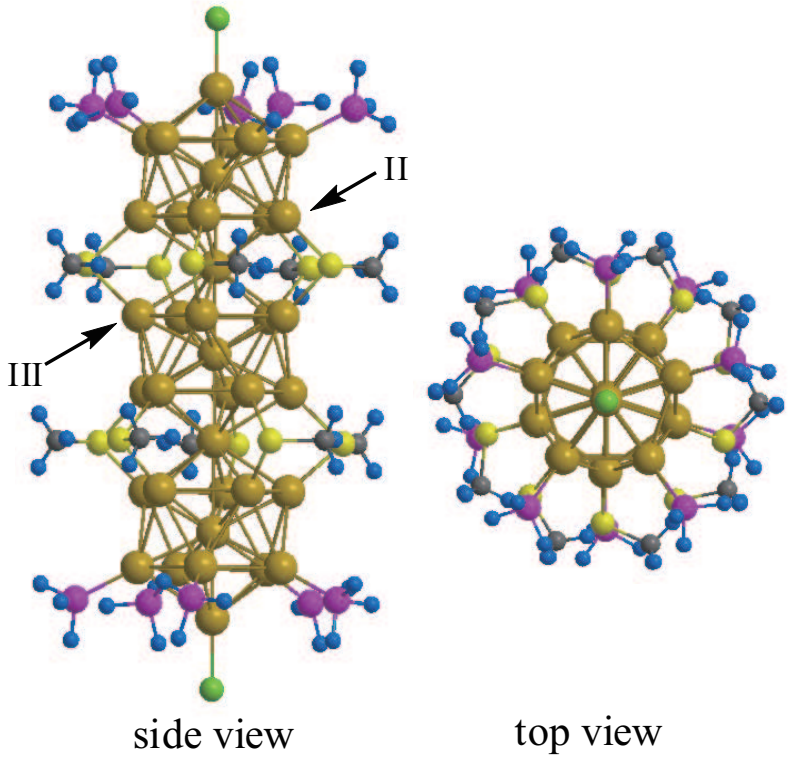

Figure 2.18: Same as Figure 1 but for the trimer structure of **3**.

Figure 2.18 shows side and top views of the optimized structure of **3**. Similar to the structure of **2**, the three icosahedral Au_{13} clusters are bridged by the methanethiolates sharing vertex gold atoms at two different sites and terminated by the chlorine atoms. The top view in Figure 2.18 shows that the methanethiolates are also aligned counterclockwise. The structural properties of **3** summarized in Table 1 are very similar to those of **2**. This suggests that the triicosahedral gold cluster is also constructed from the vertex-sharing Au_{13} icosahedrons and their individual properties remain almost unchanged.

In Figure 2.16c, the absorption spectrum of **3** is plotted. The spectral pattern in the range less than 600 nm resembles that of **2** except that the spectrum is shifted toward higher wavelength. Alternatively, two peaks appear at 761 and 1238 nm. The second peak at 761 nm seems to correspond to the red-shift of the first peak at 702 nm in the spectrum of **2**. However, this peak is assigned to a new electronic transition due to the trimeric structure. Figure 2.17b shows the HOMO, HOMO-1, and LUMO of **3**. As described for the biicosahedral cluster, the HOMO and HOMO-1 consist of atomic orbitals along the z axis, and the LUMO is constructed primarily from the s orbitals at two different sites on the vertex gold atoms. In particular, the HOMO extends along a quasi-one-dimensional gold chain aligned along the z axis. The first peak at 1238 nm is assigned to the HOMO−LUMO electronic transition, and the second one

at 761 nm is assigned to the HOMO-1 - LUMO electronic transition. Therefore, the two peaks in the triicosahedral structure appear because the three vertex-sharing Au_{13} icosahedrons interact with each other through two different vertexes.

2.2.4 Short summary

I have presented the DFT study of geometric and electronic structures of a gold cluster compound $[\ Au_{25}(PH_3)_{10}(SCH_3)_5Cl_2]^{2+}$. The optimized structure is considered to be a biicosahedral cluster consisting of two icosahedral Au_{13} clusters bridged by methanethiolates sharing a vertex gold atom and terminated by chlorine atoms. This geometrical structure is in good agreement with the experimental observation. I have further demonstrated that a triicosahedral structure $[\ Au_{37}(PH_3)_{10}(SCH_3)_{10}Cl_2]^{+}$ was achieved. The geometric properties of the bi- and the triicosahedral gold clusters are very similar to each other. Furthermore, a comparison between the absorption spectra of the two structures has revealed that the new electronic levels due to each oligomeric structure appear sequentially, whereas other electronic properties remain almost unchanged compared to the individual icosahedral Au_{13} cluster. The cluster-assembled compounds are expected to be derived as an extension of the present oligomeric gold clusters.

Chapter 3

Development of optical response theory

This chapter focuses on the development of optical response theory of nanoclusters in a nonuniform electric field, with the aim of studying near-field electronic excitations. At first, I will make clear the problems to be addressed when we study optical response of clusters at the 1 nm scale.

3.1 Problems to be addressed

I have obtained the static properties of the constituent building blocks, in both isolated and assembled states, such as geometric and electronic structures, and photoabsorption spectra using the gold cluster compounds. To achieve cluster-based devices at the 1 nm scale, the next step is to gain a further insight into the dynamical optical properties of cluster compounds, in particular for discussing photoinduced dynamics in nanoclusters or nanocluster assemblies, we should have proper understanding of an inter-cluster near-field interaction. The conventional light-matter interaction based on available lasers is quite different from the near-field interaction because the wavelength is much longer than the size of the local structure of the cluster compounds. In other words, the 1-nm-sized cluster compounds feel the almost uniform electromagnetic field and thus the local structures of the compounds cannot be resolved in space. In contrast, a near-field interaction is a nonuniform light-matter interaction and this is not well described by the conventional optical response theory. For these reasons, I will develop optical response theory applicable to 1-nm-sized clusters beyond the diffraction limit of wavelengths of the available visible lasers.

3.2 Multipolar Hamiltonian

The multipolar Hamiltonian can be derived from the minimal-coupling Hamiltonian by performing a canonical transformation [161–163] and has an advantage over the minimal-coupling one in the sense that the light-matter interaction is described in terms of the scalar product of a polarization $\boldsymbol{P}$ and an electric field $\boldsymbol{E}$ with a compact analytical expression. In the multipolar Hamiltonian form, we can utilize an electric field, which can be directly observed, instead of using vector potential and momentum as in the case of the minimal-coupling Hamiltonian. It should be noted that in this study the electric field is considered to be a classical value and any magnetic interactions are neglected. According to Ref. [163] and Appendix A, the multipolar Hamiltonian of molecules interacting with an electric field is obtained as

$$\hat{H} = \hat{H}_{\mathrm{mol}} + \hat{V}_{\mathrm{inter}} - \int d\boldsymbol{r} \hat{\boldsymbol{P}}(\boldsymbol{r}) \cdot \boldsymbol{E}^{\perp}(\boldsymbol{r}), \tag{3.1}$$

where $\hat{H}_{\mathrm{mol}}$ is the Hamiltonian of the molecules and $\hat{V}_{\mathrm{inter}}$ is the static intermolecular Coulomb interaction. $\hat{\boldsymbol{P}}(\boldsymbol{r}) = \sum_i \hat{\boldsymbol{P}}_i(\boldsymbol{r})$ is the total polarization operator of the system with $\hat{\boldsymbol{P}}_i(\boldsymbol{r})$ being the polarization operator of the molecule i. $\boldsymbol{E}^{\perp}(\boldsymbol{r})$ is the transverse part of the electric field written in the form of

$$\boldsymbol{E}^{\perp}(\boldsymbol{r}) = \boldsymbol{E}^{\perp}_{\mathrm{laser}}(\boldsymbol{r}) + \sum_j \boldsymbol{E}^{\perp}_j(\boldsymbol{r}), \tag{3.2}$$

where $\boldsymbol{E}^{\perp}_{\mathrm{laser}}$ is an incident laser field and $\boldsymbol{E}^{\perp}_j$ is the induced electric field due to the response of the j-th molecule to the incident laser field. The static intermolecular Coulomb interaction is given by

$$\hat{V}_{\mathrm{inter}} = \frac{1}{\varepsilon_0} \sum_{i<j} \int d\boldsymbol{r} \hat{\boldsymbol{P}}^{\parallel}_i(\boldsymbol{r}) \cdot \hat{\boldsymbol{P}}^{\parallel}_j(\boldsymbol{r}), \tag{3.3}$$

where $\hat{\boldsymbol{P}}^{\parallel}_i(\boldsymbol{r})$ is the longitudinal part of $\hat{\boldsymbol{P}}_i(\boldsymbol{r})$. Then, Eq.(3.1) is rewritten as

$$\begin{aligned} \hat{H} = \hat{H}_{\mathrm{mol}} &+ \frac{1}{\varepsilon_0} \sum_{i<j} \int d\boldsymbol{r} \hat{\boldsymbol{P}}^{\parallel}_i(\boldsymbol{r}) \cdot \hat{\boldsymbol{P}}^{\parallel}_j(\boldsymbol{r}) \\ &- \sum_i \int d\boldsymbol{r} \hat{\boldsymbol{P}}_i(\boldsymbol{r}) \cdot \boldsymbol{E}^{\perp}(\boldsymbol{r}). \end{aligned} \tag{3.4}$$

The explicit form of $\hat{\boldsymbol{P}}_i(\boldsymbol{r})$ is [161–163]

$$\hat{\boldsymbol{P}}_i(\boldsymbol{r}) = \sum_{\alpha} e_{\alpha}(\hat{\boldsymbol{q}}_{\alpha} - \boldsymbol{R}_i) \int_0^1 d\lambda \delta(\boldsymbol{r} - \boldsymbol{R}_i - \lambda(\hat{\boldsymbol{q}}_{\alpha} - \boldsymbol{R}_i)), \tag{3.5}$$

where e_{α} and $\hat{\boldsymbol{q}}_{\alpha}$ are the charge and the position operator of the α-th electron in the molecule i, respectively, and $\boldsymbol{R}_i$ is the center of mass of the molecule. The integration in Eq. (3.5) with respect to λ is introduced to express the polarization in such a compact form, instead of using multipoles explicitly.

I address here the relation between the present optical response formula and the conventional approach based on a multipole expansion method. Eq. (3.5) can be expanded in a Taylor series leading to the dipole, quadrupole, octapole, and higher-order multipole terms. The present formulation is thus a generalization of the conventional optical response theory with the dipole approximation. Applying the Taylor expansion to Eq. (3.5) and integrating the resulting equation with respect to λ, we obtain

$$\begin{aligned}
&\int d\boldsymbol{r}\hat{\boldsymbol{P}}(\boldsymbol{r})\cdot\boldsymbol{E}^{\perp}(\boldsymbol{r}) \\
&\quad= \left(\sum_{\alpha} e_{\alpha}(\hat{\boldsymbol{q}}_{\alpha}-\boldsymbol{R})_i\right)\cdot E_i^{\perp}(\boldsymbol{R}) \\
&\qquad-\left(\frac{1}{2!}\sum_{\alpha} e_{\alpha}(\hat{\boldsymbol{q}}_{\alpha}-\boldsymbol{R})_i(\hat{\boldsymbol{q}}_{\alpha}-\boldsymbol{R})_j\right)\nabla_i E_j^{\perp}(\boldsymbol{R}) \\
&\qquad+\left(\frac{1}{3!}\sum_{\alpha} e_{\alpha}(\hat{\boldsymbol{q}}_{\alpha}-\boldsymbol{R})_i(\hat{\boldsymbol{q}}_{\alpha}-\boldsymbol{R})_j(\hat{\boldsymbol{q}}_{\alpha}-\boldsymbol{R})_k\right) \\
&\qquad\quad\times\nabla_i\nabla_j E_k^{\perp}(\boldsymbol{R}) \\
&\qquad\quad\cdots \\
&\quad\equiv \hat{\mu}_i E_i^{\perp}+\hat{Q}_{ij}\nabla_i E_j^{\perp}+\hat{O}_{ijk}\nabla_i\nabla_j E_k^{\perp}\cdots, \qquad (3.6)
\end{aligned}$$

where $\hat{\mu}_i$, $\hat{Q}_{ij}$, and $\hat{O}_{ijk}$ represent the dipole, quadrupole, and octapole moments of a molecule, respectively, and the indexes denote their (x, y, z) tensorial components. These moments are defined at the molecular center $\boldsymbol{R}$. ∇_i is the gradient operator along the i-th direction and acts on the electric field. Here a contraction of $x_i y_i = \sum_i x_i y_i$ is used. The dipole moment couples with the field itself, the quadrupole with the first derivative of the field, and the octapole with the second derivative of the field, and so forth. If an electric field varies slowly over a whole spatial region, the optical response can be reasonably described by only the first term of this expansion (i.e., the dipole approximation). However, the near-field interaction requires an infinite number of terms in the expansion because of its nonuniform spatial structure. Therefore, I use Eq. (3.5) as is, without performing the Taylor expansion of the polarization.

3.3 A molecule interacting with a near-field

This subsection derives a compact expression of the Hamiltonian for a molecule interacting with a near-field. In contrast to the conventional optical response theory for molecules in which electromagnetic fields are uniform external fields, nano-optics concerns nonuniform electric fields and these fields will be modified by a feedback from an excited molecule. The first problem requires one to go beyond the dipole approximation. The second one requires a self-consistent treatment on light and matter at the nanometer scale. This study focuses on the first problem, and the second one will be studied in the future.

3.3.1 Nonuniform light-matter interaction model

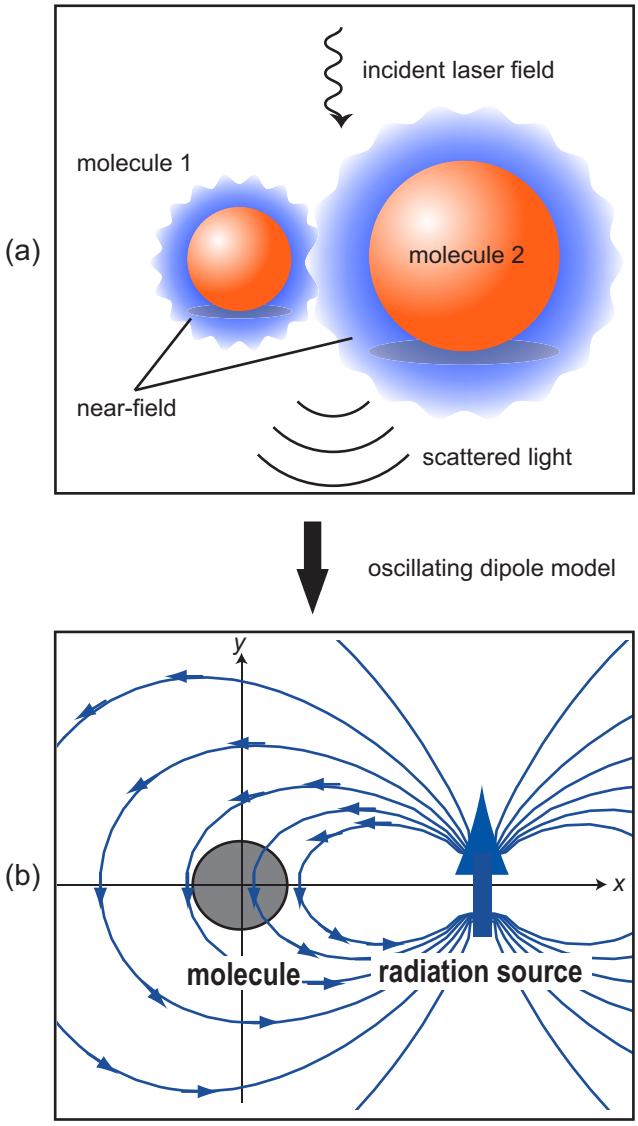

Figure 3.1: (a) Schematic diagram of near-field and scattered light radiation from distant molecules 1 and 2 in the presence of an incident laser field. (b) Nonuniform light-matter interaction model derived from the above molecular system. The molecule 2 is considered to be a radiation source approximated by an oscillating dipole (a blue bold arrow). The near-fields, i.e., nonuniform electric fields, radiated from the oscillating dipole are shown in the blue curves.

To demonstrate the electron dynamics in molecules interacting with a near-field, I first introduce a theoretical model consisting of two molecules irradiated by a laser light. Fig. 3.1(a) schematically shows the model. The multipolar Hamiltonian Eq.

(3.4) is rewritten for such a model system by

$$\hat{H}_{\rm mol} + \frac{1}{\varepsilon_0}\int d\boldsymbol{r}\hat{\boldsymbol{P}}_1^{\parallel}(\boldsymbol{r})\cdot\hat{\boldsymbol{P}}_2^{\parallel}(\boldsymbol{r}) - \int d\boldsymbol{r}\left(\hat{\boldsymbol{P}}_1(\boldsymbol{r})+\hat{\boldsymbol{P}}_2(\boldsymbol{r})\right)\cdot\boldsymbol{E}^{\perp}(\boldsymbol{r}). \tag{3.7}$$

As mentioned in the introduction, the near-field is a non-propagating local field around nanostructures, generated in the presence of laser irradiation. Although the near-field should be given by solving the Maxwell's equations (or by resorting to quantum electrodynamics theory in a narrow sense), it is reasonably approximated by the short-range term of an oscillating dipole radiation [133, 164]. Then, the theoretical model given by Eq. (3.7) can be further simplified as follows. I discuss here optical response of the molecule 1 interacting only with the near-field radiated from the molecule 2, in which the molecule 2 is considered to be an oscillating dipole as shown in Fig. 3.1(b). This approximation means that the material Hamiltonian of the molecule 1 is solved quantum mechanically, whereas the molecule 2 is assumed to be a classical dielectric merely as a radiation source. Furthermore, I neglect the near-field induced around the molecule 1, which might affect the dielectric molecule 2 (i.e., the self-consistent effect). Since I focus on roles of the nonuniform electric field in electronic excitation of a molecule, the self-consistent effect is left for the future investigation. The incident laser field $\boldsymbol{E}_{\rm laser}^{\perp}$ in the third term of Eq. (3.7) is required to induce the polarization associated with the oscillating dipole in the molecule 2. From my preliminary calculations, however, the incident field was found to be less important for the light-matter interaction in the near-field region because the intensity of the induced near-field is larger than that of the incident field. As a result, the electron dynamics in this region is qualitatively unaffected even if the incident laser field is neglected.

Under these conditions, Eq. (3.7) can be reduced to the form of

$$\hat{H}_{\rm mol} - \int d\boldsymbol{r}\hat{\boldsymbol{P}}_1^{\parallel}(\boldsymbol{r})\cdot\tilde{\boldsymbol{E}}_2^{\parallel}(\boldsymbol{r}) - \int d\boldsymbol{r}\left(\hat{\boldsymbol{P}}_1(\boldsymbol{r})+\hat{\boldsymbol{P}}_2(\boldsymbol{r})\right)\cdot\left(\tilde{\boldsymbol{E}}_1^{\perp}(\boldsymbol{r})+\tilde{\boldsymbol{E}}_2^{\perp}(\boldsymbol{r})\right), \tag{3.8}$$

where the longitudinal part of the polarization operator $\hat{\boldsymbol{P}}_2^{\parallel}$ is replaced with the expectation (or c-number) value $-\varepsilon_0\tilde{\boldsymbol{E}}_2^{\parallel}$. $\tilde{\boldsymbol{E}}$ represents the near-field part of $\boldsymbol{E}$. Although the far-field part of $\boldsymbol{E}$ can also be included in this derivation, I only use the near-field part for simplicity. Eq. (3.8) is rewritten in a more compact form of

$$\hat{H}_{\rm mol} - \int d\boldsymbol{r}\hat{\boldsymbol{P}}_1(\boldsymbol{r})\cdot\tilde{\boldsymbol{E}}_2(\boldsymbol{r}) - \int d\boldsymbol{r}\left[\hat{\boldsymbol{P}}_1(\boldsymbol{r})\cdot\tilde{\boldsymbol{E}}_1^{\perp}(\boldsymbol{r})+\hat{\boldsymbol{P}}_2(\boldsymbol{r})\cdot\left(\tilde{\boldsymbol{E}}_1^{\perp}(\boldsymbol{r})+\tilde{\boldsymbol{E}}_2^{\perp}(\boldsymbol{r})\right)\right], \tag{3.9}$$

where I used the relations of $\hat{\boldsymbol{P}}_1^{\parallel}\cdot\tilde{\boldsymbol{E}}_2^{\parallel} = \hat{\boldsymbol{P}}_1\cdot\tilde{\boldsymbol{E}}_2^{\parallel}$ and $\tilde{\boldsymbol{E}}_2^{\parallel}+\tilde{\boldsymbol{E}}_2^{\perp} = \tilde{\boldsymbol{E}}_2$. Since the self-interaction term $\hat{\boldsymbol{P}}_1\cdot\tilde{\boldsymbol{E}}_1^{\perp}$ is not important in this work and $\hat{\boldsymbol{P}}_2(\boldsymbol{r})\cdot(\tilde{\boldsymbol{E}}_1^{\perp}(\boldsymbol{r})+\tilde{\boldsymbol{E}}_2^{\perp}(\boldsymbol{r}))$

does not act on the molecule 1, these terms can be omitted. Finally, the Hamiltonian of a molecule interacting with the near-field becomes

$$\begin{aligned}\hat{H} &\equiv \hat{H}_{\rm mol} + \hat{H}_{\rm int} \\ &= \hat{H}_{\rm mol} - \int d\boldsymbol{r}\hat{\boldsymbol{P}}_1(\boldsymbol{r})\cdot\tilde{\boldsymbol{E}}_2(\boldsymbol{r}),\end{aligned} \tag{3.10}$$

This nonuniform light-matter interaction Hamiltonian is used throughout this study. The present computational model is rather oversimplified. However, it is computationally demanding (might be practically impossible) to fully solved coupled Schrödinger−Maxwell equations, taking account of the properties of the self-consistency and the nonuniformity due to the light-matter interaction at the 1 nm scale. This derivation can also be applied to three or more particle systems, where only the dynamics of the molecule 1 interacting with the near-fields generated by the molecules 2, 3, $\cdots$ is solved quantum mechanically in a similar way as in the two-particle system.

3.3.2 Near-field radiated from an oscillating dipole

Next, I have to model the near-field. The near-field is known to be a localized, non-propagating part of the light generated from a molecule when irradiated by an incident laser field (see Fig.3.1(a)). I describe the near-field in this thesis as the near-part of the electric field generated from an oscillating dipole, the simplest model for a radiation. In Fig. 3.1(b), the electric lines of the dipole radiation are depicted as the blue curves, the directions of which are shown by the arrows on the lines.

The analytical expression of the dipole radiation field $\boldsymbol{E}_{\rm dip}(\boldsymbol{r},t)$ generated by the oscillating dipole is given by [164]

$$\boldsymbol{E}_{\rm dip}(\boldsymbol{r},t) = \frac{k^3}{4\pi\varepsilon_0}\Big(\frac{[3\boldsymbol{n}(\boldsymbol{n}\cdot\boldsymbol{\mu})-\boldsymbol{\mu}]}{(kr)^3} \tag{3.11a}$$

$$- i\frac{[3\boldsymbol{n}(\boldsymbol{n}\cdot\boldsymbol{\mu})-\boldsymbol{\mu}]}{(kr)^2} \tag{3.11b}$$

$$+ \frac{[(\boldsymbol{n}\times\boldsymbol{\mu})\times\boldsymbol{n}]}{(kr)}\Big)e^{-i\omega t+ikr} \tag{3.11c}$$

where k is a wavenumber, ε_0 is the vacuum permittivity, $\boldsymbol{n}$ is the unit vector of $\boldsymbol{r}/r$, $\boldsymbol{\mu}$ is a dipole moment of the source placed at the origin, and ω is a frequency of the oscillation, where $\omega = kc$ with c being the velocity of light. The radiation field is classified into three parts in terms of the radial dependencies, r^{-3}, r^{-2}, and r^{-1}. I set the distance between the target molecule and the radiation source to be several angstroms, which is comparable in size with the molecule. In this region, the dipole radiation field is dominated by the local electric field depending on r^{-3} given by Eq. (3.11a). This local field is referred to as the near-field $\tilde{\boldsymbol{E}}$ used in the nonuniform light-matter interaction in Eq. (3.10). I can then neglect the magnetic interacting terms because the magnetic field from the oscillating dipole, not shown here, has the r^{-2} and r^{-1} dependent terms. This will be discussed in more detail in Appendix B.

3.4 Light-matter interaction in the Kohn-Sham equation

For computational applications of the present formal theory, I will derive the light-matter interaction $H_{\rm int}$ in the Kohn-Sham (KS) DFT form. In the following derivations, I take $e_\alpha = 1$ for simplicity. Although the KS Hamiltonian is obtained by functional derivative of the expectation value of the total energy, it is enough to consider here only the light-matter interaction term of Eq.(3.10). The expectation value of $\hat{H}_{\rm int}$ is expressed by

$$\begin{aligned}
\left\langle \hat{H}_{\rm int} \right\rangle &= \int d\boldsymbol{r}\Psi^*(\boldsymbol{r})\hat{H}_{\rm int}\Psi(\boldsymbol{r}) \\
&= -\int d\boldsymbol{r}d\boldsymbol{r}'\Psi^*(\boldsymbol{r})\hat{\boldsymbol{P}}(\boldsymbol{r}')\Psi(\boldsymbol{r})\cdot\tilde{\boldsymbol{E}}(\boldsymbol{r}') \\
&= -\int d\boldsymbol{r}d\boldsymbol{r}'\Psi^*(\boldsymbol{r})(\boldsymbol{r}-\boldsymbol{R}) \\
&\quad\times\int_0^1 d\lambda\delta(\boldsymbol{r}'-\boldsymbol{R}-\lambda(\boldsymbol{r}-\boldsymbol{R}))\Psi(\boldsymbol{r})\cdot\tilde{\boldsymbol{E}}(\boldsymbol{r}') \\
&= -\int d\boldsymbol{r}\left[\Psi^*(\boldsymbol{r})\Psi(\boldsymbol{r})\right](\boldsymbol{r}-\boldsymbol{R})\int_0^1 d\lambda \\
&\quad\times\int d\boldsymbol{r}'\delta(\boldsymbol{r}'-\boldsymbol{R}-\lambda(\boldsymbol{r}-\boldsymbol{R}))\tilde{\boldsymbol{E}}(\boldsymbol{r}') \\
&\equiv -\int d\boldsymbol{r}\rho(\boldsymbol{r})(\boldsymbol{r}-\boldsymbol{R})\cdot\int_0^1 d\lambda\tilde{\boldsymbol{E}}(\boldsymbol{R}+\lambda(\boldsymbol{r}-\boldsymbol{R})) \\
&\equiv -\int d\boldsymbol{r}\rho(\boldsymbol{r})(\boldsymbol{r}-\boldsymbol{R})\cdot\boldsymbol{E}_{\rm eff}(\boldsymbol{r}) \\
&\equiv \int d\boldsymbol{r}\rho(\boldsymbol{r})V_{\rm eff}(\boldsymbol{r}) \qquad (3.12)
\end{aligned}$$

where Ψ is the ground state wavefunction of the molecule, and the electron density $\rho(\boldsymbol{r})$, the effective electric field $\boldsymbol{E}_{\rm eff}$, and the effective potential $V_{\rm eff}$ are given by

$$\rho(\boldsymbol{r}) \equiv \Psi^*(\boldsymbol{r})\Psi(\boldsymbol{r}), \qquad (3.13)$$

$$\boldsymbol{E}_{\rm eff}(\boldsymbol{r}) \equiv \int_0^1 d\lambda\tilde{\boldsymbol{E}}(\boldsymbol{R}+\lambda(\boldsymbol{r}-\boldsymbol{R})), \qquad (3.14)$$

$$V_{\rm eff}(\boldsymbol{r}) \equiv -(\boldsymbol{r}-\boldsymbol{R})\cdot\boldsymbol{E}_{\rm eff}(\boldsymbol{r}). \qquad (3.15)$$

The λ-integration of $\tilde{\boldsymbol{E}}$ includes all the contributions of the spatial variation of the electric field. As is clearly seen from Eq.(3.12), the nonuniform light-matter interaction is straightforwardly calculated in the conventional KS-DFT approach if the effective potential $V_{\rm eff}$ is added to the external potential term in the KS equation. In the next chapter, the KS-DFT computational approach will be explained to demonstrate the electron dynamics of nanoclusters interacting with a near-field.

Chapter 4

Computational applications and system details

This chapter describes the computational applications of the present formal theory. Numerical computation is based on the time-dependent density functional theory (TDDFT) with the effective potential that is obtained from a near-field modeled by the dipole-radiation field. As a computational system, I adopt a linear-chain molecule NC_6N in the near-field.

4.1 Time-dependent Kohn-Sham approach in real space

The time-dependent Kohn-Sham (TD-KS) approach in real space and time to electron dynamics has so far been explained elsewhere [165–168]. I review the approach with particular emphasis on extending it to the optical response to a nonuniform electric field. A time-dependent N-electron interacting system is solved through a set of electronic wave functions $\psi_j(\boldsymbol{r}, t)$ satisfying the following TD-KS equation

$$i\hbar\frac{\partial}{\partial t}\psi_j(\boldsymbol{r}, t) = \left[-\frac{\hbar^2}{2m}\nabla^2 + V_{\mathrm{KS}}[\rho](\boldsymbol{r}, t)\right]\psi_j(\boldsymbol{r}, t), \tag{4.1}$$

where m is the electron mass and ρ is the electron density given by

$$\rho(\boldsymbol{r}, t) = 2\sum_{j=1}^{N/2}|\psi_j(\boldsymbol{r}, t)|^2. \tag{4.2}$$

The factor of 2 indicates that each KS orbital is fully occupied (i.e., a closed shell system). The KS potential $V_{\mathrm{KS}}[\rho](\boldsymbol{r}, t)$ is a functional of ρ, and it consists of four terms of an ion-electron interaction potential $V_{\mathrm{ion}}(\boldsymbol{r})$, a time-dependent Hartree potential, an exchange-correlation (XC) potential $V_{\mathrm{xc}}[\rho](\boldsymbol{r}, t)$, and an external potential V_{eff} as

follows:

$$V_{\mathrm{KS}}[\rho](\boldsymbol{r},t) = V_{\mathrm{ion}}(\boldsymbol{r}) + \frac{1}{4\pi\varepsilon_0}\int \frac{\rho(\boldsymbol{r'},t)}{|\boldsymbol{r}-\boldsymbol{r'}|}d\boldsymbol{r'} + V_{\mathrm{xc}}[\rho](\boldsymbol{r},t) + V_{\mathrm{eff}}(\boldsymbol{r},t). \tag{4.3}$$

The ion-electron interaction potential $V_{\mathrm{ion}}(\boldsymbol{r})$ is constructed from norm-conserving pseudopotentials of each atomic component of the system considered. Following the Troullier and Martins procedure [169], the pseudopotentials are numerically generated so that the pseudowavefunctions can imitate the all-electron atomic wave functions. The potentials depend on the angular momentum components. In this thesis, I use the Kleinman-Bylander separable form to represent the nonlocal (i.e., angular momentum depending) potential terms [170].

To represent the XC potential, I use the following adiabatic local density approximation (ALDA)

$$V_{\mathrm{xc}}[\rho](\boldsymbol{r},t) \approx V_{\mathrm{xc}}^{\mathrm{LDA}}[\rho](\boldsymbol{r},t) = V_{\mathrm{xc}}^{\mathrm{LDA}}[\rho_0](\boldsymbol{r})\big|_{\rho_0(\boldsymbol{r})=\rho(\boldsymbol{r},\boldsymbol{t})}, \tag{4.4}$$

where $V_{\mathrm{xc}}^{\mathrm{LDA}}[\rho_0](\boldsymbol{r})$ is the ground-state LDA XC potential given by Perdew and Zunger [171]. In ALDA, the XC potential at $\boldsymbol{r}$ and t is approximated by that of the ground-state uniform electron gas having the density $\rho(\boldsymbol{r},\boldsymbol{t})$. Although the ALDA XC potential does not take account of the nonlocality in both $\boldsymbol{r}$ and t and more accurate exchange-correlation functionals have been developed lately, the ALDA has practically provided reasonable results for single-electron excitation processes sufficiently below the lowest ionization threshold of systems [172–174]. Furthermore, it is reasonable to use such a simple functional at this early stage of development prior to performing highly accurate calculations towards material science.

In the present theoretical model of the nonuniform light-matter interaction, the external potential V_{eff} is given by Eqs. (3.14) and (3.15). As mentioned above, $\tilde{\boldsymbol{E}}$ in Eq. (3.14) is approximated as the oscillating dipole radiation Eq. (3.11), the main contribution of which is given by the r^{-3} dependent term of Eq. (3.11a). For convenience of computation, setting the center of mass of a molecule to be at the origin and giving the external electric field in the form of a pulsed field, the effective potential Eq. (3.15) is rewritten by

$$V_{\mathrm{eff}}(\boldsymbol{r},t) = -\boldsymbol{r}\cdot\boldsymbol{E}_{\mathrm{eff}}(\boldsymbol{r})\sin(\omega t)\sin^2\left(\frac{\pi t}{T}\right) \qquad (0<t<T), \tag{4.5}$$

where ω is the frequency of the oscillating dipole, and T determines the pulse duration. The pulse profile is approximated by $\sin^2\left(\frac{\pi t}{T}\right)$ in which a few cycles of the electric fields are included. The field intensity is related to the field strength by $I = \frac{1}{2}\varepsilon_0 cE^2$.

4.2 Molecular system and computational details

A linear chain molecule is one of the better choices to demonstrate the nonuniform light-matter interaction, in particular for such an electric field proportional to r^{-3}.

I choose a dicyanodiacetylene (NC_6N) molecule [175] shown in Figure 4.1(a) as an example of a real molecule. The geometric structure has been optimized by using the TURBOMOLE V5.10 [142, 176] package of quantum chemistry programs, employing the LDA exchange functional developed by Perdew and Wang [177] with the basis set of def-SV(P) [178] from the TURBOMOLE basis set library, which corresponds to the basis set of 6-31G*. The simplest functional LDA was chosen for consistency with the functional used in the TD-KS equation. The vibrational analysis showed no imaginary frequency. The interatomic distances of the molecule are $N_1{-}C_2 = 1.176$ Å, $C_2{-}C_3 = 1.354$ Å, $C_3{-}C_4 = 1.239$ Å, and $C_4{-}C_5 = 1.340$ Å [179].

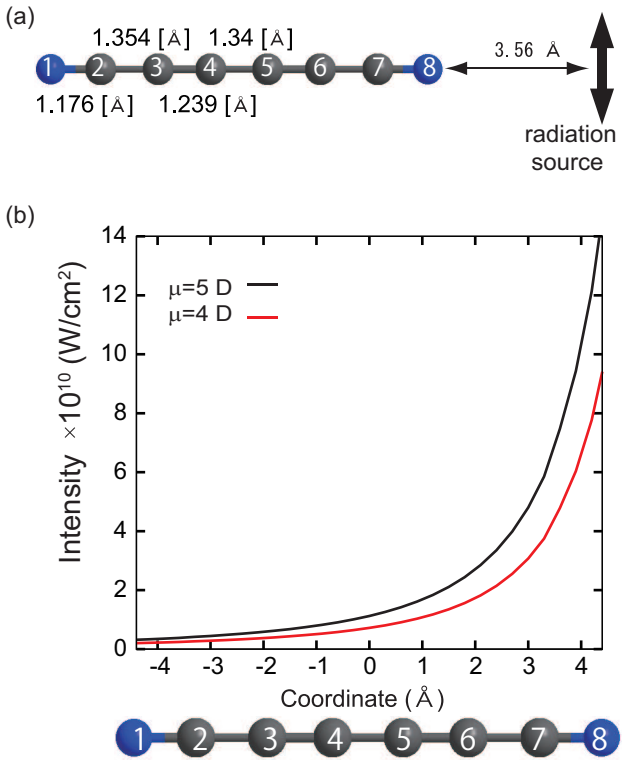

Figure 4.1: (a) Geometrical structure of NC_6N and the position of the radiation source. (b) The effective electric field intensities on the molecular axis. The near-fields are generated by the oscillating dipole with its absolute value of the dipole moment being 4 D (red line) and 5 D (black line), respectively.

The TDKS equation (4.1) for NC_6N is solved numerically by a grid-based method [165, 180] in a three-dimensional Cartesian-coordinate rectangular box, the lengths of which are 30 Å along the molecular (x-) axis and 20 Å along the y- and z-axes, utilizing uniform grids with a mesh spacing of 0.3 Å. The Laplacian operator is evaluated by a nine-point difference formula [181]. The time-propagation of the KS orbitals is carried out with a fourth-order Taylor expansion by using a constant time step of 0.002 fs. The inner shell structures of the carbon and nitrogen atoms are approximated by

effective core pseudopotentials, and then the remaining four electrons ($2s^2 2p^2$) for C and five electrons ($2s^2 2p^3$) for N are explicitly treated. In other words, I have carried out 34-electron dynamics calculations for NC_6N.

The effective potential for the dipole radiation on each grid is computed combining Eqs. (3.11), (3.14), and (3.15), where the main contribution in (3.11) is its near-field part (3.11a). A point dipole $\boldsymbol{\mu}$ is placed at $x = 8.0$ Å (i.e., the value of 3.56 Å is the distance between the rightmost nitrogen atom N(8) and the dipole as shown in Fig. 4.1(a)) so that the nonuniform electronic excitation due to the near-field is clearly demonstrated. The dipole is assumed to be y-polarized, that is $\boldsymbol{\mu} = (0.0,\ \mu,\ 0.0)$ debye (D), where μ is the absolute value of the dipole moment. The dipole fields generated from $\mu = 4.0$ D and 5.0 D are used in this study. The integral of Eq. (3.14) is calculated numerically with a constant step of $\Delta\lambda = 0.0423$ Å. The contribution of the dipole radiation field at its origin to the integration is evaluated by $4\pi\boldsymbol{\mu}/3$ [163]. $\boldsymbol{E}_{\rm dip}$ is also replaced with $4\pi\boldsymbol{\mu}/3$ if $|\boldsymbol{E}_{\rm dip}|$ is larger than $|4\pi\boldsymbol{\mu}/3|$. This is done for a few points very close to the dipole, i.e., $|r| \sim 0.2$ Å. The intensity of the nonuniform electric field varies largely as indicated in Fig. 4.1(b). The effective electric field intensity at the right end of the NC_6N molecule is two orders of magnitude larger than that at the left end (i.e., 10^{11} and 10^9 W/cm^2 at the right and the left ends, respectively). Thus, the molecule is nonuniformly excited by the oscillating dipole field. All the electric fields used in this study have the field frequency ω of 1 eV (the off-resonance condition). The pulse duration ($T = 30$ fs) is short enough to avoid considering the nuclear dynamics.

Chapter 5

Nonuniform electronic excitation induced by the near-field

This chapter discusses mechanisms of the nonuniform excitations induced by the near-field. To this end, the computational approach to the electron dynamics under the nonuniform light-matter interaction, developed in the last two chapters, is applied to a NC_6N molecular system as an example. The excitations are analyzed by visualizing the electron densities and by calculating the induced dipole and quadrupole moments of the NC_6N molecule in the time- and frequency-domains. The nonuniform excitation processes are also analyzed on the basis of the perturbation theory. Finally, a control of high-harmonics is demonstrated in the nonuniform excitation by using two-radiation sources.

5.1 Nonuniform electronic excitation

Let me first demonstrate the electron density motions in the uniform and the nonuniform electric fields. Figure 5.1 shows four snapshots of differences of the electron densities at t = 6, 12, 18, 24, and 30 fs from the initial ($t = 0$) electron density. The red and the blue colors indicate an increase and a decrease in the electron density, respectively. Each column of the snapshots illustrates the different time evolution of the electron density depending on the ways of electronic excitation. Four schematic illustrations at the top of the figure display how the light-matter interaction works. The uniform oscillating-electric-field with its intensity of 10^{12} W/cm^2 is applied to the molecule along the (a) x- or (b) y-axis, whereas the nonuniform fields radiated from the oscillating dipoles (the black bold arrows) with their dipole moments being (c) 4 D and (d) 5 D are applied to the molecule.

The electron densities in Figs. 5.1(a) and (b) oscillate uniformly and regularly along the applied field directions, keeping the molecular symmetry. However, as shown

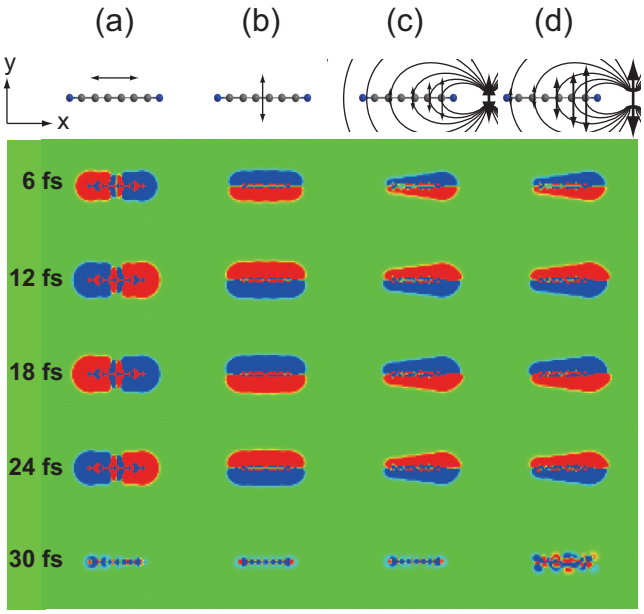

Figure 5.1: Snapshots of difference of the electron density at t=6, 12, 18, 24, and 30 fs from the initial (t = 0 fs) static electron density. The uniform fields ((a), (b)) and the nonuniform (oscillating dipole) fields with their dipole moments being (c) 4 D and (d) 5 D are applied to the molecule. The red and blue colors represent an increase and a decrease in the electron density, respectively. Four schematic illustrations at the top of each snapshot display the ways of electronic excitation.

in Figs. 5.1(c) and (d), the nonuniform electric field apparently induces the symmetry-breaking time-evolution of the electron density. Such inhomogeneous electron dynamics clearly reflects the spatial distribution of the dipole field. Since the oscillating dipole is y-polarized, the generated electric field on the x-axis is also y-polarized, but its intensity sharply falls as r increases (i.e., $\propto r^{-3}$), where r is the distance from the oscillating dipole. Furthermore, only the x-component of the dipole field E_x is antisymmetric with respect to the x-axis (i.e., $E_x(x, y, z) = -E_x(x, -y, z)$), whereas E_y and E_z are symmetric. For these reasons, the time-evolved densities in Figs. 5.1(c) and (d) regularly oscillate to some extent along the y-axis, whereas those are distorted along the x-axis. The electron density distributions at 12 and 18 fs, for example, represent the antisymmetric motion along the x-axis. Specifically, the upper and lower half parts of the densities with respect to the x-axis move toward the opposite directions. These irregular motions are really due to the electronic excitation by the symmetry-breaking, nonuniform electric field. The electron density distribution at 30 fs in Fig. 5.1(d) looks rather different from the others. The electron-density-differences in Figs. 5.1(a)-(c) almost disappear at the end of the pulse of the external electric fields because the applied laser frequency considered is not in tune with any resonance frequencies. In contrast, the electron density distribution in Fig. 5.1(d), under the

condition of the stronger nonuniform electric field, still persists even after the end of the external field.

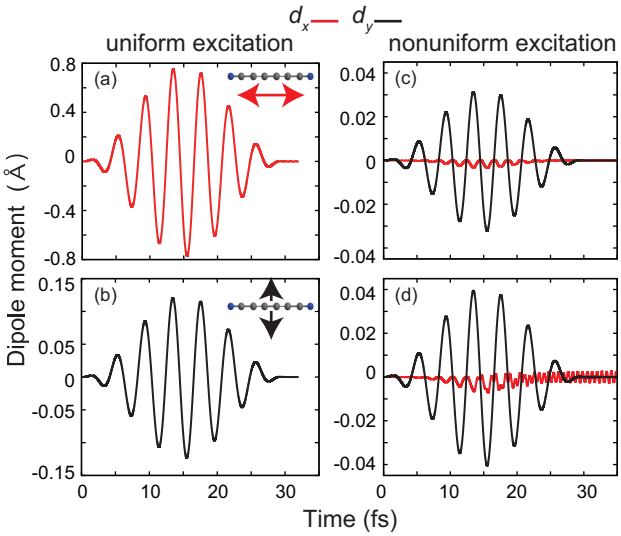

Figure 5.2: Induced dipole moments along the x- and y-axes, d_i $(i = x, y)$. The dipole moments, respectively, correspond to the time-evolutions of the density in Figs. 5.1(a)-(d). Insets in (a) and (b) are schemes of the applied field direction.

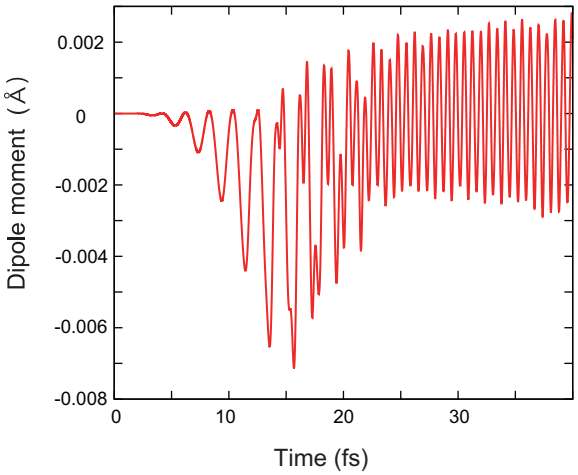

Figure 5.3: Magnification of d_x in Fig. 5.2(d).

Figures 5.2(a)-(d) show the induced dipole moments along the x- and y-axes, d_i $(i = x, y)$, corresponding to the time evolutions of the electron densities in Figs. 3(a)-(d), respectively. The red and the black curves represent d_x and d_y. The insets in Figs. 5.2(a) and (b) schematically draw the applied field directions. Similar overall time-profiles have been observed in d_x (Fig. 5.2(a)) and d_y (Fig. 5.2(b)) induced by the uniform field and in d_y induced by the nonuniform field. In sharp contrast,

nonuniformly induced d_xs do not follow the time-profile of the applied field. To see this more clearly, I pick up d_x in Fig. 5.2(d) and plot it in Fig. 5.3. In the early times until about 20 fs, d_x takes negative values owing to the sharp gradient in the field intensity. The oscillation frequency becomes much faster than that of the applied field after $\sim$ 20 fs. Such an irregular oscillation of d_x is a consequence of the antisymmetric E_x of the dipole field that acts strongly in the right part of NC_6N. Thus, the irregular time-evolutions of the density along the x-axis in Figs. 5.1(c) and (d) were induced by the nonuniform, antisymmetric dipole radiation field. I have further confirmed that such an irregular motion cannot be induced even if I use either an electric field having a similar sharp gradient in the field intensity or an antisymmetric electric field.

I next calculate the emission spectra for each electron dynamics to analyze the uniform and nonuniform electronic excitations in an energy domain. Since the emission spectrum is associated with the dipole acceleration [182, 183], I take the second derivative of the induced dipole moments and then perform a Fourier transform. Fig. 5.4 shows the power spectra of the dipole acceleration $|\ddot{d}_i(\omega)|^2$ $(i = x, y)$ in the unit of Å^2 fs^{-2} as a function of energy. I refer to the power spectra of the dipole acceleration as harmonic-generation (HG) spectra. The HG spectra in Figs. 5.4(a)-(d) correspond to the induced dipole moments in Figs. 5.2(a)-(d), respectively. The red and the black curves represent $|\ddot{d}_x(\omega)|^2$ and $|\ddot{d}_y(\omega)|^2$. Comparing Figs. 5.4(a) and (b), the harmonics along the x-axis ($\ddot{d}_x$) seem relatively easier to generate than that along the y-axis ($\ddot{d}_y$). A comparatively large peak appears at around 6 eV in Fig.5.4(a). Since the NC_6N molecule has a dipole resonance frequency at 5.75 eV, this large peak is related to the resonance state. Despite the inversion symmetry of NC_6N, the nonuniform electric field, in contrast to the uniform one, causes the even harmonics in addition to the odd harmonics as shown in Figs. 5.4 (c) and (d). Interestingly, the even and odd harmonics are respectively due to the induced dipole moments along the x- and y-axes. The even harmonics, therefore, have proved to be generated by the nonuniform electric field breaking the symmetry along the x-axis. Furthermore, in comparison with the HG spectra by the uniform electric field, relatively higher harmonics are clearly seen in the HG spectra by the nonuniform electric field. In addition, their peak intensities do not decay linearly against the order of the harmonics.

Before ending this section, I demonstrate that the nonuniform electronic excitation also induces the quadrupole moment, which is never induced by the uniform electric field, as one of the phenomena beyond the dipole approximation. The xy component of the quadrupole moment (Q_{xy}) for the time-evolution of Fig. 5.1(d) and its HG power spectrum are shown in Figs. 5.5(a) and (b), respectively. The quadrupole moments both in the time and the energy domains provide the structural patterns quite similar to those of the dipole ones. To verify that Q_{xy} is non-negligible in the nonuniform excitation, I consider the charge distribution that causes dipole and quadrupole moments. The calculated value of the quadrupole moment in the unit of Å^2 is about an order of magnitude larger than that of the dipole moment in the unit of Å. The dipole moment of two charges q and $-q$ with the intercharge distance

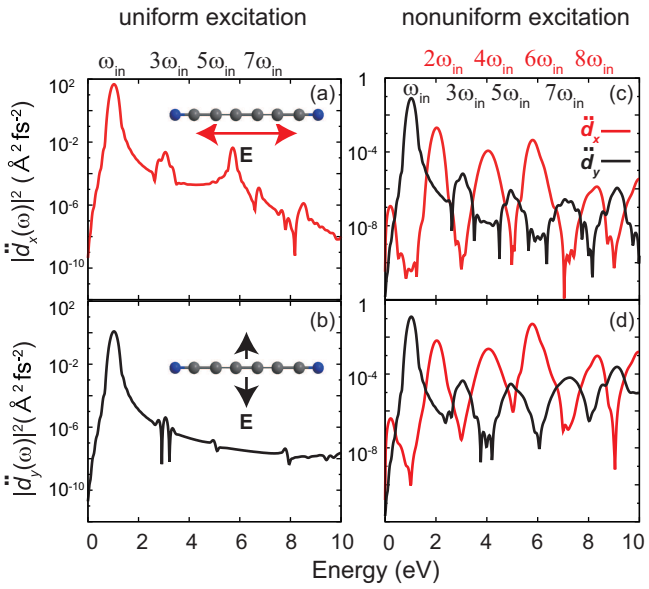

Figure 5.4: Power spectra of the dipole acceleration. The ways of electronic excitation correspond to those in Figs. 5.1(a)-(d) and also in Figs. 5.2(a)-(d), respectively.

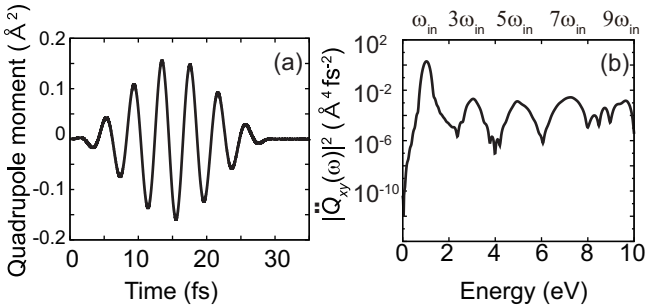

Figure 5.5: (a) xy-component of the induced quadrupole moment as a result of the nonuniform excitation with $\mu = 5$ D and (b) its power spectrum.

a is qa Å, whereas the quadrupole moment of two positive q' and two negative $-q'$ charges disposed at the corners of a square with its side being a is $q'a^2$ Å^2. Then, $|Q_{xy}| \sim 10|d_y|$ (see Figs. 5.2(d) and 5.5(a)) and a is ~ 10 Å for NC_6N. Thus, we have $q \sim q'$ because $q'a^2 \sim 10 \times qa \rightarrow q'a \sim 10 \times q \rightarrow q' \sim q$. This indicates that the dipole-like and quadrupole-like charge distributions have been induced in almost the same amount as a consequence of the nonuniform light-matter interaction.

5.2 Even and Odd Harmonics

Let me next carry out a perturbation analysis of the HG power spectra generated through the nonuniform light-matter interaction. As shown in Figs. 5.4(c) and 5.4(d),

the even harmonics appear despite the inversion symmetry of NC_6N. The even and odd harmonics are due to the induced dipole moments d_x and d_y, respectively. This even and odd alteration is easily understood in terms of the symmetries of the molecular wave functions and the external field.

Table 5.1: Matrix elements of the second-order dipole moments along the x- and y-axes in the power of $V_{\rm eff}$. e and o denote even and odd symmetries, respectively. The symmetries of the ground state and $V_{\rm eff}$ are indicated by bold characters.

$d_x^{(2)}$		$\langle 0\|x\|i\rangle$	$\langle i\|V_{\rm eff}\|j\rangle$	$\langle j\|V_{\rm eff}\|0\rangle$	
	$\int dx$	$\langle \boldsymbol{e}\|\boldsymbol{o}\|o\rangle$	$\langle o\|\boldsymbol{eo}\|eo\rangle$	$\langle eo\|\boldsymbol{eo}\|\boldsymbol{e}\rangle$	$\neq 0$
	$\int dy$	$\langle \boldsymbol{e}\|\ \|e\rangle$	$\langle e\|\boldsymbol{o}\|o\rangle$	$\langle o\|\boldsymbol{o}\|\boldsymbol{e}\rangle$	$\neq 0$
	$\int dz$	$\langle \boldsymbol{e}\|\ \|e\rangle$	$\langle e\|\boldsymbol{e}\|e\rangle$	$\langle e\|\boldsymbol{e}\|\boldsymbol{e}\rangle$	$\neq 0$
$d_y^{(2)}$		$\langle 0\|y\|i\rangle$	$\langle i\|V_{\rm eff}\|j\rangle$	$\langle j\|V_{\rm eff}\|0\rangle$	
	$\int dx$	$\langle \boldsymbol{e}\|\ \|e\rangle$	$\langle e\|\boldsymbol{eo}\|eo\rangle$	$\langle eo\|\boldsymbol{eo}\|\boldsymbol{e}\rangle$	$\neq 0$
	$\int dy$	$\langle \boldsymbol{e}\|\boldsymbol{o}\|o\rangle$	$\langle o\|\boldsymbol{o}\|e\rangle$	$\langle e\|\boldsymbol{o}\|\boldsymbol{e}\rangle$	$= 0$
	$\int dz$	$\langle \boldsymbol{e}\|\ \|e\rangle$	$\langle e\|\boldsymbol{e}\|e\rangle$	$\langle e\|\boldsymbol{e}\|\boldsymbol{e}\rangle$	$\neq 0$

Table 5.2: Same as Table 5.1 but for the third-order dipole moments. As in the case of Table 5.1, $\int dxdz$ is always nonzero, and thus only $\int dy$ is summarized here.

$d_x^{(3)}$		$\langle 0\|x\|i\rangle$	$\langle i\|V_{\rm eff}\|j\rangle$	$\langle j\|V_{\rm eff}\|k\rangle$	$\langle k\|V_{\rm eff}\|0\rangle$	
	$\int dy$	$\langle \boldsymbol{e}\|\ \|e\rangle$	$\langle e\|\boldsymbol{o}\|o\rangle$	$\langle o\|\boldsymbol{o}\|e\rangle$	$\langle e\|\boldsymbol{o}\|\boldsymbol{e}\rangle$	$= 0$
$d_y^{(3)}$		$\langle 0\|y\|i\rangle$	$\langle i\|V_{\rm eff}\|j\rangle$	$\langle j\|V_{\rm eff}\|k\rangle$	$\langle k\|V_{\rm eff}\|0\rangle$	
	$\int dy$	$\langle \boldsymbol{e}\|\boldsymbol{o}\|o\rangle$	$\langle o\|\boldsymbol{o}\|e\rangle$	$\langle e\|\boldsymbol{o}\|e\rangle$	$\langle o\|\boldsymbol{o}\|\boldsymbol{e}\rangle$	$\neq 0$

According to the time-dependent perturbation theory [184, 185], n-th dipole moment $d_\alpha^{(n)}$ ($n = 1, 2, \cdots$ and $\alpha = x, y, z$) in powers of the perturbation $V_{\rm eff}$ can be evaluated by the following matrix elements,

$$\langle 0\,|\alpha|\,i\rangle \underbrace{\langle i\,|V_{\rm eff}|\,j\rangle\,\langle j\,|V_{\rm eff}|\,k\rangle \cdots \langle l\,|V_{\rm eff}|\,0\rangle}_{n \text{ brackets}}, \tag{5.1}$$

where $|0\rangle$ and $|i\rangle$ are the ground and the excited eigen states of the nonperturbative Hamiltonian of the molecule, respectively. As typical examples, $d_x^{(2)}$, $d_y^{(2)}$, $d_x^{(3)}$, and $d_y^{(3)}$ are considered. Table 5.1 summarizes the evaluation of the matrix elements of $d_x^{(2)}$ and $d_y^{(2)}$. The symmetries of the eigen states and the applied field are labeled as "e" for the even symmetry and "o" for the odd one. Since NC_6N has mirror symmetries in every direction, the eigen state $\{|i\rangle\}$ is either even or odd with respect to x-, y-, or z-axis, namely, $\psi(x, y, z) = \pm\psi(-x, y, z)$, $\psi(x, y, z) = \pm\psi(x, -y, z)$, or

$\psi(x,y,z) = \pm\psi(x,y,-z)$. The effective potential $V_{\rm eff}$ given by Eq.(3.15) is neither an even nor an odd function of x, an odd function of y, and an even function of z, i.e., $V_{\rm eff}(x,y,z) \neq V_{\rm eff}(-x,y,z)$, $V_{\rm eff}(x,y,z) = -V_{\rm eff}(x,-y,z)$, and $V_{\rm eff}(x,y,z) = V_{\rm eff}(x,y,-z)$. Thus, the brackets can be estimated by decomposing them into the integrations with respect to the x-, y-, and z-coordinates. $\int d\alpha$ ($\alpha = x,y,z$) in Table 5.1 denotes each component of the integrations. The symmetries of the ground state $|0\rangle$, the operators (x and y), and the potential $V_{\rm eff}$ are specified in bold characters. The symmetries of $|i\rangle$ and $|j\rangle$ are then specified so that the matrix elements have nonzero values. As a result, $d_x^{(2)}$ becomes nonzero, but $d_y^{(2)}$ must be zero because the integral of $\langle j|V_{\rm eff}|0\rangle$ with respect to the y-coordinate vanishes. The same analysis can be applied to $d_\alpha^{(3)}$ (see, Table 5.2). Then, $d_x^{(3)}$ must be zero but $d_y^{(3)}$ becomes nonzero. The above analysis clearly explains the even-odd alteration appears in the HG power spectra obtained by the nonuniform excitation.

5.3 Control of harmonic generation

Finally, it is demonstrated that the harmonics induced by the near-field can be controlled. Fig. 5.6 shows the HG power spectra obtained when both ends of the NC_6N molecule are excited by the near-fields radiated from two oscillating dipoles with different phases by $\pi/2$. The inset illustrates the schematic diagram of the near-field excitation by two radiation sources. It is clearly seen from the figure that harmonics selectively appear every $4\omega_{\rm in}$ starting from the second harmonics ($2\omega_{\rm in}$). The forth and eighth harmonics ($4\omega_{\rm in}$ and $8\omega_{\rm in}$) completely disappear as a result of the interference between the two near-fields having different phases. I expect that this idea of the near-field excitation with different phases can control intensities and orders of HG spectra.

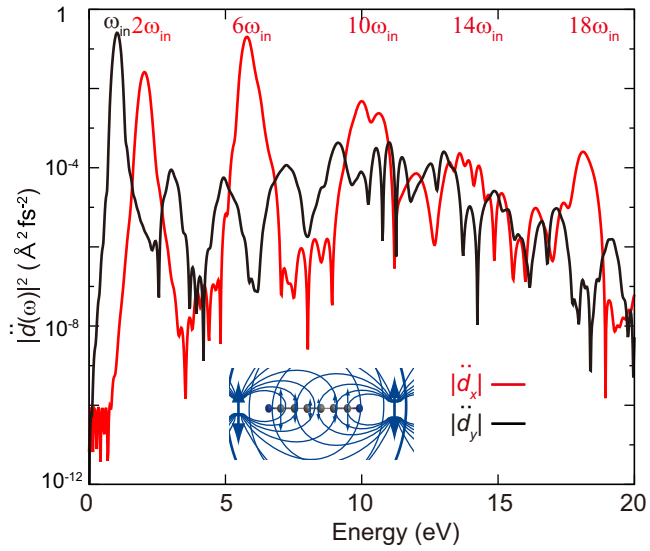

Figure 5.6: Power spectra of the dipole acceleration along the x- and y-axes. Two oscillating dipole fields with different phases disposed at both ends of the molecule are applied.

Chapter 6

Conclusion

This thesis has presented theoretical studies of the geometric, electronic, and optical properties of one-nanometer sized materials. I have revealed the geometric and electronic properties of gold-thiolate nanocluster compounds and developed optical response theory in an effort to understand nonuniform light-matter interaction between near-filed and nanometer-sized cluster compounds.

The geometric and electronic structures of a gold-methanethiolate $[Au_{25}(SCH_3)_{18}]^+$ have been investigated by carrying out the density functional theory (DFT) calculations. The obtained optimized structure consists of a planar Au_7 core cluster and Au-S complexes, where the Au_7 plane is enclosed by a $Au_{12}(SCH_3)_{12}$ ring and sandwiched by two $Au_3(SCH_3)_3$ ring clusters. This sharply contrasted geometry to a generally accepted geometrical motif of gold-thiolate clusters that a spherical gold cluster is superficially ligated by thiolate molecules provides a large HOMO-LUMO gap, and its X-ray diffraction and photoabsorption spectra successfully reproduce the experimental results. On another gold cluster compound $[Au_{25}(PH_3)_{10}(SCH_3)_5Cl_2]^{2+}$, which consists of two icosahedral Au_{13} clusters bridged by methanethiolates sharing a vertex gold atom and terminated by chlorine atoms, the DFT calculations have provided very close structure to the experimentally obtained gold cluster $[Au_{25}(PPh_3)_{10}(SC_2H_5)_5Cl_2]^{2+}$. A vertex-sharing triicosahedral gold cluster $[Au_{37}(PH_3)_{10}(SCH_3)_{10}Cl_2]^+$ has also been achieved by bridging the core Au_{13} units with the methanethiolates. A comparison between the absorption spectra of the bi- and triicosahedral clusters shows that the new electronic levels due to each oligomeric structure appear sequentially, whereas other electronic properties remain almost unchanged compared to the individual icosahedral Au_{13} cluster. These theoretical studies have elucidated the fundamental properties of the promising building blocks such as geometric structures and stability of real cluster compounds in terms of the detailed electronic structures.

To study dynamical near-field interactions at the 1 nm scale, I have developed a generalized theoretical description of optical response in an effort to understand a nonuniform light-matter interaction between a near-field and a 1-nm-sized cluster

compound. The light-matter interaction based on the multipolar Hamiltonian was described in terms of a space integral of the inner product of the total polarization of a molecule and an external electric field. Noteworthy is the fact that the polarization in the integral can be treated entirely without invoking any approximation such as the dipole approximation. Therefore, the present light-matter interaction theory allows us to understand the inhomogeneous electron dynamics associated with local electronic structures of a cluster compound at the 1 nm scale, although the wavelength of an incident laser pulse is much longer than the size of the molecule. For a computational application, I have studied the near-field-induced electron dynamics of NC_6N by using the TD-KS approach incorporated with the present nonuniform interaction theory. The electron dynamics induced by the nonuniform light-matter interaction has been completely different from that by the conventional uniform interaction under the dipole approximation. Specifically, in the nonuniform electronic excitation high harmonics have been generated more easily and much more interestingly the even harmonics have been also generated in addition to the odd ones despite the inversion symmetry of NC_6N. Perturbation theory has clearly explained that the even harmonics were generated owing to the symmetry-breaking (nonuniform) electric field along the x-axis radiated from the oscillating dipole. It has also been found that the nonuniform fields with different phases control harmonic generation though their interference effect. It is expected that the nonuniform electronic excitation can induce unprecedented electron dynamics giving information about local electronic structures, electronic transitions beyond the dipole approximation, and high-order nonlinear optical phenomena. Furthermore, the present nonuniform light-matter interaction/TD-KS approach incorporated with the Maxwell's equation will enable us to elucidate electron and electromagnetic field dynamics in nanostructures.

Appendices

Appendix A

Quantum electrodynamics

The multipolar Hamiltonian (3.1) is derived from the minimal coupling Hamiltonian by the canonical transformation. Before the transformation, the longitudinal and transverse vector fields are explained first. The minimal coupling Hamiltonian is expressed using the polarization and then transformed into the multipolar Hamiltonian. Finally, the semiclassical equation of motion is derived by considering the Heisenberg equation of motion and treating the electromagnetic field classically.

A.1 Longitudinal and Transverse vector fields

The Coulomb gauges is defined as the divergent of the vector potential $\boldsymbol{A}$ is zero, i.e. $\boldsymbol{\nabla} \cdot \boldsymbol{A} = 0$. An intermolecular interaction then can be decomposed into a static instantaneous Coulomb interaction and a dynamical retarded interaction. The former and the latter are described with a longitudinal and a transverse vector fields. The longitudinal and transverse vectors are, in other words, the curl-free and divergence-free. The geometrical explanation of these vectors will be provided.

By definition, longitudinal and transverse vector fields $\boldsymbol{A}^{\parallel}$ and $\boldsymbol{A}^{\perp}$ satisfy the next relations:

$$\boldsymbol{\nabla} \times \boldsymbol{A}^{\parallel} = 0, \tag{A.1}$$

$$\boldsymbol{\nabla} \cdot \boldsymbol{A}^{\perp} = 0. \tag{A.2}$$

Their geometrical meanings can be clearly seen in reciprocal space. Let $\boldsymbol{\mathcal{A}}$ be the Fourier spatial transform of a vector $\boldsymbol{A}$. Then $\boldsymbol{A}$ and $\boldsymbol{\mathcal{A}}$ are related through the following equations:

$$\boldsymbol{\mathcal{A}}(\boldsymbol{k}) = \frac{1}{(2\pi)^{3/2}} \int d\boldsymbol{r} \boldsymbol{A}(\boldsymbol{r}) e^{-i\boldsymbol{k}\cdot\boldsymbol{r}}, \tag{A.3}$$

$$\boldsymbol{A}(\boldsymbol{r}) = \frac{1}{(2\pi)^{3/2}} \int d\boldsymbol{k} \boldsymbol{\mathcal{A}}(\boldsymbol{k}) e^{i\boldsymbol{k}\cdot\boldsymbol{r}}. \tag{A.4}$$

Defining $\boldsymbol{\mathcal{A}}^{\parallel}$ and $\boldsymbol{\mathcal{A}}^{\perp}$ as the Fourier transform of $\boldsymbol{A}^{\parallel}$ and $\boldsymbol{A}^{\perp}$, eqs. A.1 and A.2 can be rewritten as

$$\boldsymbol{\nabla} \times \boldsymbol{A}^{\parallel} = \frac{1}{(2\pi)^{3/2}} \int d\boldsymbol{r}(-i\boldsymbol{k}) \times \boldsymbol{\mathcal{A}}^{\parallel} e^{-i\boldsymbol{k}\cdot\boldsymbol{r}} = 0, \tag{A.5}$$

$$\boldsymbol{\nabla} \cdot \boldsymbol{A}^{\perp} = \frac{1}{(2\pi)^{3/2}} \int d\boldsymbol{r}(-i\boldsymbol{k}) \cdot \boldsymbol{\mathcal{A}}^{\perp} e^{-i\boldsymbol{k}\cdot\boldsymbol{r}} = 0. \tag{A.6}$$

These results mean that $\boldsymbol{\mathcal{A}}^{\parallel}(\boldsymbol{k})$ is parallel to $\boldsymbol{k}$ and $\boldsymbol{\mathcal{A}}^{\perp}(\boldsymbol{k})$ is perpendicular to $\boldsymbol{k}$. Let $\hat{\boldsymbol{k}}$ be the unit vector parallel to $\boldsymbol{k}$, these vectors can be written as

$$\boldsymbol{\mathcal{A}}^{\parallel} \equiv (\boldsymbol{\mathcal{A}} \cdot \hat{\boldsymbol{k}})\hat{\boldsymbol{k}} \tag{A.7}$$

$$\boldsymbol{\mathcal{A}}^{\perp} \equiv \boldsymbol{\mathcal{A}} - \boldsymbol{\mathcal{A}}^{\parallel} \tag{A.8}$$

and therefore we can decompose $\boldsymbol{\mathcal{A}}$ as

$$\boldsymbol{\mathcal{A}} = \boldsymbol{\mathcal{A}}^{\parallel} + \boldsymbol{\mathcal{A}}^{\perp}, \tag{A.9}$$

with

$$\boldsymbol{\mathcal{A}}^{\parallel} \cdot \boldsymbol{\mathcal{A}}^{\perp} = 0. \tag{A.10}$$

Recalling that the inner product of two vectors $\boldsymbol{A}$ and $\boldsymbol{B}$ is irrelevant to the basis, we have

$$\boldsymbol{A}^{\parallel} \cdot \boldsymbol{A}^{\perp} = 0 \tag{A.11}$$

and thus

$$\boldsymbol{A} = \boldsymbol{A}^{\parallel} + \boldsymbol{A}^{\perp}. \tag{A.12}$$

Rewriting A.7 and A.8 as

$$\mathcal{A}_i^{\parallel} = \hat{k}_i \hat{k}_j \mathcal{A}_j \tag{A.13}$$

$$\mathcal{A}_i^{\perp} = (\delta_{ij} - \hat{k}_i \hat{k}_j)\mathcal{A}_j \tag{A.14}$$

where the relation $A_i B_i = \sum_i A_i B_i$ is used. $A_i^{\parallel}$ and $A_i^{\perp}$ can be related to A_j by performing the Fourier spatial transform twice as

$$A_i^{\parallel}(\boldsymbol{r}) = \frac{1}{(2\pi)^{3/2}} \int d\boldsymbol{k} \hat{k}_i \hat{k}_j \mathcal{A}_j(\boldsymbol{k}) e^{i\boldsymbol{k}\cdot\boldsymbol{r}} \tag{A.15}$$

$$= \frac{1}{(2\pi)^3} \iint d\boldsymbol{k} d\boldsymbol{r}' \hat{k}_i \hat{k}_j A_j(\boldsymbol{r}') e^{i\boldsymbol{k}\cdot(\boldsymbol{r}-\boldsymbol{r}')} \tag{A.16}$$

$$A_i^{\perp}(\boldsymbol{r}) = \frac{1}{(2\pi)^{3/2}} \int d\boldsymbol{k} (\delta_{ij} - \hat{k}_i \hat{k}_j) \mathcal{A}_j(\boldsymbol{k}) e^{i\boldsymbol{k}\cdot\boldsymbol{r}} \tag{A.17}$$

$$= \frac{1}{(2\pi)^3} \iint d\boldsymbol{k} d\boldsymbol{r}' (\delta_{ij} - \hat{k}_i \hat{k}_j) A_j(\boldsymbol{r}') e^{i\boldsymbol{k}\cdot(\boldsymbol{r}-\boldsymbol{r}')}. \tag{A.18}$$

Here, the relations can be written in a more compact form if the δ-dyadics are defined as follows:

$$\delta_{ij}^{\parallel}(\boldsymbol{r}) \equiv \frac{1}{(2\pi)^3}\int \hat{k}_i\hat{k}_j e^{i\boldsymbol{k}\cdot\boldsymbol{r}}d\boldsymbol{k} \tag{A.19}$$

$$\delta_{ij}^{\perp}(\boldsymbol{r}) \equiv \frac{1}{(2\pi)^3}\int (\delta_{ij}-\hat{k}_i\hat{k}_j) e^{i\boldsymbol{k}\cdot\boldsymbol{r}}d\boldsymbol{k} \tag{A.20}$$

then with them,

$$A_i^{\parallel}(\boldsymbol{r}) = \int d\boldsymbol{r}' A_j(\boldsymbol{r}')\delta_{ij}^{\parallel}(\boldsymbol{r}-\boldsymbol{r}') \tag{A.21}$$

$$A_i^{\perp}(\boldsymbol{r}) = \int d\boldsymbol{r}' A_j(\boldsymbol{r}')\delta_{ij}^{\perp}(\boldsymbol{r}-\boldsymbol{r}'). \tag{A.22}$$

In short, the longitudinal and the transverse component vectors of a vector field are curl-free and divergence-free, respectively, in a real space. In reciprocal space, the longitudinal and the transverse vectors are the vectors parallel and perpendicular to its wavenumber vector $\boldsymbol{k}$, respectively. In the Coulomb gauge, the vector potential is taken to be divergence-free. From the above discussion, then the vector potential is a transverse vector field

$$\boldsymbol{\nabla}\cdot\boldsymbol{A} = 0 \quad \rightarrow \quad \boldsymbol{A} = \boldsymbol{A}^{\perp} \tag{A.23}$$

A.2 Minimal coupling Hamiltonian in the Coulomb gauge

The minimal coupling Hamiltonian of a system of charged particles interacting with an electromagnetic field in the Coulomb gauge is given by

$$H_{\min} = \sum_{\alpha}\frac{\hbar^2}{2m_\alpha}\left(\boldsymbol{p}_\alpha - e_\alpha\boldsymbol{A}(\boldsymbol{q}_\alpha)\right)^2 + \frac{1}{8\pi\varepsilon_0}\sum_{\alpha\neq\beta}\frac{e_\alpha e_\beta}{|\boldsymbol{q}_\alpha-\boldsymbol{q}_\beta|} + H_{\mathrm{rad}} \tag{A.24}$$

where m_α, e_α, and $\boldsymbol{q}_\alpha$ are the mass, charge, and coordinate of a particle α, respectively, and

$$H_{\mathrm{rad}} = \frac{1}{2}\int d\boldsymbol{r}\left(\frac{\boldsymbol{\Pi}^{\perp 2}}{\varepsilon_0} + c^2\varepsilon_0(\boldsymbol{\nabla}\times\boldsymbol{A})^2\right) \tag{A.25}$$

where the canonical momenta of the field is given by $\boldsymbol{\Pi} = \varepsilon_0\dot{\boldsymbol{A}}(\boldsymbol{r}) = -\varepsilon_0\boldsymbol{E}^{\perp}$ with $\boldsymbol{E}$ being the electric field. Here, H_{rad} is purely transverse, because $\boldsymbol{A}$ is always transverse in the Coulomb gauge.

For a system which consists of molecules, the charged particles can be assigned into each molecule m, then the Hamiltonian becomes

$$\begin{aligned} H_{\min} &= \sum_m \left\{ \sum_{i\in m} \frac{\boldsymbol{p}_i^2}{2m_i} + V_m \right\} + H_{\rm rad} \\ &\qquad + \sum_m \left\{ \sum_{i\in m} \left(-\frac{e_i \boldsymbol{p}_i \cdot \boldsymbol{A}(\boldsymbol{q}_i)}{m_i} + \frac{e_i^2 \boldsymbol{A}^2(\boldsymbol{q}_i)}{2m_i} \right) \right\} + V_{\rm inter} \qquad \text{(A.26)} \\ &\equiv \sum_m H_{\rm mol}(m) + H_{\rm rad} + \sum_m \left\{ H_{\rm int}^{(1)}(m) + H_{\rm int}^{(2)}(m) \right\} + V_{\rm inter} \qquad \text{(A.27)} \\ &\equiv H_{\rm mol} + H_{\rm rad} + H_{\rm int} \qquad \text{(A.28)} \end{aligned}$$

where

$$H_{\rm mol}(m) \equiv \sum_{i\in m} \frac{\boldsymbol{p}_i^2}{2m_i} + V_m, \qquad \text{(A.29)}$$

$$V_m \equiv \frac{1}{8\pi\varepsilon_0} \sum_{i\neq j\in m} \frac{e_i e_j}{|\boldsymbol{q}_i - \boldsymbol{q}_j|}, \qquad \text{(A.30)}$$

$$H_{\rm int}^{(1)}(m) \equiv \sum_{i\in m} \frac{e_i}{m_i} \boldsymbol{p}_i \cdot \boldsymbol{A}(\boldsymbol{q}_i) \qquad \text{(A.31)}$$

$$H_{\rm int}^{(2)}(m) \equiv \sum_{i\in m} \frac{e_i^2}{2m_i} \boldsymbol{A}^2(\boldsymbol{q}_i) \qquad \text{(A.32)}$$

$$V_{\rm inter} \equiv \frac{1}{8\pi\varepsilon_0} \sum_{i\in m, j\in m'} \frac{e_i e_j}{|\boldsymbol{q}_i - \boldsymbol{q}_j|}. \qquad \text{(A.33)}$$

A.2.1 Density and polarization operators

Introducing the polarization operator into the minimal coupling Hamiltonian makes the Coulomb interaction terms more physically clear. Let $\rho_m(\boldsymbol{r})$ be the density operator of the molecule m given by

$$\rho_m(\boldsymbol{r}) \equiv \sum_{i\in m} e_i \delta(\boldsymbol{r} - \boldsymbol{q}_i). \qquad \text{(A.34)}$$

This can be rewritten by expanding the delta function in a Taylor series using $\boldsymbol{R}_m$, the center of mass of the molecule m, as follows:

$$\begin{aligned} \rho_m(\boldsymbol{r}) &= \sum_{i\in m} e_i \delta(\ (\boldsymbol{r} - \boldsymbol{R}_m) - (\boldsymbol{q}_i - \boldsymbol{R}_m)\ ) \\ &= \sum_{i\in m} e_i \Big[1 - (\boldsymbol{q}_i - \boldsymbol{R}_m) \cdot \boldsymbol{\nabla} \\ &\qquad + \frac{1}{2!} \{(\boldsymbol{q}_i - \boldsymbol{R}_m) \cdot \boldsymbol{\nabla}\}^2 \\ &\qquad + \frac{1}{3!} \{(\boldsymbol{q}_i - \boldsymbol{R}_m) \cdot \boldsymbol{\nabla}\}^3 - \cdots \Big] \delta(\boldsymbol{r} - \boldsymbol{R}_m) \\ &\equiv \rho_m^{\rm true}(\boldsymbol{r}) - \boldsymbol{\nabla} \cdot \boldsymbol{P}_m(\boldsymbol{r}) \qquad \text{(A.35)} \end{aligned}$$

where $\rho_m^{\text{true}}(\boldsymbol{r})$ is the net charge of the molecule m given by

$$\rho_m^{\text{true}}(\boldsymbol{r}) \equiv \left(\sum_{i\in m} e_i\right) \delta(\boldsymbol{r} - \boldsymbol{R}_m) \tag{A.36}$$

and for a neutral molecule it is zero. $\boldsymbol{P}_m(\boldsymbol{r})$ is the polarization of the molecule m given by

$$\boldsymbol{P}_m(\boldsymbol{r}) = \sum_{i\in m} e_i(\boldsymbol{q}_i - \boldsymbol{R}_m) \left[1 - \frac{1}{2!}(\boldsymbol{q}_i - \boldsymbol{R}_m)\cdot\boldsymbol{\nabla} + \frac{1}{3!}\left\{(\boldsymbol{q}_i - \boldsymbol{R}_m)\cdot\boldsymbol{\nabla}\right\}^2 - \cdots\right] \delta(\boldsymbol{r} - \boldsymbol{R}_m). \tag{A.37}$$

Using $1/n = \int_0^1 \lambda^{n-1} d\lambda$ and recalling the Taylor expansion of the delta function, it can be written as

$$\begin{aligned}\boldsymbol{P}_m(\boldsymbol{r}) &= \sum_{i\in m} e_i(\boldsymbol{q}_i - \boldsymbol{R}_m) \int_0^1 d\lambda \left[1 - \lambda(\boldsymbol{q}_i - \boldsymbol{R}_m)\cdot\boldsymbol{\nabla} + \frac{1}{2!}\left\{\lambda(\boldsymbol{q}_i - \boldsymbol{R}_m)\cdot\boldsymbol{\nabla}\right\}^2 - \cdots\right] \delta(\boldsymbol{r} - \boldsymbol{R}_m) \\ &= \sum_{i\in m} e_i(\boldsymbol{q}_i - \boldsymbol{R}_m) \int_0^1 d\lambda \delta(\boldsymbol{r} - \boldsymbol{R} - \lambda(\boldsymbol{q}_i - \boldsymbol{R}_m)) \end{aligned} \tag{A.38}$$

which is the polarization operator I use in the chapter three.

A.2.2 Intermolecular Coulomb interaction

All the discussion in the thesis is restricted to the neutral system, and hence we can write the density as

$$\rho_m(\boldsymbol{r}) = -\boldsymbol{\nabla}\cdot\boldsymbol{P}_m(\boldsymbol{r}) \tag{A.39}$$

Using the density operator, the intermolecular Coulomb interaction terms can be written as

$$V_{\text{inter}} = \sum_{m\neq m'} \frac{1}{8\pi\varepsilon_0} \iint d\boldsymbol{r} d\boldsymbol{r}' \frac{\boldsymbol{\nabla}\cdot\boldsymbol{P}_m(\boldsymbol{r})\boldsymbol{\nabla}'\cdot\boldsymbol{P}_{m'}(\boldsymbol{r}')}{|\boldsymbol{r} - \boldsymbol{r}'|}. \tag{A.40}$$

Integrating this by parts twice and then using the fact that $\boldsymbol{\nabla}' f(|r - r'|) = -\boldsymbol{\nabla} f(|r - r'|)$, we have

$$\begin{aligned} V_{\text{inter}} &= \sum_{m\neq m'} \frac{1}{8\pi\varepsilon_0} \iint d\boldsymbol{r} d\boldsymbol{r}' \boldsymbol{\nabla}\boldsymbol{\nabla}\left(\frac{1}{|\boldsymbol{r} - \boldsymbol{r}'|}\right)\cdot\boldsymbol{P}_m(\boldsymbol{r})\boldsymbol{P}_{m'}(\boldsymbol{r}') \\ &= \frac{1}{8\pi\varepsilon_0} \iint d\boldsymbol{r} d\boldsymbol{r}' \partial_i\partial_j \left(\frac{1}{|\boldsymbol{r} - \boldsymbol{r}'|}\right) \left(\boldsymbol{P}_m(\boldsymbol{r})\right)_i \left(\boldsymbol{P}_{m'}(\boldsymbol{r}')\right)_j . \end{aligned} \tag{A.41}$$

Performing the Fourier transform as $\frac{1}{(|r-r'|)} \to \frac{4\pi}{(2\pi)^{3/2}k^2}$, we obtain

$$\partial_i\partial_j \frac{1}{|\boldsymbol{r} - \boldsymbol{r}'|} = \partial_i\partial_j \frac{1}{(2\pi)^3} \int d\boldsymbol{k} \frac{4\pi e^{i\boldsymbol{k}\cdot(\boldsymbol{r}-\boldsymbol{r}')}}{k^2} \tag{A.42}$$

$$= -\frac{4\pi}{(2\pi)^3} \int d\boldsymbol{k} \frac{k_i k_j}{k^2} e^{i\boldsymbol{k}\cdot(\boldsymbol{r}-\boldsymbol{r}')} \tag{A.43}$$

$$= -4\pi\delta_{ij}^{\parallel}(\boldsymbol{r} - \boldsymbol{r}'), \tag{A.44}$$

where the definition of (A.19) is used at the last equal. Finally, V_{inter} becomes

$$V_{\text{inter}} = \frac{1}{2}\sum_{m\neq m'}\frac{1}{\varepsilon_0}\int d\boldsymbol{r}d\boldsymbol{r}'\delta^{\parallel}_{ij}(\boldsymbol{r}-\boldsymbol{r}')\left(\boldsymbol{P}_m(\boldsymbol{r})\right)_i\left(\boldsymbol{P}_{m'}(\boldsymbol{r}')\right)_j \tag{A.45}$$

$$= \sum_{m<m'}\frac{1}{\varepsilon_0}\int d\boldsymbol{r}\boldsymbol{P}^{\parallel}_m(\boldsymbol{r})\cdot\boldsymbol{P}^{\parallel}_{m'}(\boldsymbol{r}) \tag{A.46}$$

where the fact that $\boldsymbol{A}^{\parallel}\cdot\boldsymbol{B} = \boldsymbol{A}^{\parallel}\cdot\boldsymbol{B}^{\parallel}$ is used. Here the inter-molecular interaction is expressed as the interaction between longitudinal polarizations of molecules m and m'.

A.3 Canonical transformation and multipolar Hamiltonian

H_{int} in the minimal coupling Hamiltonian (A.28) is transformed using next function:

$$S = \frac{1}{\hbar}\int d\boldsymbol{r}\boldsymbol{P}^{\perp}(\boldsymbol{r})\cdot\boldsymbol{A}(\boldsymbol{r}). \tag{A.47}$$

S is the function of $\boldsymbol{q}$ and $\boldsymbol{A}$ and thus these variables remain unchanged by the transformation. Only the momenta $\boldsymbol{p}$ and $\boldsymbol{\Pi}$ will change. As a result, the interaction is described with the polarization and electric field, instead of the momentum of particles and vector potential.

Our strategy here is to obtain new variables by

$$A_{\text{new}} = e^{iS}Ae^{-iS} \tag{A.48}$$

then express the old variables by the new ones as

$$A = A(A_{\text{new}}) \tag{A.49}$$

and using the relation that

$$H_{\text{new}}(p_{\text{new}}, q_{\text{new}}) = H(p(p_{\text{new}}, q_{\text{new}}), q(p_{\text{new}}, q_{\text{new}})) \tag{A.50}$$

where the old variables p, q are expressed with the new variables and substitute them into the old Hamiltonian.

In the calculation I use the next relations that

$$e^{iG\lambda}Ae^{-iG\lambda} = A + i\lambda[G,A] + \left(\frac{i^2\lambda^2}{2!}\right)[G,[G,A]] + \tag{A.51}$$

$$\cdots + \left(\frac{i^n\lambda^n}{n!}\right)[G,[G,[G,\cdots[G,A]]]\cdots] + \cdots, \tag{A.52}$$

which is known as Baker-Hausdorff lemma [184], and

$$[S(q),p] = [S(0),p] + [\partial_q S q, p] + \left[\frac{\partial_q^2 S}{2!}q^2, p\right] + \left[\frac{\partial_q^3 S}{3!}q^3, p\right]\cdots \tag{A.53}$$

$$= \partial_q S[q,p] + \frac{\partial_q^2 S}{2!}[q^2,p] + \frac{\partial_q^3 S}{3!}[q^3,p]\cdots \tag{A.54}$$

$$= (i\hbar)\left[(\partial_q S) + \partial_q(\partial_q S)q + \frac{\partial_q}{2!}(\partial_q S)q^2 + \cdots\right] \tag{A.55}$$

$$= i\hbar\partial_q S \tag{A.56}$$

where $\partial_q \equiv \partial/\partial q$ and the next relation is used

$$[q^n, p] = ni\hbar q^{n-1}. \tag{A.57}$$

The proof is given by the method of induction. For $n = 1$ and 2,

$$[q,p] = i\hbar \tag{A.58}$$

$$[q^2,p] = q[q,p] + [q,p]q = 2i\hbar q \tag{A.59}$$

then assume that the relation for $n = k$ holds, then

$$[q^n,p] = q[q^{n-1},p] + [q,p]q^{n-1}$$

$$= q(n-1)i\hbar q^{n-2} + i\hbar q^{n-1} = ni\hbar q^{n-1} \tag{A.60}$$

thus the relation is true for all n. Now, $[S,p] = i\hbar\partial_q S$ is the function of q then this commutes with $S(q)$, thus we have

$$p_{\text{new}} = e^{iS}pe^{-iS}$$

$$= p + i[S,p] + \frac{i^2}{2!}[S,[S,p]] + \cdots \tag{A.61}$$

$$= p - \hbar\partial_q S \tag{A.62}$$

Bearing in mind these relations, we have

$$\boldsymbol{\Pi}_{\text{mult}} = e^{iS}\boldsymbol{\Pi}_{\text{min}}e^{-iS}$$

$$= \boldsymbol{\Pi}_{\text{min}} - \hbar\frac{\partial S}{\partial \boldsymbol{A}} \tag{A.63}$$

$$= \boldsymbol{\Pi}_{\text{min}} - \boldsymbol{P}^{\perp} \tag{A.64}$$

$$= -\varepsilon_0\boldsymbol{E}^{\perp} - \boldsymbol{P}^{\perp} \tag{A.65}$$

$$\equiv -\boldsymbol{D}^{\perp} \tag{A.66}$$

where the displacement field $\boldsymbol{D}$ is defined. Then the momentum becomes

$$\boldsymbol{p}_{\text{mult}} = \boldsymbol{p}_{\text{min}} - \hbar\frac{\partial S}{\partial \boldsymbol{q}} \tag{A.67}$$

where

$$\begin{aligned}\frac{\partial S}{\partial \boldsymbol{q}} &= \partial_{\boldsymbol{q}}\left(\frac{1}{\hbar}\int d\boldsymbol{r}\boldsymbol{P}^{\perp}\cdot\boldsymbol{A}\right)\\ &= \partial_{\boldsymbol{q}}\left(\frac{1}{\hbar}\int d\boldsymbol{r}e(\boldsymbol{q}-\boldsymbol{R})\int_0^1 d\lambda\delta(\boldsymbol{r}-\boldsymbol{R}-\lambda(\boldsymbol{q}-\boldsymbol{R}))\boldsymbol{A}\right)\\ &= \frac{1}{\hbar}\iint d\boldsymbol{r}d\lambda e\delta(\boldsymbol{r}-\boldsymbol{R}-\lambda(\boldsymbol{q}-\boldsymbol{R}))\boldsymbol{A}\\ &\qquad + \frac{1}{\hbar}\iint d\boldsymbol{r}d\lambda e(\boldsymbol{q}-\boldsymbol{R})\partial_{\boldsymbol{q}}\delta(\boldsymbol{r}-\boldsymbol{R}-\lambda(\boldsymbol{q}-\boldsymbol{R}))\boldsymbol{A} \qquad \text{(A.68)}\end{aligned}$$

For a while, I hide $\boldsymbol{R}$ for clarity. The following derivations are complicated and technically. The important part can be written as

$$\iint d\boldsymbol{r}d\lambda\delta(\boldsymbol{r}-\lambda\boldsymbol{q})\boldsymbol{A} + \iint \boldsymbol{q}_i\left(\partial_{\boldsymbol{q}}\delta(\boldsymbol{r}-\lambda\boldsymbol{q})\right)\boldsymbol{A}_i \qquad \text{(A.69)}$$

$$+\iint\left[\boldsymbol{q}\cdot\partial_{\boldsymbol{q}}\right]\delta(\boldsymbol{r}-\lambda\boldsymbol{q})\boldsymbol{A} - \iint\left[\boldsymbol{q}\cdot\partial_{\boldsymbol{q}}\right]\delta(\boldsymbol{r}-\lambda\boldsymbol{q})\boldsymbol{A} \qquad \text{(A.70)}$$

in the second line, the same term is added and subtracted. Applying the first of the next relations (A.71) to the first term of (A.70), and (A.72) into the seconds of (A.69) and (A.70)

$$(\boldsymbol{q}\cdot\partial_{\boldsymbol{q}})\delta(\boldsymbol{r}-\lambda\boldsymbol{q}) = \lambda\frac{d}{d\lambda}\delta(\boldsymbol{r}-\lambda\boldsymbol{q}) \qquad \text{(A.71)}$$

$$\partial_{\boldsymbol{q}}\delta(\boldsymbol{r}-\lambda\boldsymbol{q}) = -\lambda\boldsymbol{\nabla}\delta(\boldsymbol{r}-\lambda\boldsymbol{q}), \qquad \text{(A.72)}$$

the first terms of eq.(A.69) and (A.70) become

$$\begin{aligned}&\iint d\boldsymbol{r}d\lambda\delta(\boldsymbol{r}-\lambda\boldsymbol{q})\boldsymbol{A} + \iint d\boldsymbol{r}d\lambda\lambda\frac{d}{d\lambda}\delta(\boldsymbol{r}-\lambda\boldsymbol{q})\boldsymbol{A}\\ &\quad= \iint d\boldsymbol{r}d\lambda\frac{d}{d\lambda}\left[\lambda\delta(\boldsymbol{r}-\lambda\boldsymbol{q})\right]\boldsymbol{A}\\ &\quad= \int d\boldsymbol{r}\int_{\lambda=0}^{\lambda=1} d[\lambda\delta(\boldsymbol{r}-\boldsymbol{R}-\lambda(\boldsymbol{q}-\boldsymbol{R}))]\boldsymbol{A}\\ &\quad= \int d\boldsymbol{r}\delta(\boldsymbol{r}-\boldsymbol{q})\boldsymbol{A}(\boldsymbol{r})\\ &\quad= \boldsymbol{A}(\boldsymbol{q}) \qquad \text{(A.73)}\end{aligned}$$

where I recalled $\boldsymbol{R}$ in the third line. Next, the second terms of (A.69) and (A.70) can

be written as

$$\begin{aligned}
&\iint d\boldsymbol{r}d\lambda\ q_j\partial_{q_i}\delta(\boldsymbol{r}-\lambda\boldsymbol{q})A_j - \iint d\boldsymbol{r}d\lambda(q_j\partial_{q_j})\delta(\boldsymbol{r}-\lambda\boldsymbol{q})A_i \\
&= -\iint d\boldsymbol{r}d\lambda\ q_j\partial_i\lambda\delta(\boldsymbol{r}-\lambda\boldsymbol{q})A_j + \iint d\boldsymbol{r}d\lambda(q_j\partial_j)\lambda\delta(\boldsymbol{r}-\lambda\boldsymbol{q})A_i \\
&\quad \text{(integrate by parts with respect to } d\boldsymbol{r}) \\
&= \int d\boldsymbol{r}q_j\int_0^1 d\lambda\ \lambda\delta(\boldsymbol{r}-\lambda\boldsymbol{q})\left(\partial_jA_i-\partial_iA_j\right) \\
&= \int d\boldsymbol{r}q_j\int_0^1 d\lambda\lambda\delta(\boldsymbol{r}-\lambda\boldsymbol{q})\varepsilon_{ijk}B_k,
\end{aligned} \tag{A.74}$$

where $\partial_j \equiv \partial/\partial_{r_j}$ and ε_{ijk} is the Levi-Civita symbol. Finally, defining $\boldsymbol{n}$ as follows

$$\boldsymbol{n}_i \equiv e_i(\boldsymbol{q}_i-\boldsymbol{R}_m)\int_0^1 \lambda\delta(\boldsymbol{r}-\boldsymbol{R}_m-\lambda(\boldsymbol{q}_i-\boldsymbol{R}_m))d\lambda \tag{A.75}$$

and applying this to eq.(A.74) and together with (A.67), (A.68), and (A.73), the multipolar momentum is

$$\boldsymbol{p}_{\text{mult}} = \boldsymbol{p}_{\text{min}} + e\boldsymbol{A} - \int d\boldsymbol{r}\boldsymbol{n}\times\boldsymbol{B} \tag{A.76}$$

Thus,

$$\boldsymbol{\Pi}_{\text{min}} = \boldsymbol{\Pi}_{\text{mult}} + \boldsymbol{P}^{\perp} \tag{A.77}$$

$$\boldsymbol{p}_{\text{min}} = \boldsymbol{p}_{\text{mult}} - e\boldsymbol{A} + \int d\boldsymbol{r}\boldsymbol{n}\times\boldsymbol{B} \tag{A.78}$$

and substituting them into eq. (A.26) with omitting the summation and related subscriptions for clarity, we have

$$\begin{aligned}
H_{\text{mult}} &= \left[\frac{1}{2m}\left(\boldsymbol{p}-e\boldsymbol{A}+\int d\boldsymbol{r}\boldsymbol{n}\times\boldsymbol{B}\right)^2+V\right]+\frac{1}{2}\int d\boldsymbol{r}\left[\frac{\left(\boldsymbol{\Pi}+\boldsymbol{P}^{\perp}\right)^{\boldsymbol{2}}}{\varepsilon_0}+c^2\varepsilon_0\boldsymbol{B}^2\right] \\
&\qquad +\frac{e}{m}\left(\boldsymbol{p}-e\boldsymbol{A}+\int d\boldsymbol{r}\boldsymbol{n}\times\boldsymbol{B}\right)\cdot\boldsymbol{A}+\frac{e^2}{2m}\boldsymbol{A}^2+V_{\text{inter}} \\
&= \left[\frac{1}{2m}\left(\boldsymbol{p}+\int d\boldsymbol{r}\boldsymbol{n}\times\boldsymbol{B}\right)^2+\frac{e^2}{2m}\boldsymbol{A}^2-\frac{\left(\boldsymbol{p}+\int d\boldsymbol{r}\boldsymbol{n}\times\boldsymbol{B}\right)}{m}\cdot\boldsymbol{A}+V\right] \\
&\qquad +H_{\text{rad}}+\frac{e}{m}\left(\boldsymbol{p}+\int d\boldsymbol{r}\boldsymbol{n}\times\boldsymbol{B}\right)\cdot\boldsymbol{A}-\frac{e^2}{m}\boldsymbol{A}^2+\frac{e^2}{2m}\boldsymbol{A}^2+V_{\text{inter}} \\
&= \left[\frac{1}{2m}\left(\boldsymbol{p}+\int d\boldsymbol{r}\boldsymbol{n}\times\boldsymbol{B}\right)^2+V\right]+\frac{1}{2}\int d\boldsymbol{r}\left[\varepsilon_0^{-1}\left(\boldsymbol{\Pi}+\boldsymbol{P}^{\perp}\right)^2+c^2\varepsilon_0\boldsymbol{B}^2\right]+V_{\text{inter}}
\end{aligned} \tag{A.79}$$

where the subscription $_{\text{mult}}$ is omitted from $\boldsymbol{p}_{\text{mult}}$ and $\boldsymbol{\Pi}_{\text{mult}}$. Expanding and regrouping this equation further, we have

$$\begin{aligned} H_{\text{mult}} &= \left(\frac{\boldsymbol{p}^2}{2m} + V\right) + \frac{1}{2}\int d\boldsymbol{r}\left\{\frac{\boldsymbol{\Pi}^2}{\varepsilon_0} + c^2\varepsilon_0\boldsymbol{B}^2\right\} \\ &\quad + \frac{1}{\varepsilon_0}\int d\boldsymbol{r}\boldsymbol{P}^{\perp}\cdot\boldsymbol{\Pi} + V_{\text{inter}} + \frac{1}{2\varepsilon_0}\int d\boldsymbol{r}|\boldsymbol{P}^{\perp}|^2 \qquad \text{(A.80)} \\ &\quad + \frac{\boldsymbol{p}}{m}\cdot\int d\boldsymbol{r}\ \boldsymbol{n}\times\boldsymbol{B} + \frac{1}{2m}\left(\int d\boldsymbol{r}\boldsymbol{n}\times\boldsymbol{B}\right)^2 \qquad \text{(A.81)} \\ &= H_{\text{mol}} + H_{\text{rad}} + H_{\text{int}} + V_{\text{inter}} + H_{\text{self}} + H_{\text{magn}} \qquad \text{(A.82)} \end{aligned}$$

where

$$H_{\text{mol}} = \frac{\boldsymbol{p}^2}{2m} + V \qquad \text{(A.83)}$$

$$H_{\text{rad}} = \frac{1}{2}\int d\boldsymbol{r}\frac{\boldsymbol{\Pi}^2}{\varepsilon_0} + c^2\varepsilon_0\boldsymbol{B}^2 \qquad \text{(A.84)}$$

$$H_{\text{int}} = \frac{1}{\varepsilon_0}\int d\boldsymbol{r}\boldsymbol{P}^{\perp}\cdot\boldsymbol{\Pi} \qquad \text{(A.85)}$$

$$H_{\text{self}} = \frac{1}{2\varepsilon_0}\int d\boldsymbol{r}|\boldsymbol{P}^{\perp}|^2 \qquad \text{(A.86)}$$

$$\qquad \text{(A.87)}$$

and H_{magn} is the remaining terms as in (A.81). It should be noted that H_{int} is not the same as appeared in chapter 3.

A.4 Semiclassical equation of motion

The equation of motion of an operator of material can be written as

$$\frac{\hbar}{i}\frac{dQ}{dt} = [H_{\text{mol}} + H_{\text{int}} + V_{\text{inter}} + H_{\text{self}}, Q] \qquad \text{(A.88)}$$

where the field operators and magnetic terms are omitted. The field operator H_{rad} commutes with any material operators. Magnetic terms are negligible in the present study as discussed in chapter 4.

To derivate the equation the basis of this thesis, $H_{\text{int}} + H_{\text{self}}$ are focused. The Poisson bracket we focus on becomes

$$[H_{\text{int}} + H_{\text{self}},\ Q] = \frac{1}{2\varepsilon_0}\int d\boldsymbol{r}\left[2\boldsymbol{P}^{\perp}\cdot\boldsymbol{\Pi} + \boldsymbol{P}^{\perp 2},\ Q\right]. \qquad \text{(A.89)}$$

Writing $2\boldsymbol{P}^{\perp}\cdot\boldsymbol{\Pi} = \boldsymbol{P}^{\perp}\cdot\boldsymbol{\Pi} + \boldsymbol{\Pi}\cdot\boldsymbol{P}$, the Poisson bracket concerning H_{int} can be

written as

$$\begin{aligned}\left[2\boldsymbol{P}^{\perp}\cdot\boldsymbol{\Pi},\ Q\right] &= \left[\boldsymbol{P}^{\perp}\cdot\boldsymbol{\Pi},\ Q\right]+\left[\boldsymbol{\Pi}\cdot\boldsymbol{P}^{\perp},\ Q\right]\\ &= \boldsymbol{\Pi}\left[\boldsymbol{\Pi},\ Q\right]+\left[\boldsymbol{P}^{\perp},\ Q\right]\boldsymbol{\Pi}+\boldsymbol{\Pi}\left[\boldsymbol{P}^{\perp},\ Q\right]+\left[\boldsymbol{\Pi},\ Q\right]\boldsymbol{P}^{\perp}\\ &= \left[\boldsymbol{P}^{\perp},\ Q\right]\boldsymbol{\Pi}+\boldsymbol{\Pi}\left[\boldsymbol{P}^{\perp},\ Q\right] \qquad \text{(A.90)}\\ &= \left[\boldsymbol{P}^{\perp},\ Q\right]\left(-\varepsilon_0\boldsymbol{E}^{\perp}-\boldsymbol{P}^{\perp}\right)+\left(-\varepsilon_0\boldsymbol{E}^{\perp}-\boldsymbol{P}^{\perp}\right)\left[\boldsymbol{P}^{\perp},\ Q\right]\\ &= -\varepsilon_0\left[\left[\boldsymbol{P}^{\perp},\ Q\right],\boldsymbol{E}^{\perp}\right]_{+}-\left[\boldsymbol{P}^{\perp 2},\ Q\right] \qquad \text{(A.91)}\end{aligned}$$

where using the fact that the pure-field operator $\boldsymbol{\Pi}$ commutes with any material operator. The anticommutation relation is defined as $[A,B]_{+}\equiv AB+BA$. Substituting this into (A.89), we have

$$\left[H_{\text{int}}+H_{\text{self}},\ Q\right]=-\frac{1}{2}\int d\boldsymbol{r}\left[\left[\boldsymbol{P}^{\perp},\ Q\right],\ \boldsymbol{E}^{\perp}\right]_{+}. \qquad \text{(A.92)}$$

Finally, taking expectation value of $\boldsymbol{E}^{\perp}$ and expressing the expectation value as $\left\langle\boldsymbol{E}^{\perp}\right\rangle$, we have

$$\left[H_{\text{int}}+H_{\text{self}},\ Q\right]=-\int d\boldsymbol{r}\left[\boldsymbol{P}^{\perp}\cdot\left\langle\boldsymbol{E}^{\perp}\right\rangle,\ Q\right] \qquad \text{(A.93)}$$

Therefore, the effective Multipolar Hamiltonian can be written as follows:

$$H_{\text{mult}}^{\text{eff}}=H_{\text{mol}}+V_{\text{inter}}-\int d\boldsymbol{r}\boldsymbol{P}^{\perp}\cdot\left\langle\boldsymbol{E}^{\perp}\right\rangle. \qquad \text{(A.94)}$$

This is the starting point Hamiltonian for the present study, where $\boldsymbol{P}^{\perp}\cdot\left\langle\boldsymbol{E}^{\perp}\right\rangle$ is written as $\hat{\boldsymbol{P}}\cdot\boldsymbol{E}^{\perp}$ using the fact that $\boldsymbol{A}\cdot\boldsymbol{B}^{\perp}=\boldsymbol{A}^{\perp}\cdot\boldsymbol{B}^{\perp}$ and the operator is distinguished from the classical values by wearing the hat.

Appendix B

About magnetic interactions

The validation in neglecting the magnetic interactions in the near-field interaction based on the dipole radiation is discussed. As derived in Appendix A, the exact light-matter interaction term $\hat{H}_{\rm int}$ which acts on a molecule is given by

$$\begin{aligned}\hat{H}_{\rm int} = &- \int \hat{\boldsymbol{P}}(\boldsymbol{r}) \cdot \boldsymbol{E}(\boldsymbol{r}) d\boldsymbol{r} - \int \hat{\boldsymbol{M}}(\boldsymbol{r}) \cdot \boldsymbol{B}(\boldsymbol{r}) d\boldsymbol{r} \\ &+ \frac{1}{2} \int \hat{O}_{ij}(\boldsymbol{r}, \boldsymbol{r}') B_i(\boldsymbol{r}) B_j(\boldsymbol{r}) d\boldsymbol{r} d\boldsymbol{r}', \end{aligned} \tag{B.1}$$

where the magnetization field $\hat{\boldsymbol{M}}$ and the diamagnetization field O_{ij} are given by

$$\begin{aligned}\hat{M}(\boldsymbol{r}) = &-e \sum_{\alpha} \left[(\hat{\boldsymbol{q}}_\alpha - \boldsymbol{R}) \times \dot{\hat{\boldsymbol{q}}}_\alpha \right] \\ &\times \int_0^1 \lambda \delta(\boldsymbol{r} - \boldsymbol{R} - \lambda(\hat{q}_\alpha - \boldsymbol{R})) d\lambda \end{aligned} \tag{B.2}$$

$$\begin{aligned} O_{ij} = &\left(\frac{e^2}{m} \right) \varepsilon_{ikl} \varepsilon_{jml} \sum_{\alpha\beta} (\hat{\boldsymbol{q}}_\alpha - \boldsymbol{R})_k (\hat{\boldsymbol{q}}_\beta - \boldsymbol{R})_m \\ &\times \int \lambda \delta(\boldsymbol{r} - \boldsymbol{R} - \lambda(\hat{\boldsymbol{q}}_\alpha - \boldsymbol{R})) \\ &\times \lambda' \delta(\boldsymbol{r}' - \boldsymbol{R} - \lambda'(\hat{\boldsymbol{q}}_\beta - \boldsymbol{R})) d\lambda d\lambda'. \end{aligned} \tag{B.3}$$

In (B.2), $\dot{\hat{\boldsymbol{q}}}$ is the time derivative of $\hat{\boldsymbol{q}}$, used later as the electron velocity v. In (B.3), m is electron mass and ε_{ijk} is the Levi-Civita symbol. In the dipole radiation, the electric field is given by (3.11) and the magnetic field is

$$\boldsymbol{B} = \frac{\omega \mu_0 k^2}{4\pi} [\boldsymbol{n} \times \boldsymbol{\mu}] \left(\frac{i}{(kr)^2} + \frac{1}{(kr)} \right) e^{ikr}, \tag{B.4}$$

where $\boldsymbol{n} \equiv \boldsymbol{r}/r$. $\omega = ck$ is the angular velocity of the field, where k is the wavenumber. μ_0 is magnetic permeability of space. In the near field zone where $(kr)^{-3} \gg (kr)^{-2} \gg$

$(kr)^{-1}$, the leading contributions are (3.11a) for the electric field and the first term in (B.4) for the magnetic field. It is, thus, sometimes claimed that the main component of the near-field is (3.11a) [133]. Rigorously speaking, however, the electric and magnetic coupling terms that appear in the multipolar Hamiltonian should be compared, in addition to the simple comparison of these electric and magnetic fields. The absolute values of the coupling terms are estimated as follows:

$$P_i E_i \sim er \cdot \frac{\mu}{4\pi\varepsilon_0 r^3} = \frac{e\mu}{4\pi\varepsilon_0 r^2} \tag{B.5}$$

$$M_i B_i \sim erv \cdot \frac{\omega\mu_0\mu}{4\pi r^2} = \frac{e\mu v\omega\mu_0}{4\pi r} \tag{B.6}$$

$$O_{ij} B_i B_j \sim \frac{e^2}{m} r^2 \cdot \left(\frac{\omega\mu_0\mu}{4\pi r^2}\right)^2 = \frac{e^2\mu^2\omega^2\mu_0^2}{16\pi^2 r^2 m}, \tag{B.7}$$

where r represents the electron coordinate, and that is also used as the distance between the molecule and the radiating dipole. This is because these two length scales are set to be in the same order. μ is the absolute value of the dipole moment of the source. To compare the coupling terms, I will calculate $\alpha \equiv M_i B_i / P_i E_i$ and $\beta \equiv O_{ij} B^2 / P_i E_i$.

The right hand side of (B.5) is obtained as follows. According to the definition of the polarization, it can be written as $P \sim er$, where r is the size of a molecule. Since I consider the distance between the molecule and the radiation source to be the same order as the molecular size, (3.11a) can be approximate as $E \sim \mu/4\pi\varepsilon_0 r^3$. In (B.6), the velocity of electron $v = \dot{q}$ in (B.2) is estimated as follows. In the present model, the electron is forced to oscillate by the near field. However, the electrons are always bounded by the molecule in this study, thus it travels no more than the molecular size of about 1 nm. The electrons move at most from one side of the molecule to the other side in a half of the laser cycle $T = 2\pi/\omega = \lambda/c$, where λ is the wavelength of the dipole radiation which is about 1000 nm for UV-vis light used in this study. Thus v can be rewritten as $v \sim r/(T/2) \sim rc/\lambda$. Now, α becomes much simple by inserting (B.5) and (B.6):

$$\alpha \equiv \frac{M_i B_i}{P_i E_i} \sim rv\omega\varepsilon_0\mu_0 \sim r \cdot \frac{rc}{\lambda} \cdot \frac{c}{\lambda} \cdot \frac{1}{c^2} = \left(\frac{r}{\lambda}\right)^2 \tag{B.8}$$

where I used $\omega \sim c/\lambda$ and $\varepsilon_0\mu_0 = 1/c^2$. In the present study, I have set the molecular size to be $r \sim 1$ nm, and wavelength $\lambda \sim 1000$ nm. Thus we have $\alpha \sim 10^{-6}$, that is, $M_i B_i$ is much smaller than $P_i E_i$ by the order of 10^{-6}. This is enough to discard the $M_i B_i$ terms in studying the near field interactions.

Next β becomes

$$\beta \equiv \frac{O_{ij} B^2}{P_i E_i} \sim \frac{e\mu\omega^2\varepsilon_0\mu_0^2}{4\pi m} = \frac{e\mu\mu_0\pi}{m\lambda^2} \sim \frac{e^2 r\mu_0}{m\lambda^2} \tag{B.9}$$

where I use $\omega = 2\pi c/\lambda$ and $\varepsilon_0\mu_0 = 1/c^2$. The dipole moment of the source is set to be in the same scale as the molecule, namely, $\mu \sim er$. We can estimate β by using the present parameters in SI units, such as $e \sim 10^{-19}$ [C], $r \sim 10^{-9}$ [m], $\mu_0 \sim 10^{-7}$ [N/A^2],

$m \sim 10^{-30}$ [kg], and $\lambda \sim 10^{-6}$ [m]. Finally, β is found to be in the order of 10^{-37}. This is quite small compared to the other two terms in the multipolar Hamiltonian. From the above estimations, it is adequate to discard the magnetic interactions to study the electron dynamics interacting with the dipole radiation in such a short distances.

Bibliography

[1] Y. Negishi, K. Nobusada, and T. Tsukuda. *J. Am. Chem. Soc.*, 127:5261–5270, 2005.

[2] Y. Shichibu, Y. Negishi, H. Tsunoyama, M. Kanehara, T. Teranishi, and T. Tsukuda. *Small*, 3:835–839, 2007.

[3] Y. Shichibu, Y. Negishi, T. Tsukuda, and T. Teranishi. *J. Am. Chem. Soc.*, 127:13464–13465, 2005.

[4] Y. Negishi, H. Tsunoyama, M. Suzuki, N. Kawamura, M. M. Matsushita, K. Maruyama, T. Sugawara, T. Yokoyama, and T. Tsukuda. *J. Am. Chem. Soc.*, 128:12034–12035, 2006.

[5] Y. Negishi, N. K. Chaki, Y. Shichibu, R. L. Whetten, and T. Tsukuda. *J. Am. Chem. Soc.*, 129:11322, 2007.

[6] Y. Shichibu, Y. Negishi, T. Watanabe, N. K. Chaki, H. Kawaguchi, and T. Tsukuda. *J. Phys. Chem. C*, 111:7845–7847, 2007.

[7] R. L. Whetten, J. T. Khoury, M. M. Alvarez, S. Murthy, I. Vezmar, Z. L. Wang, P. W. Stephens, C. L. Cleveland, W. D. Luedtke, and U. Landman. *Advanced Materials*, 8:428–&, 1996.

[8] M. A. Reed, C. Zhou, C. J. Muller, T. P. Burgin, and J. M. Tour. *Science*, 278:252–254, 1997.

[9] C. Joachim, J. K. Gimzewski, and A. Aviram. *Nature*, 408:541–548, 2000.

[10] A. N. Shipway, E. Katz, and I. Willner. *ChemPhysChem*, 1:18–52, 2000.

[11] A. Sanchez, S. Abbet, U. Heiz, W. D. Schneider, H. Hakkinen, R. N. Barnett, and U. Landman. *Journal of Physical Chemistry A*, 103:9573–9578, 1999.

[12] K. S. Min, K. V. Shcheglov, C. M. Yang, H. A. Atwater, M. L. Brongersma, and A. Polman. *Appl. Phys. Lett.*, 68:2511–2513, 1996.

[13] K. S. Min, K. V. Shcheglov, C. M. Yang, H. A. Atwater, M. L. Brongersma, and A. Polman. *Appl. Phys. Lett.*, 69:2033–2035, 1996.

[14] M. L. Brongersma, A. Polman, K. S. Min, E. Boer, T. Tambo, and H. A. Atwater. *Appl. Phys. Lett.*, 72:2577–2579, 1998.

[15] M. L. Brongersma, J. W. Hartman, and H. A. Atwater. *Phys. Rev. B*, 62:16356–16359, 2000.

[16] S. A. Maier, M. L. Brongersma, P. G. Kik, S. Meltzer, A. A. G. Requicha, and H. A. Atwater. *Adv. Mater.*, 13:1501–+, 2001.

[17] S. A. Maier, P. G. Kik, and H. A. Atwater. *Appl. Phys. Lett.*, 81:1714–1716, 2002.

[18] S. A. Maier, M. L. Brongersma, P. G. Kik, and H. A. Atwater. *Phys. Rev. B*, 65:193408, 2002.

[19] S. A. Maier, P. G. Kik, H. A. Atwater, S. Meltzer, E. Harel, B. E. Koel, and A. A. G. Requicha. *Nature Mater.*, 2:229–232, 2003.

[20] S. A. Maier and H. A. Atwater. *J. Appl. Phys.*, 98:011101, 2005.

[21] W. L. Barnes, A. Dereux, and T. W. Ebbesen. *Nature*, 424:824–830, 2003.

[22] E. Ozbay. *Science*, 311:189–193, 2006.

[23] C. Girard and A. Dereux. *Rep. Prog. Phys.*, 59:657–699, 1996.

[24] C. Girard, C. Joachim, and S. Gauthier. *Rep. Prog. Phys.*, 63:893–938, 2000.

[25] C. Girard. *Rep. Prog. Phys.*, 68:1883–1933, 2005.

[26] S. Maruo, O. Nakamura, and S. Kawata. *Opt. Lett.*, 22:132–134, 1997.

[27] S. Kawata and Y. Kawata. *Chem. Rev.*, 100:1777–1788, 2000.

[28] S. Kawata, H. B. Sun, T. Tanaka, and K. Takada. *Nature*, 412:697–698, 2001.

[29] L. Novotny, D. W. Pohl, and P. Regli. *J. Opt. Soc. Am. A-Opt. Image Sci. Vis.*, 11:1768–1779, 1994.

[30] B. Hecht, H. Bielefeldt, Y. Inouye, D. W. Pohl, and L. Novotny. *J. Appl. Phys.*, 81:2492–2498, 1997.

[31] E. J. Sanchez, L. Novotny, and X. S. Xie. *Phys. Rev. Lett.*, 82:4014–4017, 1999.

[32] A. Bouhelier, M. Beversluis, A. Hartschuh, and L. Novotny. *Phys. Rev. Lett.*, 90:013903, 2003.

[33] L. Novotny. *Nature*, 455:887–887, 2008.

[34] K. Imura, T. Nagahara, and H. Okamoto. *J. Chem. Phys.*, 122:154701, 2005.

[35] J. K. Lim, K. Imura, T. Nagahara, S. K. Kim, and H. Okamoto. *Chem. Phys. Lett.*, 412:41–45, 2005.

[36] K. Imura and H. Okamoto. *Opt. Lett.*, 31:1474–1476, 2006.

[37] H. Okamoto and K. Imura. *Journal of Materials Chemistry*, 16:3920–3928, 2006.

[38] K. Imura and H. Okamoto. *Phys. Rev. B*, 77:041401, 2008.

[39] K. Imura, T. Nagahara, and H. Okamoto. *J. Am. Chem. Soc.*, 126:12730–12731, 2004.

[40] K. Imura, T. Nagahara, and H. Okamoto. *J. Phys. Chem. B*, 108:16344–16347, 2004.

[41] M. Ohtsu. *J. Lightwave Technol.*, 13:1200–1221, 1995.

[42] K. Kobayashi, S. Sangu, H. Ito, and M. Ohtsu. *Phys. Rev. A*, 6301:013806, 2001.

[43] M. Ohtsu, K. Kobayashi, T. Kawazoe, S. Sangu, and T. Yatsui. *IEEE J. Sel. Top. Quantum Electron.*, 8:839–862, 2002.

[44] A. V. Zayats, II Smolyaninov, and A. A. Maradudin. *Phys. Rep.-Rev. Sec. Phys. Lett.*, 408:131–314, 2005.

[45] K. Cho. *Prog. Theor. Phys. Suppl.*, pages 225–233, 1991.

[46] H. Ishihara, K. Cho, K. Akiyama, N. Tomita, Y. Nomura, and T. Isu. *Physical Review Letters*, 89:017402, 2002.

[47] H. Ishihara. *J. Phys.-Condes. Matter*, 16:R247–R273, 2004.

[48] H. Ishihara, J. Kishimoto, and K. Sugihara. Anomalous mode structure of a radiation-exciton coupled system beyond the long-wavelength approximation regime. pages 343–346. Elsevier Science Bv, 2004. ISI Document Delivery No.: 822WT Times Cited: 6 Cited Reference Count: 13.

[49] T. Iida and H. Ishihara. *Optics Letters*, 27:754–756, 2002.

[50] T. Iida and H. Ishihara. *Physical Review Letters*, 90:057403, 2003.

[51] T. Iida and H. Ishihara. Optically induced force between nano-particles irradiated by electronic resonant light. pages 151–155, 2005.

[52] T. Iida and H. Ishihara. *Physical Review Letters*, 97:117402, 2006.

[53] T. Iida and H. Ishihara. *Physical Review B*, 77:245319, 2008.

[54] O. Keller. *Phys. Rep.-Rev. Sec. Phys. Lett.*, 268:85–262, 1996.

[55] O. Keller. *Phys. Rep.-Rev. Sec. Phys. Lett.*, 411:1–232, 2005.

[56] J. Y. Yan, W. Zhang, S. Q. Duan, X. G. Zhao, and A. O. Govorov. *Phys. Rev. B*, 77:165301, 2008.

[57] P. L. Hernandez-Martinez and A. O. Govorov. *Phys. Rev. B*, 78:035314, 2008.

[58] D. Neuhauser and K. Lopata. *J. Chem. Phys.*, 127:154715, 2007.

[59] D. Neuhauser and K. Lopata. *J. Chem. Phys.*, 129:134106, 2008.

[60] R. Baer and D. Neuhauser. *J. Chem. Phys.*, 125:074709, 2006.

[61] K. Lopata, D. Neuhauser, and R. Baer. *J. Chem. Phys.*, 127:154714, 2007.

[62] Matthias Brack. *Rev. Mod. Phys.*, 65:677, 1993.

[63] Walt A. de Heer. *Rev. Mod. Phys.*, 65:611, 1993.

[64] P. Schwerdtfeger. *Angew. Chem. Int. Ed.*, 42:1892–1895, 2003.

[65] P. Pyykko. *Angew. Chem. Int. Ed.*, 43:4412–4456, 2004.

[66] P. Pyykko. *Inorg. Chim. Acta*, 358:4113–4130, 2005.

[67] P. Pyykko. *Chem. Soc. Rev.*, 37:1967–1997, 2008.

[68] E. M. Fernandez, J. M. Soler, I. L. Garzon, and L. C. Balbas. *Phys. Rev. B*, 70:165403, 2004.

[69] H. Hakkinen, M. Moseler, and U. Landman. *Phys. Rev. Lett.*, 89:033401, 2002.

[70] A. C. Templeton, M. P. Wuelfing, and R. W. Murray. *Accounts Chem. Res.*, 33:27–36, 2000.

[71] M. C. Daniel and D. Astruc. *Chem. Rev.*, 104:293–346, 2004.

[72] P. Crespo, R. Litran, T. C. Rojas, M. Multigner, J. M. de la Fuente, J. C. Sanchez-Lopez, M. A. Garcia, A. Hernando, S. Penades, and A. Fernandez. *Phys. Rev. Lett.*, 93:087204, 2004.

[73] C. Gonzalez, Y. Simon-Manso, M. Marquez, and V. Mujica. *J. Phys. Chem. B*, 110:687–691, 2006.

[74] M. Okumura, Y. Kitagawa, T. Kawakami, T. Taniguchi, and K. Yamaguchi. *Synth. Met.*, 154:313–316, 2005.

[75] U. Simon. *Adv. Mater.*, 10:1487–1492, 1998.

[76] E. G. Emberly and G. Kirczenow. *Phys. Rev. B*, 58:10911–10920, 1998.

[77] H. Hakkinen, R. N. Barnett, A. G. Scherbakov, and U. Landman. *J. Phys. Chem. B*, 104:9063–9066, 2000.

[78] J. M. Seminario, C. E. De la Cruz, and P. A. Derosa. *J. Am. Chem. Soc.*, 123:5616–5617, 2001.

[79] X. D. Cui, A. Primak, X. Zarate, J. Tomfohr, O. F. Sankey, A. L. Moore, T. A. Moore, D. Gust, G. Harris, and S. M. Lindsay. *Science*, 294:571–574, 2001.

[80] J. Park, A. N. Pasupathy, J. I. Goldsmith, C. Chang, Y. Yaish, J. R. Petta, M. Rinkoski, J. P. Sethna, H. D. Abruna, P. L. McEuen, and D. C. Ralph. *Nature*, 417:722–725, 2002.

[81] A. Nitzan and M. A. Ratner. *Science*, 300:1384–1389, 2003.

[82] I. Carmeli, G. Leitus, R. Naaman, S. Reich, and Z. Vager. *J. Chem. Phys.*, 118:10372–10375, 2003.

[83] A. Hernando, P. Crespo, and M. A. Garcia. *Phys. Rev. Lett.*, 96:057206, 2006.

[84] A. Hernando, P. Crespo, M. A. Garcia, E. F. Pinel, J. de la Venta, A. Fernandez, and S. Penades. *Phys. Rev. B*, 74:052403, 2006.

[85] Z. Vager and R. Naaman. *Phys. Rev. Lett.*, 92:087205, 2004.

[86] J. de la Venta, A. Pucci, E. F. Pinel, M. A. Garcia, C. D. J. Fernandez, P. Crespo, P. Mazzoldi, G. Ruggeri, and A. Hernando. *Adv. Mater.*, 19:875–+, 2007.

[87] Y. Yamamoto, T. Miura, M. Suzuki, N. Kawamura, H. Miyagawa, T. Nakamura, K. Kobayashi, T. Teranishi, and H. Hori. *Phys. Rev. Lett.*, 93:116801, 2004.

[88] H. Hori, Y. Yamamoto, T. Iwamoto, T. Miura, T. Teranishi, and M. Miyake. *Phys. Rev. B*, 69:174411, 2004.

[89] K. Yabana, T. Nakatsukasa, J. I. Iwata, and G. F. Bertsch. Real-time, real-space implementation of the linear response time-dependent density-functional theory. pages 1121–1138. Wiley-V C H Verlag Gmbh, 2006.

[90] T. Huang and R. W. Murray. *J. Phys. Chem. B*, 105:12498–12502, 2001.

[91] D. Lee, R. L. Donkers, G. L. Wang, A. S. Harper, and R. W. Murray. *J. Am. Chem. Soc.*, 126:6193–6199, 2004.

[92] T. G. Schaaff, M. N. Shafigullin, J. T. Khoury, I. Vezmar, R. L. Whetten, W. G. Cullen, P. N. First, C. GutierrezWing, J. Ascensio, and M. J. JoseYacaman. *J. Phys. Chem. B*, 101:7885–7891, 1997.

[93] T. G. Schaaff and R. L. Whetten. *J. Phys. Chem. B*, 104:2630–2641, 2000.

[94] T. P. Bigioni, R. L. Whetten, and O. Dag. *J. Phys. Chem. B*, 104:6983–6986, 2000.

[95] S. Link, A. Beeby, S. FitzGerald, M. A. El-Sayed, T. G. Schaaff, and R. L. Whetten. *J. Phys. Chem. B*, 106:3410–3415, 2002.

[96] S. D. Bader. *Rev. Mod. Phys.*, 78:1–15, 2006.

[97] B. K. Teo and K. Keating. *J. Am. Chem. Soc.*, 106:2224–2226, 1984.

[98] B. K. Teo, H. Zhang, and X. B. Shi. *J. Am. Chem. Soc.*, 112:8552–8562, 1990.

[99] B. K. Teo and H. Zhang. *Inorg. Chem.*, 30:3115–3116, 1991.

[100] S. N. Khanna and P. Jena. *Phys. Rev. Lett.*, 69:1664–1667, 1992.

[101] D. E. Bergeron, P. J. Roach, A. W. Castleman, N. Jones, and S. N. Khanna. *Science*, 307:231–235, 2005.

[102] K. Imura, H. Okamoto, M. K. Hossain, and M. Kitajima. *Nano Lett.*, 6:2173–2176, 2006.

[103] K. Imura and H. Okamoto. *Bull. Chem. Soc. Jpn.*, 81:659–675, 2008.

[104] E. Betzig, J. K. Trautman, T. D. Harris, J. S. Weiner, and R. L. Kostelak. *Science*, 251:1468–1470, 1991.

[105] E. Betzig, P. L. Finn, and J. S. Weiner. *Applied Physics Letters*, 60:2484–2486, 1992.

[106] E. Betzig and J. K. Trautman. *Science*, 257:189–195, 1992.

[107] E. Betzig and R. J. Chichester. *Science*, 262:1422–1425, 1993.

[108] R. C. Dunn. *Chem. Rev.*, 99:2891–+, 1999.

[109] A. Lewis, H. Taha, A. Strinkovski, A. Manevitch, A. Khatchatouriants, R. Dekhter, and E. Ammann. *Nature Biotechnology*, 21:1377–1386, 2003.

[110] J. Kim and K. B. Song. *Micron*, 38:409–426, 2007.

[111] K. Imura, T. Nagahara, and H. Okamoto. *Chem. Phys. Lett.*, 400:500–505, 2004.

[112] K. Imura, T. Nagahara, and H. Okamoto. *J. Phys. Chem. B*, 109:13214–13220, 2005.

[113] H. Okamoto and K. Imura. Near-field optical imaging of nanoscale optical fields and plasmon waves. pages 6055–6062, 2008.

[114] S. M. Nie and S. R. Emery. *Science*, 275:1102–1106, 1997.

[115] D. L. Jeanmaire and R. P. Vanduyne. *J. Electroanal. Chem.*, 84:1–20, 1977.

[116] Fleischm.M, P. J. Hendra, and McQuilla.Aj. *Chem. Phys. Lett.*, 26:163–166, 1974.

[117] M. G. Albrecht and J. A. Creighton. *J. Am. Chem. Soc.*, 99:5215–5217, 1977.

[118] F. Kulzer and M. Orrit. *Annu. Rev. Phys. Chem.*, 55:585–611, 2004.

[119] P. G. Etchegoin and E. C. Le Ru. *Phys. Chem. Chem. Phys.*, 10:6079–6089, 2008.

[120] M. K. Hossain, T. Shimada, M. Kitajima, K. Imura, and H. Okamoto. *Langmuir*, 24:9241–9244, 2008.

[121] S. Kim, J. H. Jin, Y. J. Kim, I. Y. Park, Y. Kim, and S. W. Kim. *Nature*, 453:757–760, 2008.

[122] K. Kamada, Y. Tanamura, K. Ueno, K. Ohta, and H. Misawa. *J. Phys. Chem. C*, 111:11193–11198, 2007.

[123] K. Ueno, S. Juodkazis, M. Mino, V. Mizeikis, and H. Misawa. *J. Phys. Chem. C*, 111:4180–4184, 2007.

[124] K. Ueno, S. Juodkazis, V. Mizeikis, K. Sasaki, and H. Misawa. *Adv. Mater.*, 20:26–+, 2008.

[125] C. Oubre and P. Nordlander. *J. Phys. Chem. B*, 108:17740–17747, 2004.

[126] C. Oubre and P. Nordlander. *J. Phys. Chem. B*, 109:10042–10051, 2005.

[127] D. W. Brandl, N. A. Mirin, and P. Nordlander. *J. Phys. Chem. B*, 110:12302–12310, 2006.

[128] T. Jensen, L. Kelly, A. Lazarides, and G. C. Schatz. *J. Clust. Sci.*, 10:295–317, 1999.

[129] A. J. Haes, S. L. Zou, G. C. Schatz, and R. P. Van Duyne. *J. Phys. Chem. B*, 108:6961–6968, 2004.

[130] L. Yin, V. K. Vlasko-Vlasov, A. Rydh, J. Pearson, U. Welp, S. H. Chang, S. K. Gray, G. C. Schatz, D. B. Brown, and C. W. Kimball. *Appl. Phys. Lett.*, 85:467–469, 2004.

[131] S. H. Chang, S. K. Gray, and G. C. Schatz. *Opt. Express*, 13:3150–3165, 2005.

[132] L. J. Sherry, S. H. Chang, G. C. Schatz, R. P. Van Duyne, B. J. Wiley, and Y. N. Xia. *Nano Lett.*, 5:2034–2038, 2005.

[133] L. Novotny and B. Hecht. *Principles of Nano-Optics*. Cambridge University Press, 2006.

[134] E. Lorin, S. Chelkowski, and A. Bandrauk. *Comput. Phys. Comm.*, 177:908–932, 2007.

[135] I. L. Garzon, C. Rovira, K. Michaelian, M. R. Beltran, P. Ordejon, J. Junquera, D. Sanchez-Portal, E. Artacho, and J. M. Soler. *Phys. Rev. Lett.*, 85:5250–5251, 2000.

[136] C. E. Roman-Velazquez, C. Noguez, and I. L. Garzon. *J. Phys. Chem. B*, 107:12035–12038, 2003.

[137] H. Hakkinen, R. N. Barnett, and U. Landman. *Phys. Rev. Lett.*, 82:3264–3267, 1999.

[138] R. N. Barnett, C. L. Cleveland, H. Hakkinen, W. D. Luedtke, C. Yannouleas, and U. Landman. *Eur. Phys. J. D*, 9:95–104, 1999.

[139] H. Hakkinen, M. Walter, and H. Gronbeck. *J. Phys. Chem. B*, 110:9927–9931, 2006.

[140] K. Nobusada. *J. Phys. Chem. B*, 108:11904–11908, 2004.

[141] B. K. Teo, H. Zhang, and X. B. Shi. *J. Am. Chem. Soc.*, 115:8489–8490, 1993.

[142] R. Ahlrichs, M. Bar, M. Haser, H. Horn, and C. Kolmel. *Chemical Physics Letters*, 162:165–169, 1989.

[143] C. T. Lee, W. T. Yang, and R. G. Parr. *Phys. Rev. B*, 37:785–789, 1988.

[144] A. D. Becke. *J. Chem. Phys.*, 98:5648–5652, 1993.

[145] D. Andrae, U. Haussermann, M. Dolg, H. Stoll, and H. Preuss. *Theor. Chim. Acta*, 77:123–141, 1990.

[146] M. E. Casida and D. R. Salahub. *J. Chem. Phys.*, 113:8918–8935, 2000.

[147] R. Bauernschmitt and R. Ahlrichs. *Chem. Phys. Lett.*, 256:454–464, 1996.

[148] R. Bauernschmitt, M. Haser, O. Treutler, and R. Ahlrichs. *Chem. Phys. Lett.*, 264:573–578, 1997.

[149] F. Furche. *J. Chem. Phys.*, 114:5982–5992, 2001.

[150] A. Guinier. *X-Ray Diffraction: In Crystals, Imperfect Crystals, and Amorphous Bodies*. Dover Publications, 1994.

[151] Y. Negishi and T. Tsukuda. Private communication.

[152] C. L. Cleveland, U. Landman, M. N. Shafigullin, P. W. Stephens, and R. L. Whetten. *Z. Phys. D-Atoms Mol. Clusters*, 40:503–508, 1997.

[153] J. A. Larsson, M. Nolan, and J. C. Greer. *J. Phys. Chem. B*, 106:5931–5937, 2002.

[154] R. Stowasser and R. Hoffmann. *J. Am. Chem. Soc.*, 121:3414–3420, 1999.

[155] I. L. Garzon, J. A. Reyes-Nava, J. I. Rodriguez-Hernandez, I. Sigal, M. R. Beltran, and K. Michaelian. *Phys. Rev. B*, 66:073403, 2002.

[156] T. Iwasa and K. Nobusada. *J. Phys. Chem. C*, 111:45–49, 2007.

[157] J. P. Perdew, K. Burke, and M. Ernzerhof. *Phys. Rev. Lett.*, 77:3865–3868, 1996.

[158] H. Gronbeck, A. Curioni, and W. Andreoni. *J. Am. Chem. Soc.*, 122:3839–3842, 2000.

[159] Z. Y. Lin, R. P. F. Kanters, and D. M. P. Mingos. *Inorg. Chem.*, 30:91–95, 1991.

[160] H. Zhang and B. K. Teo. *Inorg. Chim. Acta*, 265:213–224, 1997.

[161] C. Cohen-Tannoudji, J. Dupont-Roc, and G Grynberg. *Photons and Atoms - Introduction to Quantum Electrodynamics*. Wiley-Interscience, 1989.

[162] D. P. Craig and T. Thirunamachandran. *Molecular Quantum Electrodynamics*. Dover Publications, 1998.

[163] S. Mukamel. *Principles of Nonlinear Optical Spectroscopy.* Oxford Series on Optical and Imaging Sciences. Oxford University Press, 1999.

[164] J. D. Jackson. *Classical Electrodynamics Third Edition.* Wiley, 1998.

[165] K. Yabana and G. F. Bertsch. *Phys. Rev. B*, 54:4484–4487, 1996.

[166] E. Runge and E. K. U. Gross. *Phys. Rev. Lett.*, 52:997–1000, 1984.

[167] F. Calvayrac, P. G. Reinhard, E. Suraud, and C. A. Ullrich. *Phys. Rep.*, 337:493–578, 2000.

[168] M. A. L. Marques, A. Castro, G. F. Bertsch, and A. Rubio. *Computer Physics Communications*, 151:60–78, 2003.

[169] N. Troullier and J. L. Martins. *Phys. Rev. B*, 43:1993–2006, 1991.

[170] L. Kleinman and D. M. Bylander. *Phys. Rev. Lett.*, 48:1425–1428, 1982.

[171] J. P. Perdew and A. Zunger. *Phys. Rev. B*, 23:5048–5079, 1981.

[172] I. Vasiliev, S. Ogut, and J. R. Chelikowsky. *Phys. Rev. B*, 65:115416, 2002.

[173] A. Wasserman, N. T. Maitra, and K. Burke. *Phys. Rev. Lett.*, 91:263001, 2003.

[174] G. F. Gabriele and G. Vignale. *Quantum Theory of the Electron Liquid.* Cambridge Univ. Press, Cambridge, 2005.

[175] F. Cataldo. *Polyhedron*, 23:1889–1896, 2004.

[176] TURBOMOLE Version 5.10 (2008), *Quantum Chemistry Group*, *University of Karlsruhe* : *Karlsruhe*, *Germany*..

[177] John P. Perdew and Yue Wang. *Phys. Rev. B*, 45:13244, 1992.

[178] A. Schafer, H. Horn, and R. Ahlrichs. *J. Chem. Phys.*, 97:2571–2577, 1992.

[179] These bond lengths remain almost unchanged (i.e., at most 0.0024 Å for C_3-C_4) even if the geometry optimization was performed by using the B3LYP functional [143, 144].

[180] K. Yabana and G. F. Bertsch. *Int. J. Quantum Chem.*, 75:55–66, 1999.

[181] J. R. Chelikowsky, N. Troullier, K. Wu, and Y. Saad. *Phys. Rev. B*, 50:11355–11364, 1994.

[182] K. Burnett, V. C. Reed, J. Cooper, and P. L. Knight. *Phys. Rev. A*, 45:3347–3349, 1992.

[183] T. Brabec and F. Krausz. *Rev. Mod. Phys.*, 72:545–591, 2000.

[184] J. J. Sakurai. *Modern Quantum Mechanics (Revised Edition).* Addison Wesley; Rev Sub edition, 1993.

[185] R. W. Boyd. *Nonlinear Optics, Third Edition.* Academic Press; 3 edition, 2008.